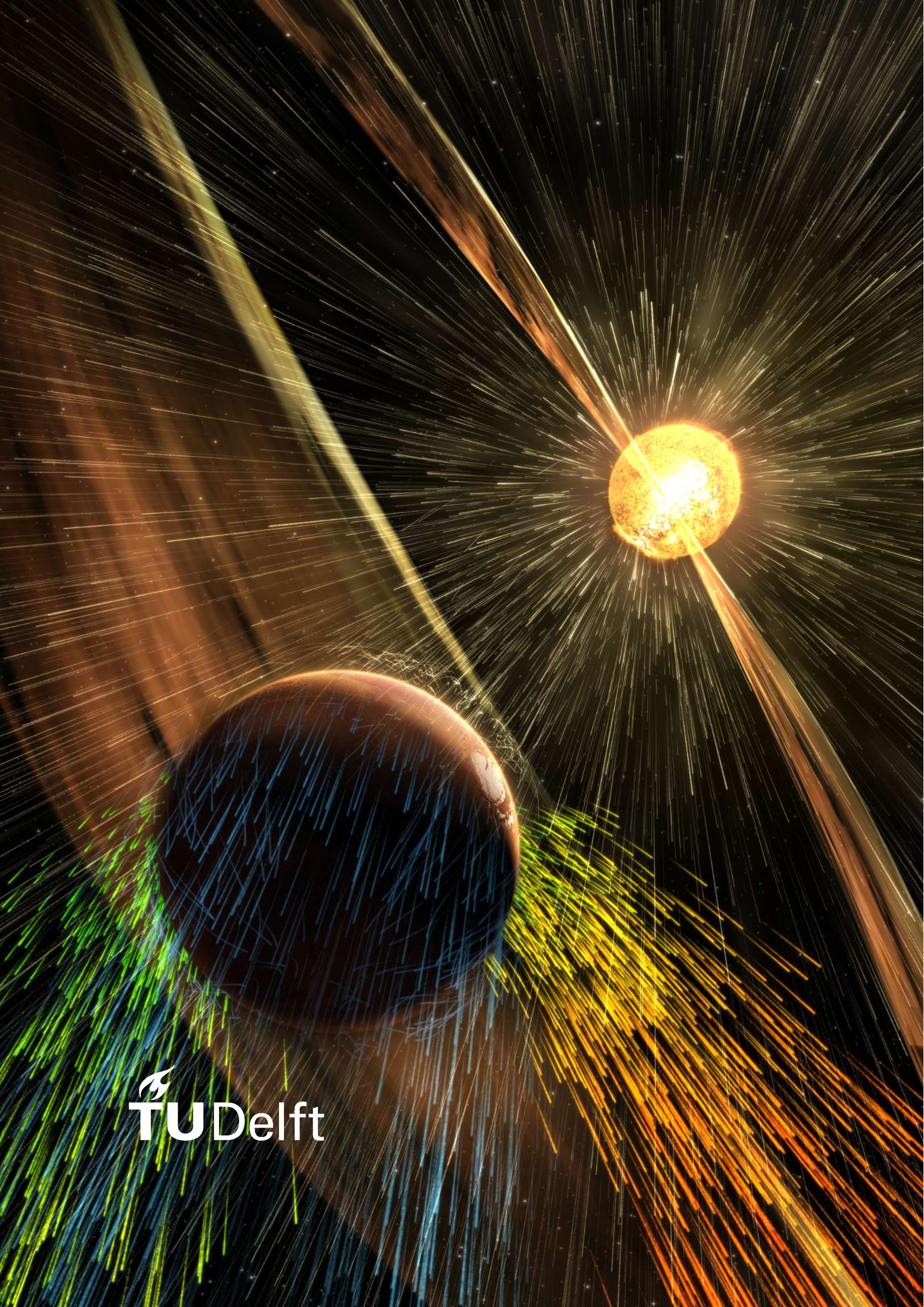
TUDelft

Spacecraft Radiation Shielding

Study of a 6U-CubeSat in Interplanetary Orbit

By

Timo Sanders
(4036352)

Master Thesis

Department of Space Engineering
Faculty of Aerospace Engineering
Delft University of Technology

6 December 2018

Daily Supervisor:	Dr. A. Menicucci	TU Delft
Chair of Graduation Committee:	Dr. A. Cervone	TU Delft
External Committee Member:	Dr. D. Stam	TU Delft

Acknowledgements

A large contribution to this thesis study has been made by dr. Alessandra Menicucci, who was willing to guide me during this leap into the world of space radiation and high energy physics. Her enormous enthusiasm about the research topic was and still is a great motivation on a new field of studies for me as a master student in space engineering. Besides that, she was incredibly supportive by introducing me to FASTRAD and providing me with the unique opportunity to use the tool. Without which the thesis would not have been what it has become. Therefore, I want to thank the TRAD company for giving me this opportunity to use their software.

Abstract

This thesis studies the radiation dose deposited on a 6U CubeSat in interplanetary orbit. The European Space Agency's radiation data tool SPENVIS has been used to determine the proton flux in interplanetary space during a solar particle event which occurs only once every one hundred years. SPENVIS has further been applied to obtain a dose depth curve for this specific 1-in-100 years proton flux. Simultaneously, 6U simplified models of several materials are created as well as a realistic 6U CubeSat structure which represents the state-of-the-art in CubeSat industry. Using radiation simulation tool Fastrad, two simulations have been performed: ray-tracing simulation and forward Monte Carlo simulation. Ray-tracing simulation provides a sector shielding analysis of the models, giving an overview of the received radiation dose for each specific point in the models. Forward Monte Carlo gives an overview of the deposited radiation for each part of the model, which has shown especially beneficial for the state-of-the-art model, in which deposited dose has been obtained for each part in the model. This has led to a dataset that shows the radiation dose deposited at each location and in each part of the 6U CubeSat structure during a 1-in-100 years solar particle event that strikes in interplanetary space.

Summary

The environment to which a satellite t in interplanetary orbit is subjected, is hazardous and possibly mission threatening. The total accumulated radiation doses caused by high energy ionizing particles are higher compared to those encountered in Low Earth Orbit missions. The absence of a protective magnetosphere is the prime reason for in terms of the radiation environment (solar particles and galactic cosmic rays) interacting with the satellite. The radiation analysis is a critical element for any deep space mission. In the last years, hundreds of nanosatellites like CubeSat have been launched into LEO. The technology has proved to be mature enough to be possibly apply to deep space missions such as the exploration of the Moon or Mars.

CubeSats can provide low-cost and fast track opportunities for scientific missions. The radiation hardening assurance of a CubeSat should start with the analysis of the shielding provided by the structure. This thesis presents an example of how this analysis can be carried out using the radiation simulation tool Fastrad. To examine the radiation shielding of current and potential future CubeSat bus structure designs, ten models have been simulated.   After examination of the trend in interplanetary CubeSat mission designs and the minimum sizes for payloads and subsystems for these missions, a 6U CubeSat model has been created which is representative of the state-of-the-art. Since the CubeSat standard constraints the size and volume of the CubeSat, this work was focused on investigating different configuration for the materials used in the structure. For all the configurations considered, simplified models were created and analysed. Four of these models in this study are pure aluminium models, ranging in thickness from 1mm to 5mm. Three models include a layer of polyethylene, which is included for low-Z ionized material shielding, such as protons. The last three models also include a thin copper layer, to check the shielding capacity against heavier ions by this heavy metal copper. Next to these simplified structures, a real life state-of-the-art 6U CubeSat model has been obtained too. After generation of representative radiation environments in SPENVIS, the CubeSat models placed into a worst-case scenario concerning the radiation environment, corresponding to a 1-in-100 years solar particle event peak flux.

By using the radiation simulation tool Fastrad, both a sector shielding analysis and a Forward Monte Carlo (FMC) simulation have been performed. The sector shielding analysis has given results for received radiation doses at specific locations. The built-in ray-tracing tool writes a sector-file that contains the thickness information on material passed through by the rays. This sector-file can then be used to virtually map this thickness information onto the outside of the model, giving a visualization of the thicker and thinner layers passed towards each specific detector.

The FMC-simulation has proven to be very useful to test the state-of-the-art 6U CubeSat model and its 298 parts individually. This resulted in a deposited radiation dose for each of these 298 parts of the satellite, hence showing which parts of the satellite require improved shielding against incoming radiation. The results following from these analyses and simulations provide an overview of weak-spots for each location in the satellite, in which a vulnerable payload or electronic device would be placed. These results can contribute to the design of a radiation-tolerant future CubeSat mission in deep-space orbit.

Table of Content

1. Introduction

High-energy ionizing particles are travelling through space at all times. Space radiation hits anything that comes in its path. For satellites, space radiation is a prime danger when orbiting Earth or other celestial bodies. As spacecraft are unreachable for human hands, the design should be failure-safe and as a result, the radiation coming at a spacecraft should not harm the mission before it has successfully exploited the targets set.

The radiation hazard that space radiation and high-energy particles pose to small spacecraft like CubeSats is potentially mission threatening. In 2018, the first interplanetary CubeSats (MARCOs on-board of the Insight mission) have been launched by NASA, escaping the Earth's protective magnetosphere. This new mission destination for CubeSats poses increased space radiation threats to the material and payload of the CubeSats on these interplanetary missions. Therefore, it is important to study the radiation shielding capabilities of state-of-the-art CubeSat bus structures and find potentially improved designs. This thesis focuses on precisely that.

First step taken in this thesis is outlining the theory on space radiation (Ch. 2). A state-of-the-art review of technology of CubeSats follows (Ch. 3). Once this is done, the radiation environment in an interplanetary orbit is simulated with SPENVIS, ESA's Space Environment Information System (Ch.5). Four scenarios have been selected, ranging from short term peak fluxes that occur only once every 100 years to long term particle fluences during a full solar cycle. The space radiation data that come out of SPENVIS are then used as input for FASTARD (Ch. 6), a radiation simulation tool which combines geometry models (e.g. CAD) of spacecraft with the radiation environment models data. By combining these two elements in FASTRAD, the radiation doses on every location in the satellite can be detected and the model can be inspected with these results (Ch. 7).

In order to narrow down the thesis to a 30-week assignment, several statements have been made during the literature review and led to the main research question of this thesis. The requirements that are obtained from these statements are listed below:

1. The spacecraft shall be a CubeSat.
2. The volume of the CubeSat shall of size 6U (6 Units).
3. The trajectory type of the CubeSat shall be of the type 'interplanetary'.
4. The target orbit of the CubeSat shall be lunar.
5. The mass of the shielding material shall not increase with respect to conventional structural materials.
6. The predominant field of study for shielding shall be the radiation range up to 1 GeV
7. Design of the shielding material shall not hinder the other subsystems of the CubeSat mission

This leads to <u>the main research question</u>:

<u>"What are radiation doses experienced by a 6U CubeSat in a test-case interplanetary orbit?"</u>

And to the *subquestions:*

1. *"Which material choices allow a reduction in radiation dose?"*
2. *"What are the local radiation doses at each part of a state-of-the-art 6U CubeSat?"*
3. *"What improvements of the state-of-the-art design can enhance the radiation shielding capability?"*

2. Space Radiation

Deep space: infinite, beautiful and hazardous. Once a spacecraft escapes the cocoon we call the magnetosphere, uncertainty awaits. What you leave behind is a protected environment with free air and a brisk sunshine if you are lucky. But if you are on an interplanetary trajectory towards the Moon or Mars, radiation levels culminate and shielding is required. It is exactly this trajectory that will be followed in this literature review and following thesis project.

CubeSats have been around for almost two decades. In these years, the concept has conquered the world. Short development time, low cost and commercial-of-the-shelf availability have made it to the most popular method of space systems engineering at universities all over the world. Now, a new challenge awaits. Instead of orbiting Earth, the first CubeSat missions are planned towards the Moon and Mars. With these plans, come new challenges. One of these challenges is the radiation level that these nanosatellites will be subjected to.

Space radiation, otherwise known as ionizing radiation, poses a threat to spacecraft and astronauts. The adjective 'ionizing' implies that the particles hitting the spacecraft have enough energy to free one or more electrons from their atomic bonds, which becomes ionized. . These high energy particles fluxes are composed of protons, electrons, neutrons, alpha particles and higher atomic number ions. During the ionization process secondary particles can be created via electromagnetic and nuclear interactions (i.e. Bremsstrahlung emission). This is called secondary radiation and is a very important factor to consider when designing for radiation robust systems. The secondary particles can in turn ionize the material further by colliding. B (Norbury J.W., 2010).

This chapter presents the radiation environment for CubeSats in interplanetary orbit. This chapter shall be used for the required background knowledge to successfully exercise the later stages of this thesis. The different components of space radiation will be introduced (2.1), the radiation charging of a spacecraft and secondary radiation (2.2) and finally a look will be taken into the Moon case (2.3): what is the radiation environment for a spacecraft in lunar orbit?

2.1. Components of Space Radiation

One of the first notions of space radiation was Aurora Borealis – the Northern Light. It was only at the start of the space age in 1958 that magnetospheric physics was 'founded'. The launch of a Geiger teller on board of the Explorer-1 satellite by James Van Allen established the presence and location of the well-known Van Allen belts (Loff S., 2017). Since then, the dangers of space radiation have been studied and are still subject of research for many scientists around the world.

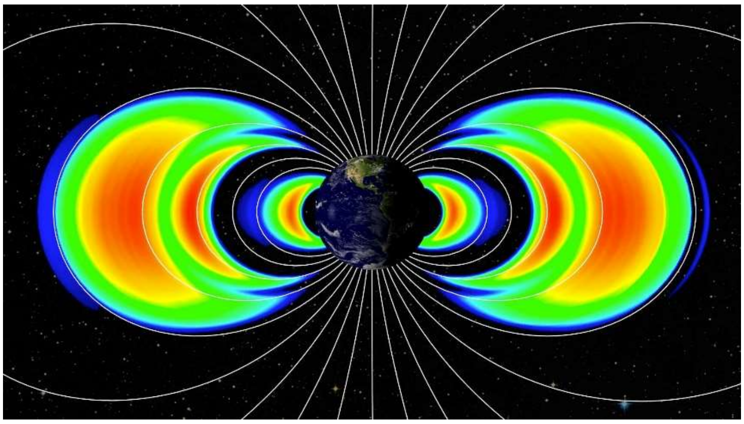

Figure 2.1: Depiction of the Van Allen radiation belts (Well H., 2017)

Space radiation consists of three kinds (NASA, 2002). First there is the trapped radiation in Earth's magnetic field. It serves as a protection shield against stellar radiation, primarily coming from the Sun. Like a bow-wave of a ship, the magnetic field is forming a shock wave between the Earth and the Sun. Despite this protection, a portion of the particles gets trapped in the magnetic field of the Earth. These particles form two rings around the Earth: the Van Allen belts. As shown in Figure 2.1, there are 2 belts: the inner and the outer. Both belts are almost toroidal in shape. The inner belt is mainly composed by high-energy protons and extends from 0.2 Earth radii to 2 Earth radii altitude. The outer belt is mainly composed by electrons and extends from 3 to 10 Earth radii. The protons in this inner belt cause the most radiation problems for spacecraft in Low Earth Orbit (LEO) and during the initial stages of spacecraft on an interplanetary flight. The protons are found to have energies up to several hundreds of MeV. The fact that the Earth magnetic field is slightly offset and tilted with respect to the Earth's spin axis causes the inner Van Allen belt to dip to altitudes of 200 [km] above the Earth's surface. This anomaly is called the 'South Atlantic Anomaly' (SAA) and it situated off the coast of Brazil. Spacecraft in Low Earth Orbit are affected by which is also relevant for the astronauts in and around the International Space Station (ISS).

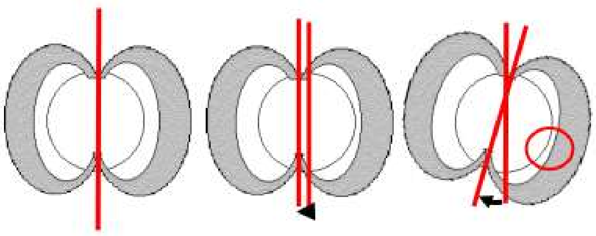

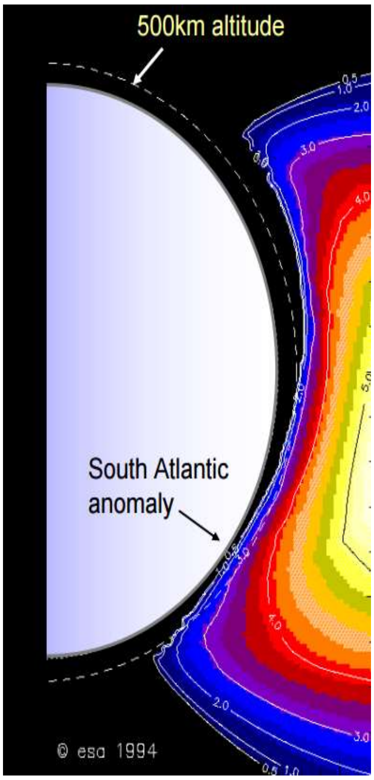

Figures 2.2 and 2.3: Indications of the South Atlantic Anomaly.

For interplanetary spaceflight, the radiation portion by the trapped particles is low compared to what awaits outside Earth's magnetic field. As discussed before, the Earth is shielded from solar and galactic radiation that is travelling towards it.

The source of SPE is the Sun, where solar flares, and coronal mass ejections, emit large bursts of protons, electrons and ions which travel into space at velocities of close to the speed of light. Because of the abundance of protons amongst the particles in solar events, these are of the main importance when considering radiation from the Sun. In an SPE, the proton flux is defined as >30 MeV and >10^6 protons/cm^2, where about one or two major SPE (>10^{10}protons/cm^2) can be expected over the course of a solar cycle.

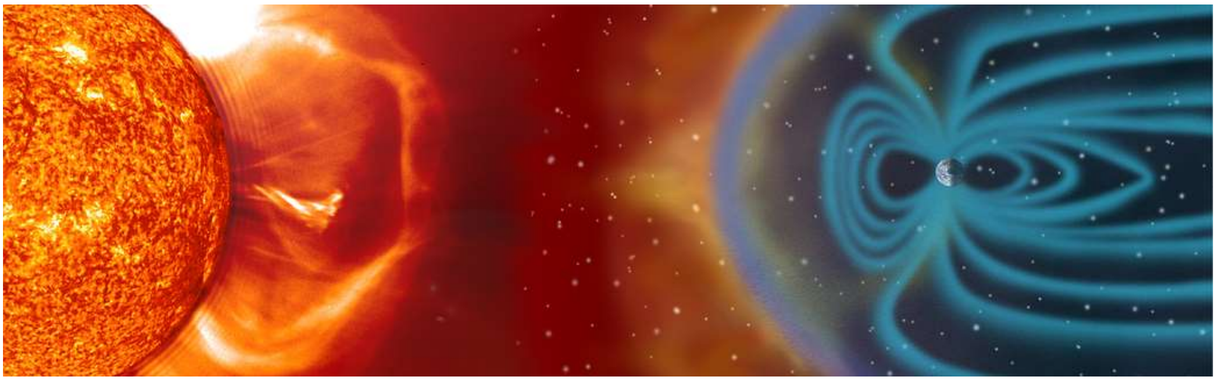

Figure 2.4: Solar wind flowing towards Earth's Magnetic Field (NASA, 2017)

SPE can be divided into two categories; solar flares and coronal mass ejections. Solar flares are short (order of hours) and impulsively shot into the solar system in a constraint zone of 30-45 degrees solar longitude and with a fluence of 10^7-10^8. Instead, coronal mass ejections happen over the course of days and have a higher fluence that can exceed 10^9/cm^2 at a spreading of 60-180 degrees. In order to illustrate the phenomena of solar flares and mass ejections further, they are illustrated hereunder. Some of the most active SPE are plotted to indicate the severity of these solar storms and the particles that are shot in Earth's direction. Herein one can see that high energy (10 MeV – 1 GeV) protons travel in high fluences (up to 10^{10}protons/cm^2) towards spacecraft on interplanetary missions.

In addition to solar particles, electromagnetic emissions include radiation in the form of X-rays and gamma-rays. The following release and acceleration of particles during an SPE can reach fluxes exceeding 100 particles/cm^2 with energies greater than 10 MeV with some identified energies as high as 25 GeV. In the last three decades of the twentieth century, more than 200 solar particle events with energies over 10 MeV and peak fluxes of ten protons/cm^2 are recorded (Kurt et al. 2004). It should be pointed out that solar flare activity and intensity has been fairly constant in the last ten million years (Shirley J.H., 1997). Since the 1950s, humans have become interested in these solar phenomena as well, with the rise of spaceflight.

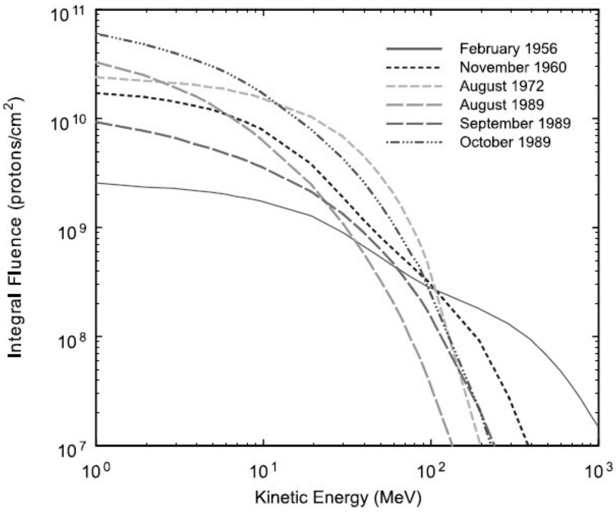

Figure 2.5: Integral Fluence as a function of kinetic energy for some large energetic solar events (George J.S. et al., 2009).

The third type of space radiation concerns galactic cosmic rays or GCR. As mentioned before, space radiation always has a stellar origin, in this case from outside the solar system. Although the source of GCR has been debated over time, GCR are believed to originate from exploding stars – supernovas – that launch part of their material into space in the form of protons, electrons, and ions (Mark H. 2003). The presence of GCR is thought to be uniform in space. The energy that GCR have, range from several MeVs up to 10^{12} MeV, shielding is therefore difficult and it will primarily be taken into account as a cause of single-event phenomena that spark secondary radiation.

Only two percent of the particles in the rays are electrons, the other 98 percent represent protons and heavy ions with the following composition: 87% protons, 12% helium ions, also called alpha particles, and 1% of heavier ions up to uranium (George J.S. et al., 2009). Although the heavier ions only represent one percent of the particles, these are highly penetrating and pose a threat to spacecraft material. Especially iron ions, as these are relatively abundant and heavy, as can be seen in Figure 2.6 that visualizes the presence of the several heavy ions up to nickel. Ions with higher valence than nickel have a clearly lower abundance. These heavy ions are especially lethal for human missions as these particles disturb the bodies of astronauts. The damage inflicted by these ions can be of so severe, that heavy disruption of cells can occur. When looking at material design for satellites, the radiation level is a smaller problem, but still a radiation load that imposes risks to the mission.

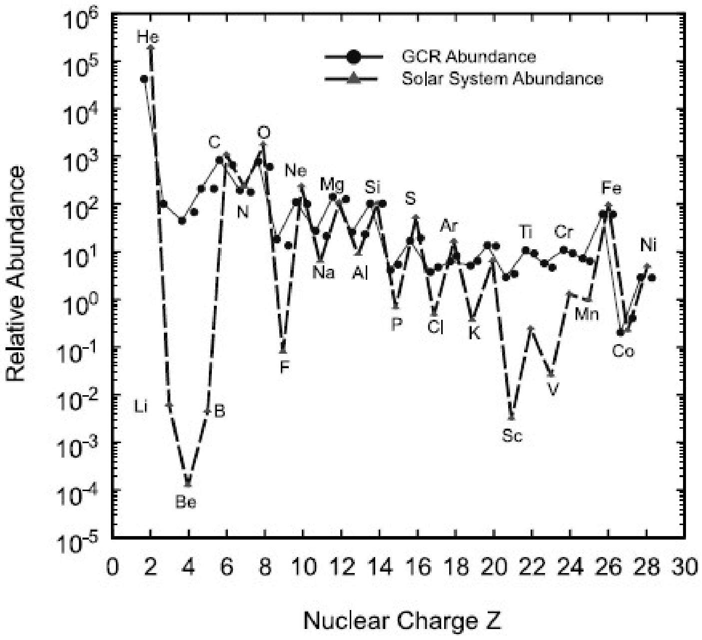

Figure 2.6: Relative abundance of chemical elements in the solar system and in galactic cosmic rays (George J.S. et al., 2009)

With energies that range from several MeV up to thousands of GeV, the galactic cosmic rays can have devastating effects. Despite their high velocity and energy, the solar radiation activity discussed earlier, can have a diminishing effect on the GCR with lower than 1 GeV energy. This is shown by Wilson (Wilson et al. 2008) in Figure 2.7 below. Whereas higher energy GCR are not affected by the Sun, the rays up to one GeV are decimated in fluence, especially during solar maximum. This has to be kept in mind when planning an interplanetary mission as it can be used as a natural radiation mitigation method. This fluence alternation during a solar cycle will be further discussed in the 'Moon Case', a section where the radiation levels and environment at the Moon are introduced in more detail.

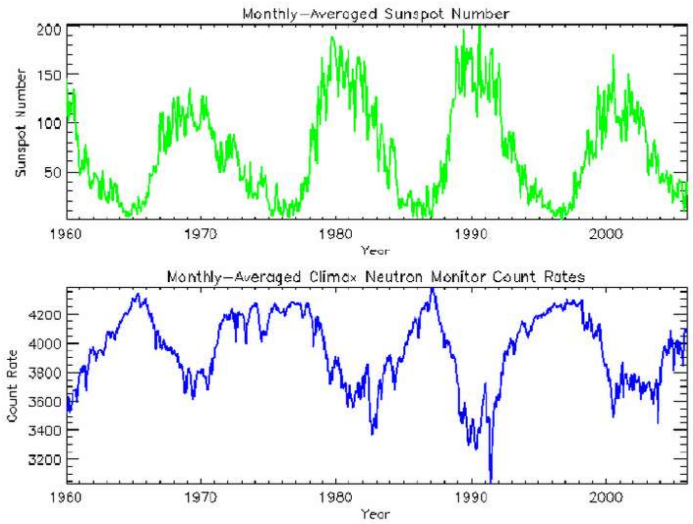

Figure 2.7: Neutron abundance on Earth surface (bottom) and galactic cosmic rays (top) fluxes in several solar cycles. The anti-correlation between solar activity and cosmic rays abundance is clearly visible. (Wilson et al. 2008)

2.2 Spacecraft Charging and Secondary Radiation

During their time in orbit, spacecraft are subjected to incoming radiation as covered in section 2.1. In this section the effects for spacecraft will be described. Making the distinction between a single incoming high energetic particle and the effect of the total dose that builds up during the mission.

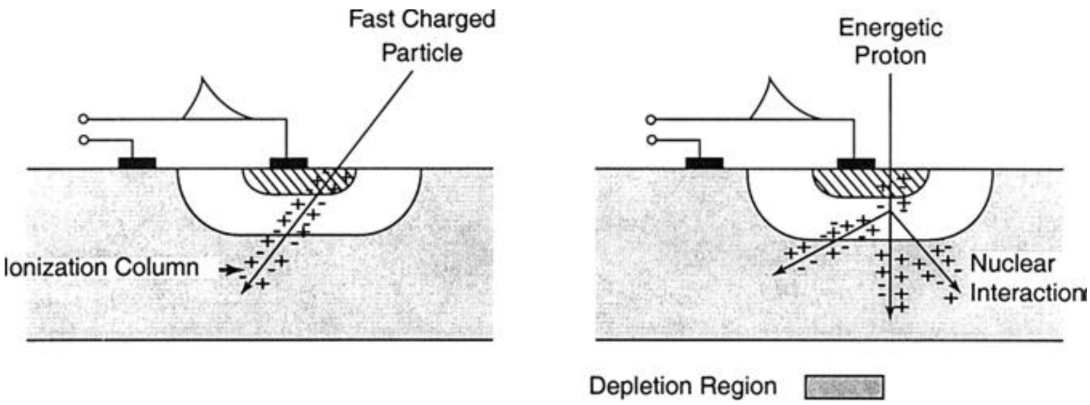

Figure 2.8: Single particle event (left) and Secondary radiation illustrations (Wertz, J.R. 1999)

In Figure 2.8, one can see a single high energy charged particle hitting the sensitive node of an electronic component on the left and an incoming proton which causes a nuclear interaction with subsequent secondary particles creation. Space Mission Analysis and Design by J.R. Wertz (1999) describes three types of single particle events on electronics. Least severe is the bit-flip or single event upset (SEU). Such an SEU has no interference with the operation of the hardware and no prolonged consequences. Second type described by Wertz is the single event latch-up (SEL). This type of single event causes the specific device to malfunction and eventually switch off. It can only operate after a switch off and on. The last and most severe single event is called single-event burnout, which is as bad as it sounds: the device is no longer operational.

Besides these single particle events, the radiation dose builds up due to electrons and protons aimed at the spacecraft (Copeland S., 2012). After a longer period of particle exposure, the electrons and protons inside may build up a high electric field. If the field is high enough, it may be sufficient to cause a local dielectric breakdown. When a local breakdown occurs, ionization channels develop extremely rapidly inside the dielectric, allowing currents to flow, which in turn generate more ionization and heat. As a result, internal instruments may be damaged. Luckily, the occurrence of high energetic (10MeV<) is relatively low in the Earth region (up to GEO). At the same time, this is the main area of spacecraft charging (Lai S.T., 2011). The charging effects of interplanetary satellites shall thus not only depend on the swift passage through the Van Allen belts, but predominantly on the single particle events discussed earlier in this chapter.

2.3 The Lunar radiation environment

In this section the radiation environment which is encountered during a Lunar mission is analysed. Lunar mission have been fascinating for humans since the Apollo era. In the last years the interest for CubeSat mission in Moon orbit has also raised. However, as pointed out before, the radiation environment in Lunar orbit is harsh. Whilst other close celestial bodies such as Mars have a very slight atmosphere, the Moon does not possess such shielding characteristics and can be treated as a worst case scenario.

One of the main fluctuations in the radiation environment is caused by the Sun's activity. During solar minimum, the interplanetary magnetic field is weakest and vice versa in solar maximum. At lower solar activity, more galactic cosmic rays can therefore penetrate the solar system. This causes changes in the amount and energy level of GCR reaching the Moon. During solar minimum, the GCR levels at the Moon are 2.5 times denser than during a solar maximum (Eckart P., 2006). As one can see in the Figure 2.9 below. The fluences of all ionized material decreases during a solar maximum. This factor can be taken into account when planning missions that last shorter than a full solar period, as the solar minimum can be avoided.

However, there are those GCR particles that are unaffected by the solar maximum counteracting radiation. The higher energy particles of over 1 GeV are in general still able to reach the lunar environment, as their energy is too high compared to the solar activity radiation. As the fluences of high energy particles are lower, the collision risk is lower. However, the result of such a collision with spacecraft material is more disruptive because the chances of ionization of material increases with increasing energy.

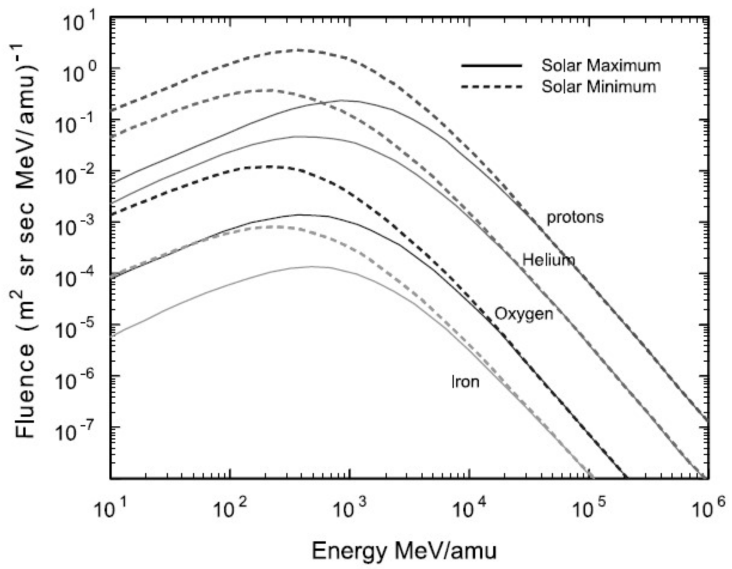

Figure 2.9: Difference of GCR particle flux at solar minimum and maximum (Eckart P., 2006)

3. CubeSat: State-of-the-Art and Shielding Capabilities

The CubeSat idea came to life in the United States, in a combined effort of Stanford University and California Tech. Some years after its announcement, one of their successful launches was the QuakeSat in 2003 (Kramer H.J., 2017). A 3U CubeSat designed to measure extra low frequency magnetic signal data to recognize signals that would come from earthquakes. A revolutionary thought, that was extra special due to the small size of the spacecraft. This small and standardized spacecraft structure started to take over the industry, especially at universities the new phenomenon was a breakthrough. Students and staff had a budget-friendly way to system design a spacecraft, that in some cases was part of a common project called QB50 (QB50.eu, 2017). QB50 is a shared effort of universities to have measurements taken by CubeSat that are orbiting Earth in a low Earth orbit. By sharing cost and knowledge, the scientific world benefits from this collaboration.

CubeSat missions are widely applied for LEO orbits. However, the future of this type of spacecraft might see it travel further than that. As explained in the previous chapter on radiation, the interplanetary environment is hostile due to the higher fluxes of galactic cosmic rays and solar flares. In order to investigate the shielding capabilities of CubeSats, this chapter will start by stating the state-of-the art materials and design for bus structures of CubeSats. Then, the protection provided by these designs are discussed, followed by a section on properties of materials that are beneficial when trying to shield a spacecraft. At the end of this chapter consists of two parts. One deals with strategies which improve the radiation shielding of CubeSats and the second one will be about risk mitigation possibilities.

3.1 State-of-the-art CubeSat structures

CubeSats come in several size, of which a range of 1U to 8U is depicted in Figure 3.1. In the last decade, the number of CubeSats has increased and is still increasing. This can be seen in Figure 3.2, where one sees a sharp increase from 2013 (88 launched CubeSats) onwards to 2023, where currently 703 CubeSats are predicted to be launched (Nanosats.eu, 2018). Another factor in the development of the CubeSat technology, is the widening of the range of sizes of nanosatellites. PocketCubes as well as 6U and even 8U/12U/16U/20U CubeSats are launched more frequently. The relative increase of larger CubeSats can also be seen from Figure 3.2, where the blue colours indicate the launch or planned launch of these PocketCubes and 6-20U CubeSats. In Figure 3.3, this trend can be spotted even more clearly. The companies that provide these larger CubeSat structures have increased their attention on these somewhat larger sized CubeSats, making it commercial-of-the-shelf (COTS) available for the industry.

Figure 3.1: The six basic CubeSat sizes: 1U, 2U, 1.5U, 3U, 6U and 8U (from left to right)

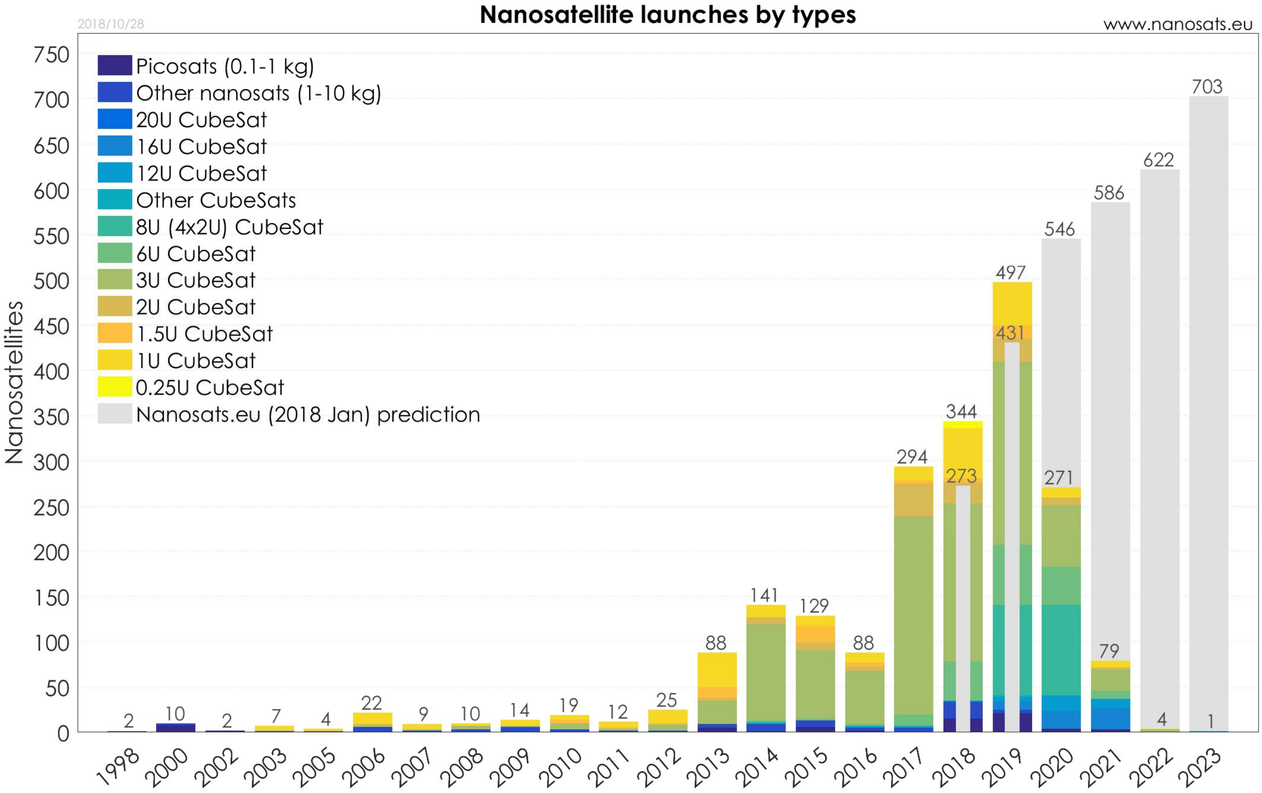

Figure 3.2: Timeline (1998-2023) nanosatellite launches. The sharp increase of amount of CubeSats from 2013 onwards and the relative shift towards larger (blue colours) CubeSats is clearly visible. (Nanosats.eu, 2018)

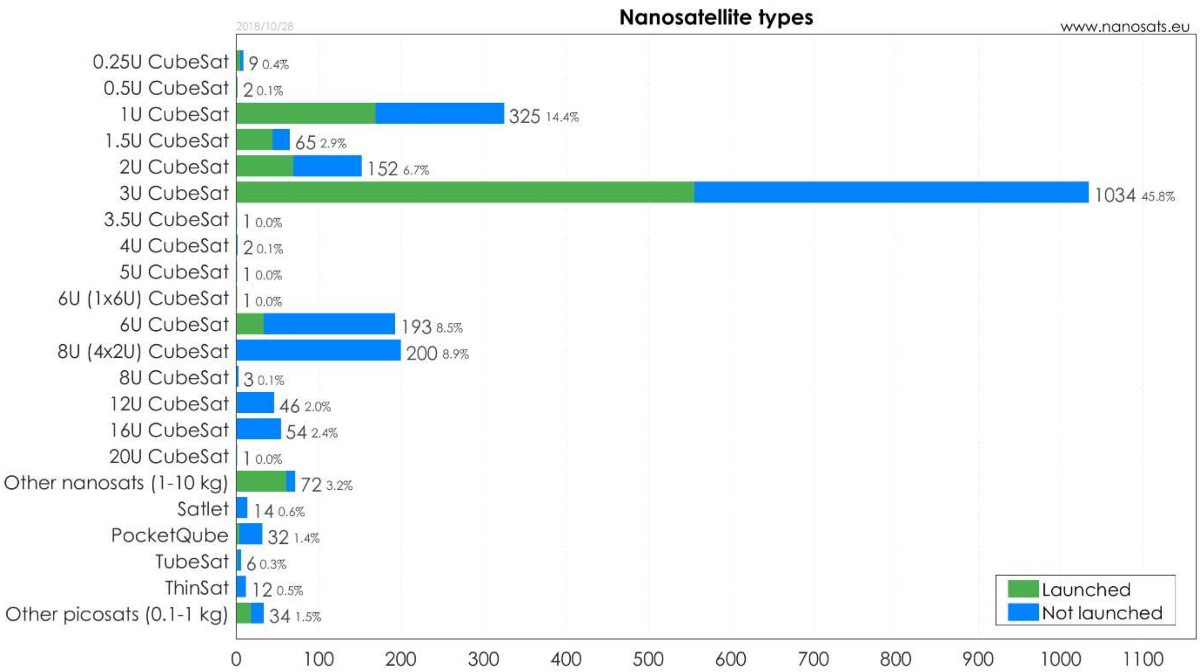

Figure 3.3: Nanosatellite types and the amount of launched (green) and not launched (blue) per type. The new application of 6U, 8U 16U and 20U CubeSats is clearly visible.

This section focuses on the several different sized CubeSats available and their properties, such as the material used. This is done to get an overview of the status quo of the CubeSat industry so that possible challenges can be identified when one would select CubeSats for mission purposes other than the current applications. The CubeSat structures in Figure 3.1 are readily available from the CubeSat shop (Cubesatshop.com, 2017) and are provided by Innovative Solutions in Space (ISIS). The outside is mostly covered by solar or body panels that provide the required power and complete the structure. These panels fit on the outside planes of the satellite and make it into a box-shaped object. The thickness of these panels is 1.8 [mm] for the top/bottom panels and 2.5 [mm] for the side panels (Cubesatshop.com, 2017 & ISIS, 2017). The manufacturer claims a two-year period of radiation proof spaceflight in Low Earth Orbit. The panels are available for 1U up to 8U panels, making 16U nanosatellites a possibility. The solar cell material is Gallium-Arsenide (GaAs) as is the case for many space applications.

Most widely used material for the frame of CubeSats and nanosats is aluminium. More specifically, the 7075, 6061 and 5052 types. The density of these materials lies in the range of 2.68-2.81 [g/cm^3]. The total mass for a 1U structure is around 50 [g], adding up to 300 [g] for a 6U mission. It might be clear that mass is a critical value in space mission design. As the contemporary CubeSat and nanosat missions are operating in LEO, this limited amount of (shielding) material fulfils the requirements.

Figure 3.4: Assembled 12U Nanosat (ISIS, 2017)

The company, ISIS, also provides fully assembled nanosats. One of the examples is the 12U Nanosat Figure 3.4. These slightly larger CubeSats are thought to start a new revolution in the use of CubeSats, providing the service of easy manufacturing and short development time for a wider range of spacecraft. To conclude this section, a short summary shall be provided below. This summary will concern successful first era 3U Cubesats, after that a few planned interplanetary CubeSat missions and examples of new missions using 6U-16U Cubesats.

At TU Delft, the first CubeSat project of The Netherlands was ignited in 2004, inspired by the American counterparts of Cal Tech and Stanford University. The first CubeSat called Delfi-C3 (TU Delft, 2017) was a demonstrator that has performed so well, that the project has evolved into numerous satellite projects. After the launch of DelfiC3 and its – still in orbit – successor DelfiN3XT, the focus now is twofold: to add a duo of CubeSats to the QB50 constellation and second to innovate by going even smaller than CubeSats. This new project called 'pocketcube' (TU Delft, 2017) is a proposal to go to an even smaller size of 0.5Ux0.5Ux0.5U, as technology allows for downscaling.

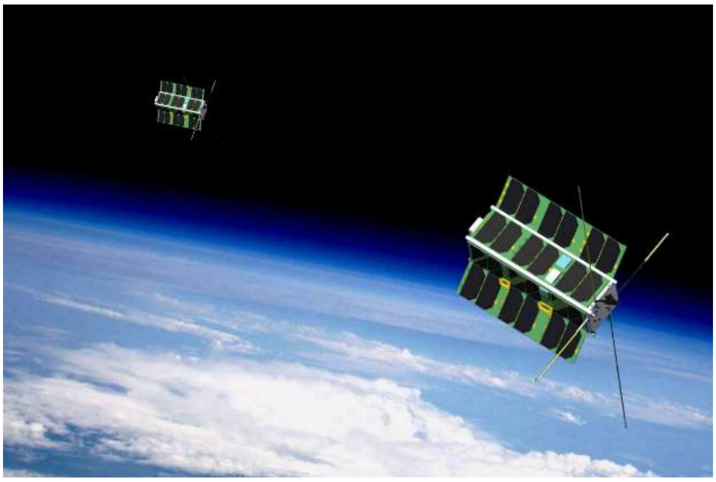

Figure 3.5: Artist impression of Delffi, the QB50 contribution of TU Delft. (TU Delft, 2017)

Until now the access to space for CubeSats has been limited to Low Earth Orbit. As mentioned already the new frontier is becoming interplanetary CubeSats, and for this reason the rest of this historical summary shall focus on the current and future efforts of space companies to explore near Earth celestial bodies such as the Moon and Mars.

The first announced deep space mission for a CubeSat is the Insight mission of NASA, a Martian lander that will study the surface and subsurface of the red planet. This mission includes two 6U CubeSats (NASA, 2017) to support the Insight ground station by relaying telemetry. The mission of the two CubeSats has been named MarCO (Mars Cube One) and shall be an uncritical addition to the Insight mission, meaning that failure is not catastrophic for the overall Insight mission. This path has been chosen by NASA to see the capability of CubeSats to operate in a deep-space environment. A successful operation life time could open the doors to more interplanetary operations by CubeSats and by that, create new chances for the entire space industry. Launch of the Insight mission and MarCO CubeSats has taken place on May 5 2018, with expected landing of the Insight mission on Martian soil on 26 November 2018. By that time, the CubeSats have been in interplanetary space for six months, so the test case for those CubeSats is taking place already.

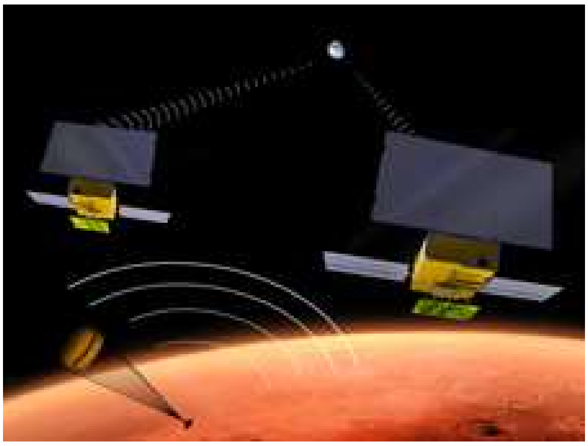

Figure 3.6: Artist illustration of MarCO: the first deep-space CubeSat mission (NASA, 2017)

The lessons that will be learned during this pioneer CubeSat mission will provide a database and perspective for the coming decade. Engineers at NASA have looked into the new requirements of an interplanetary mission. First, the lifetime will be longer and more critical since the CubeSat reaches Mars only after several months. Instead of a floating CubeSat without propulsion, the MarCO mission requires some orbit corrections and has to have the ability to keep its solar panels fixed towards the Sun as incoming solar flux is lower at Mars. Last but not least, there is the danger of a malfunction in the electronics due to radiation. This is perhaps the most critical and unstudied part of a longer and interplanetary CubeSat flight which also is the interest of this thesis. The rest of this chapter and this thesis will thus focus on what shielding methods exist for state-of-the-art CubeSats and whether there are improvements that can be made.

3.2 Radiation shielding methods for small spacecraft

Shielding a smaller spacecraft such as a CubeSat from space radiation, is a topic often overlooked due to the fact that the radiation environment in LEO is relatively mild. The relevance of this study comes forth from the interest of multiple companies to plan and operate CubeSat interplanetary missions. This section focuses on the way that current CubeSat structures shield their payload.

3.2.1 Inherent-Mass/Passive Shielding

One of the 'methods' is to optimally use the existing structure of the CubeSat or see whether the existing structure can mitigate the radiation environment that the spacecraft encounters. Some sections of the CubeSat will geometrically be more shielded than other sections. This method is called passive shielding. Passive shielding is most effective for lower energy radiation and at higher fluxes. When travelling beyond the magnetosphere, satellites are exposed to higher fluxes of cosmic rays which due to their very high energy, can penetrate the shielding thicknesses of a standard structure. The structure has weak spots in terms of capability to shield ionizing radiation and this is due to the fact that the structure and the materials are typically optimized only to withstand the structural loads of the spacecraft. Since the mass budget is a critical design factor in the space engineering, the option of increasing the thickness of the CubeSat structure is not applicable. Therefore, the improvement of CubeSats' radiation shielding capabilities shall be focused on using the most effective materials in an optimized configuration, and not increasing mass with respect to conventional materials. In the case that extra mass actually is added to the spacecraft for radiation shielding purposes, one speaks about inherent mass shielding.

3.2.2 Ad Hoc Shielding

Ad Hoc (Latin 'for here') shielding comes in place when considering specific spots or sections of the spacecraft. These smaller parts of the satellite then require further shielding than the shielding passively provided by the structural components. Once the radiation environment of a satellite is known, one can optimize the spacecraft structural components using Ad hoc shielding. This is more efficient than inherent mass shielding because of this direct implementation dependent of the radiation environment and component placement in that situation. The structural constraints which limit inherent mass shielding, are thereby loosened. One of the methods of ad hoc shielding involves multiple layers shielding, where several layers different in terms of thickness and material composition. The benefit of this approach, is that the mitigation of the secondaries created during the passage of the primary particle through the shielding can be optimized. This method is called "graded-Z shielding". The idea is to alternate layers with low and high Z (atom number) materials, in a configuration which minimizes the radiation emerging from the most inner layer. The low Z layers will shield against protons and ions and without having a large contribution to the secondary radiation. High Z layers are doped with metallic micro particles which scatter the electrons and photons efficiently. The combination of materials provides more shielding capacity than the sole use of structural materials such as aluminium. Using the software of SPENVIS – which will be discussed later – the shielding capability of several different layer structures can be analysed. This could result in an optimal way of providing radiation shielding to a small satellite.

3.3 Risk mitigation possibilities

The trend in proposed future CubeSat missions is to go bigger. The most common size for CubeSat lays between 6U up to 16U. Even though these rank high in mass with respect to the average developed CubeSat, the mass and size of these spacecraft is still limited. Consider that a 6U is equivalent to the size of a shoebox. In order to reduce the risk of mission failure or severe malfunction due to space radiation, different approaches will be discussed in this section.

Figure 3.7: A 3D-printed 1U CubeSat structure with PEEK material (ESA/ESTEC, 2017)

The research on new materials and manufacturing techniques is constantly evolving. One hot topic in this field at the moment is the application of Additive Manufacturing (also known as 3D printing) to space systems. For example ESA (ESA/ESTEC, 2017) is working on producing spacecraft materials with the use of a 3D-printer. Among other potential application (e.g. production of tools on-board of ISS) Additive Manufacturing has been applied to produce the 1U CubeSat shown in Fig. 2.13. The material used is polyether ether ketone (PEEK). PEEK is a strong thermoplastic with a high melting point. The CubeSat shown also conduct voltages, giving it an extra feature as the CubeSat would not require internal wiring.

Another major agency, across the Atlantic, has found a specific set of characteristics in a new material that could be of importance in the future. At NASA's Langley Research Centre, an existing technique was used to come up with Boron Nitride Nanotubes (BNNT).

The use of nanotubes was kicked off in 1991, but the material used was carbon. The new combination of Boron and Nitrogen gives an slightly ionized character to the material, causing the material to shield better against incoming radiation and be thermally stable up to high temperatures (1100 K) and have a very high Young's Modulus (up to 1.3 TPa) at the same time (Tiano et Al., n.d.). This material is therefore a viable solution to future spacecraft and human settlement at e.g. Mars. As can be seen in Figure 3.8, the doping of BNNT with hydrogen atoms, is a way of diving below the state-of-the-art protection levels. Keeping an eye on BNNT and potentially using them in the future will benefit the new interplanetary missions of CubeSats.

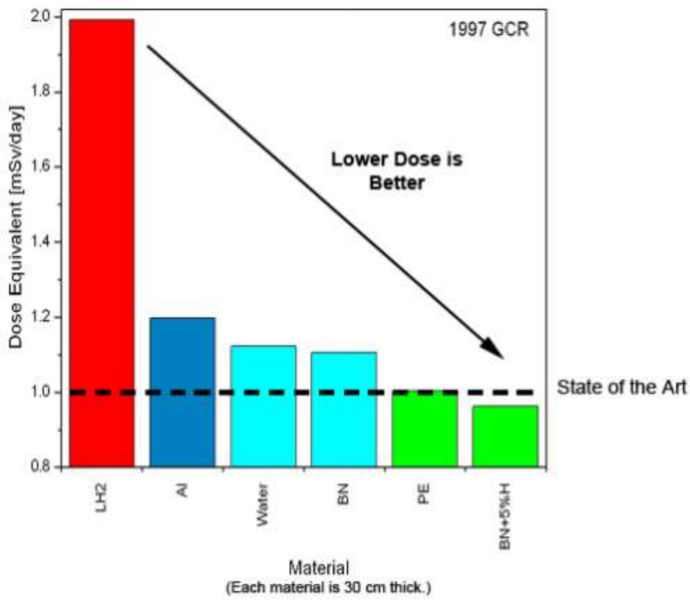

Figure 3.8: Shielding capacity of materials (Tiano et al. p.14, n.d.): hydrogen, aluminium, water, BNNT, Polyethylene and Hydrogen doped BNNT (from left to right).

Besides new material inventions, there are components of embedded systems that already mitigate spacecraft radiation induced malfunctions. Fault-tolerant techniques like implementing standard Watchdog system are already applied on CubeSats such as the RAX (Beningo J., 2010). The Radio Aurora eXplorer (RAX) is a 3U CubeSat with a volume. RAX was built using common off the shelf components. The flight computer (FCPU), consists of a TI MSP430F1611 16 bit micro-controller running at 8 MHz and consuming less than 5 mA in active mode. The RAX FCPU is monitored by a watchdog system in order to minimize system down time and risks due to transient faults. These faults can be caused by incoming radiation, stressing the importance of redundant system design besides just looking at the shielding capacity of the spacecraft bus.

Not only using the right hardware, also mission strategy and operations are important factors. As mentioned before in Chapter 2, the activity of the Sun depends on its 11 year cycle. Mitigating risk of a high ionization dose can simply be done by flying a satellite mission in low-solar times. Sadly this is only applicable for missions that last up to four years because the activity of the Sun will not stay low for long. Another limiting factor is the ability of the design team to be ready for a launch just before a solar minimum and the availability of a launch window. The right strategy can thus be difficult when planning a mission to the solar activity. What always helps, is applying the right operations on board, safer during operations. Using memory scrubbing and periodic resets to account for single event phenomena can save the mission from a malfunctioning satellite. In order to decide which countermeasures should be applied, the radiation shielding analysis is the starting point, since it can provide the radiation environment at component level.

3.4 Other CubeSat Design Factors for Interplanetary Flight

This section discusses other important factors to keep in mind while designing an interplanetary CubeSat mission.

The main purpose of the current CubeSat fleet is a fast and cheap access to space research and systems engineering. This thought is shared by many universities, institutions, companies and agencies around the world. However, the simplicity of the system might be lost when adapting the CubeSat design for interplanetary flight. Many subsystems available on CubeSat shop such as attitude determination and control, are intended for LEO operations and the sun sensors, star camera magnetometer have to be redesigned and engineered to fulfil the requirements of interplanetary flight. Navigation beyond LEO is another point of attention as the Deep Space Network is probably not available for CubeSats.

Another challenge is the communication between a CubeSat at e.g. The Moon and Earth ground stations. The free path loss for a Lunar trajectory is -38 dB and the transmit power shall thus have to be increased. Mitigation of this problem could be performed by using directional or deployable cameras, a larger ground station or by storing data. But by doing so, complicating the CubeSat mission. Other points of consideration are the environmental differences that might occur at other planets. CubeSats are usually not equipped with large solar arrays, but they might be required for flight towards planets more distant from the Sun in order to create enough power. That being said, it is still the question what the possible lifetime is of a CubeSat and especially outside Earth's environment. Lessons learned by pioneering missions such as MarCO by NASA will be of key importance in the CubeSat development.

3.5 Radiation Hardness of CubeSat electronics

This section is included to set a benchmark for the radiation dose that can be handled by a CubeSat and its electronics. Especially the electronics on board of the satellite are susceptible to upsets due to space radiation (section 2.2) when flying in interplanetary orbit. Not only will interplanetary missions of CubeSats be longer than their current applications in LEO, the electronics has to be able to fulfil the requirements of such a longer mission. More data are to be handled, FPGA-processing should be radiation hardened and memory capacity is to be increased (Staehle et al., 2013). For some state-of-the-art electronical parts, radiation hardness tests have been performed by Sinclair and Dyer (Sinclair and Dyer, 2013). Their results are summarized in Table 3.1 below.

Part Name	Instrument Type	Radiation Hardness
IR2104S MOSFET Driver	Driver	10krad: noticeable effect, 20krad: upper limit
LT3012 Linear Regulator	Linear Regulator	15krad: noticeable effect, >20 krad: upper limit
C8051F410 8-bit Microcontroller	Microcontroller	>20krad: upper limit
C8051F580 8-bit Microcontroller	Microcontroller	12krad: minor effects >20krad: upper limit
SN65HVD1781 RS485 Transceiver	Transceiver	14krad: noticeable effect >20krad: upper limit
ZXMN6A11DN8 Dual Power N-channel MOSFET	Field-effect transistor	Single-event upset from 105 MeV protons depositing 1 krad
SiM3C1XX 32-bit Microcontroller	Microcontroller	Latch-ups from 105 MeV protons depositing 1 krad
LT3437 DC/DC Converter	DC/DC Converter	15krad: noticeable effects >20krad: upper limit
DDR DRAM	Memory	Immune to solar event upsets

Table 3.1: Radiation hardness of CubeSat electronics during solar particle events from research performed by Sinclair and Dyer (Sinclair and Dyer, 2013).

From the studies of Sinclair and Dyer, it is concluded that after 10-15 krad, noticeable effects take place in the instruments presented. However, these are not mission-threatening. A benchmark is therefore placed at 20 krad, up to which the parts presented in Table 3.1 are still functional, albeit with some noticeable effects occurring. This value of 20 krad shall thus be of high importance when looking at the radiation results obtained in Chapter 7.

4. Simulation and Testing

During the rest of this thesis, the focus shall be on the simulation of different relevant material configuration and payload placement in a 6U configuration. The simulations have been performed using SPENVIS and FASTRAD.

4.1 The Space Environment Information System (SPENVIS)

The radiation environment in a reference mission and under different solar activity scenarios has been modelled by 'SPENVIS' (SPENVIS, 2017), the Space Environment Information System developed by the Royal Belgian Institute for Space Aeronomy – under an ESA contract.

The first step in SPENVIS, is always the definition of an orbit trajectory. With this as an input, one can choose to model several elements (SPENVIS, 2017):

- geomagnetic coordinates
- trapped proton and electron fluxes and solar proton fluences
- radiation doses (ionising and non-ionising) for simple geometries
- a sectoring analysis for dose calculations in more complex geometries
- damage equivalent fluences for Si, GaAs and multi-junction solar cells
- Geant4 Monte Carlo analysis for doses and pulse height rates in planar and spherical shields
- ion LET and flux spectra and single event upset rates
- trapped proton flux anisotropy
- atmospheric and ionospheric densities and temperatures
- atomic oxygen erosion depths

From these built-in models, one can thus perform a complete study about a specific CubeSat design. The results will be presented and discussed at a later stage. More thorough use of SPENVIS during this thesis is explained in chapter 3.

4.2 FASTRAD

FASTRAD is the second simulation tool used in this thesis. FASTRAD is developed by the firm TRAD (TRAD, 2017) from 1999 onwards and has received support by the European Space Agency. Thanks to the CAD Interface, the program can incorporate full 3D models and immerse them into the selected radiation environment. The radiation simulation software estimates the dose and displacement damage of electronics and material of spacecraft, such that the weak spots of a design can be assessed. By selecting sections or even subsystems of a spacecraft, the aluminium mass equivalence can be determined that is required for the shielding of the section or subsystem.

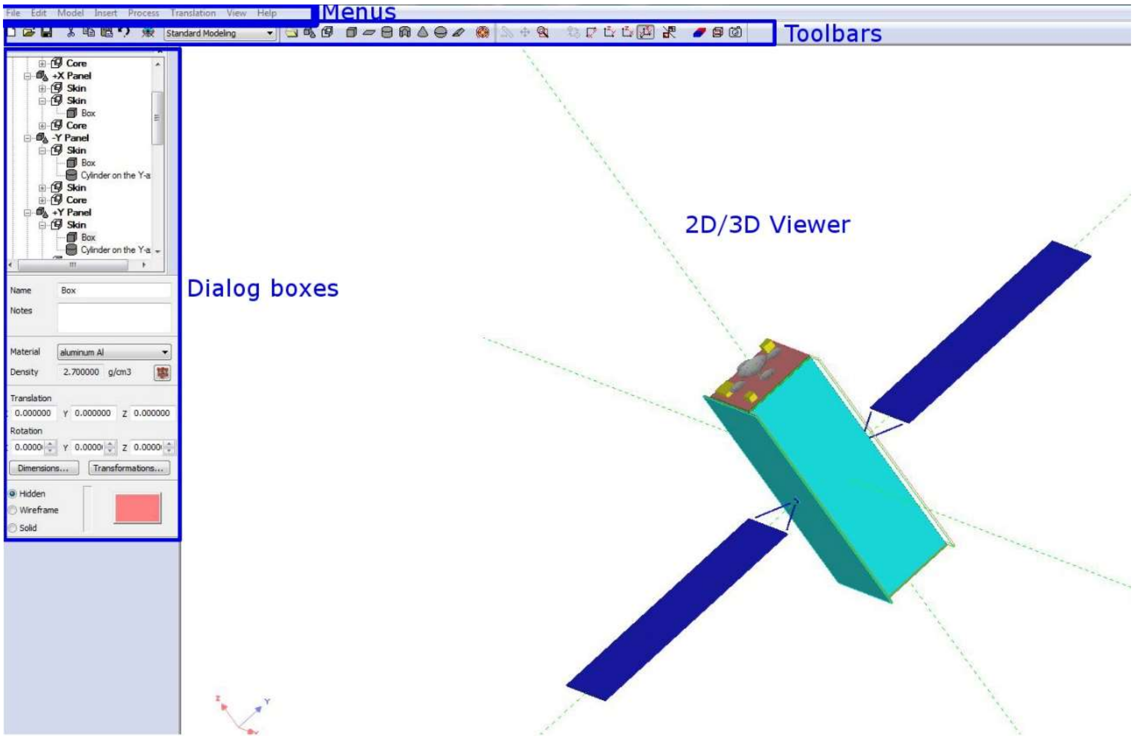

Figure 4.1: Insight in the modelling environment of FASTRAD. (TRAD, 2017)

The models that were created are presented in chapter 4, where the use of FASTRAD for this thesis and the choice for the creation of models is published.

5. SPENVIS: creating the radiation environment

5.1 The Orbit Parameters

In this thesis the orbit type is chosen to be interplanetary. The orbit altitude for an interplanetary flight as chosen in the mission definition is a default value of 90,000 km in SPENVIS. This interplanetary orbit lies outside the Van Allen-Belts, setting the spacecraft free of any trapped particles in the Earth Magnetosphere. The orbit parameters selected in SPENVIS are shown in Fig. 3.1.

Mission overview
Orbit around: Earth
Number of mission segments: 1
Mission start: 01/01/2012 00:00:00
Mission end: 31/12/2015 00:00:00
Mission duration: 1460.00 days (4.00 years)
Satellite axis: velocity vector

Mission segment 1: Solar Maximum 2012-2015
Orbit type: near Earth interplanetary
Distance from the Sun: 1.00 AU
Orbit start: 01/01/2012 00:00: 0.0
Segment end: 31/12/2015 00:00: 0.0
Segment length: 1460.00 days

Figure 5.1: Tables of the 'mission overview' provided by SPENVIS after orbit generation.

Radiation Sources and Effects: mapping the radiation environment

Once the interplanetary orbit is chosen (for all scenarios) and the mission duration is specified (depending on scenario), the coordinate grid of the project is set and it can be used for all models that can be activated in SPENVIS. The following step is the generation of the radiation environment data, which can be determined using the 'radiation sources and effects' package. In SPENVIS, there are four radiation sources:

1. Trapped particles – calculated for each mission segment;
2. Short term solar fluxes – calculated for peak fluxes;
3. Long term solar fluences – calculated for the full mission duration; and
4. Galactic cosmic rays – calculated for each mission segment.

As this thesis focuses on interplanetary orbits for CubeSats, the first radiation source – trapped particles – can be discarded as these particles are only present in Earth orbits. The four scenarios discussed in the next section of this chapter shall thus only focus on the three latter radiation sources: As a model for the solar particles, the SAPPHIRE-model is selected. This model is a 2018 update, which looks at the 0.1 MeV-1.0 GeV spectrum. The model shall be discussed in section 3.2 of this chapter, to prove its validity. For the galactic cosmic rays incoming on the spacecraft in interplanetary orbit, the CREME86-model is selected. This model shall be discussed later as well.

Ion range

Although protons and Helium ions are the dominant contributors to the (solar) particle flux, higher Z-particles such as Iron (Fe) can contribute a significant part to the total dose on the spacecraft For this reason the entire spectrum is selected.

Short term solar effects: peak fluxes

In order to create a representative environment for a worst-case scenario in which the spacecraft shall operate, the short term SPE are of crucial importance. These strong effects are causing peak fluxes of solar particles on the material of the satellite. Therefore, this radiation scenario is studied with extra care, by studying the radiation source with two models. The first is the peak flux model of SAPPHIRE and the second one is the 1-in-n-years SPE-model of SAPPHIRE .

The background information and differences between the two models are published in a later section of this chapter, where the input model SAPPHIRE is discussed.

Long term solar particle fluences

The total fluence of solar particles during the mission epochs of the four scenarios selected in SPENVIS is calculated using the SAPPHIRE total fluence model. The model uses the mission epoch and establishes the period of solar maximum within this mission epoch, keeping in mind that a solar maximum period lasts seven years for SPENVIS and is from solar maximum minus 2.5 years till solar maximum plus 4.5 years. The inputs for ion range and magnetic shielding have been stated before, but a new input is the confidence level of this long term fluence model. This factor is the probability (in percentage) of the proton fluence not being overestimated. Historical data is used to establish this proton fluence.

Galactic Cosmic Rays

The third and final source of radiation in interplanetary orbit, comes from galactic cosmic rays (GCR), which are modelled using CREME86-model. The CREME96-model automatically pre-sets the time period to be the solar minimum of 1977, thus not adhering to the time-frame set in the mission design. The CREME86-model follows the mission epoch set in SPENVIS and does not automatically select a solar minimum period as the modelling period. By selecting the CREME86-model, the solar maximum scenario can be modelled as well and by using the same model, a comparison can be made between the scenarios. Again, the ion range for this model shall be as complete as possible: H to U. Magnetic shielding is off, as an interplanetary orbit – outside the magnetosphere – is considered.

5.2 The SAPPHIRE Model

In this section the Solar Accumulated and Peak Proton and Heavy Ion Radiation Environment (SAPPHIRE) model will be discussed. The main features of the model as well as how SAPPHIRE, has been applied to this thesis will be presented.

Solar Radiation Data

The dataset on which SAPPHIRE is modelled, is the second version of the SEPEM Reference DataSet (SRDS). This SRDS has been validated by Rodriguez et al. [2017]. The SAPPHIRE model uses inputs from several in-situ measured data sets (GOES/SEM and IMP-8/GME). This was done to take advantage of their best features and to address some issues that occur in the models of solar energetic particles, available before SAPPHIRE was introduced [Jiggens et al. 2018]:

1. The saturation of science-quality instrumentation during high flux periods.
2. Uncertainties in the response of monitor-quality data, given broad energy bins.
3. High data spikes and dead-time effects.
4. The variability of SEPs iss not sufficiently mapped by the limited timespan

The cleaned data of SRDS by means of the combination of aforementioned data sets, results in a homogenous reference data set with a mapping time from 1974 to 2016. The data of SRDS is available by Heynderickx et al. [2017].

Solar Maxima and Minima

The definition of the solar period in SAPPHIRE is equal to that in SPENVIS; the maximum lasts for 7 years, with 2.5 years prior to peak value and 4.5 years after the peak value. This definition is set by Feynman et al [1990]. The reason for this clear distinction between the solar minima and maxima during the solar period is the order of magnitude difference in proton fluences between the two. This is supported by the documentation of SPEs in the 'SEPEM reference event list' [http://sepem.eu/help/event_ref.html]. In this documentation, the number of SPEs during solar maxima between 1974 and 2016 (the SAPPHIRE time-span) is 266. Only 29 occurred in solar minimum periods, about one tenth of the total amount of SPEs.

Background Filtering

As a final note on the model data, it has to be mentioned that the background data of GCRs are filtered out. By taking the mean flux during the week around the SPE and subtracting this from the total flux during the SPE, the GCR flux is filtered out. In the Figures 5.2 and 5.3, the difference between the flux including GCR background fluxes (black) and excluding GCR background fluxes (yellow) can be seen. It is clear that lower energetic SPEs are more widely spread in time, as a significant part of their flux is filtered out along with the GCR fluxes. Higher energy, shorter, SPEs show no effect of the filtering, as the contribution of GCR fluxes to these total fluxes are negligible.

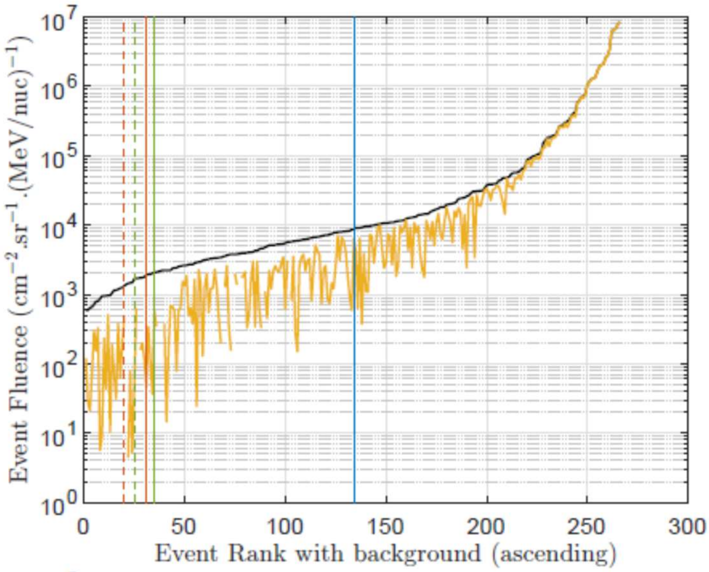

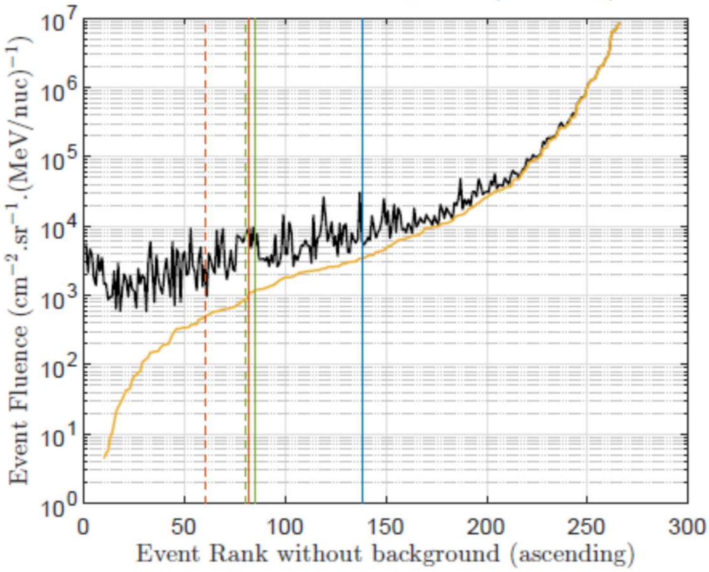

Figures 5.2 and 5.3: SPE Fluxes before (black lines) and after (yellow lines) filtering of background GCR fluxes.

1-in-n-years SPEs

Besides the update in datasets used for SAPPHIRE, an additional feature has been added to the model. This involves the derivation of 1-in-n-years SPE flux outputs. This extra feature is helpful for users of the model that want to test their satellite under conditions that occur once in 'n'-years. For use in SPENVIS, the user has the choice between 10;20;50;100;300;1000 and 10000 for 'n'. In Figure 5.4 the fluence during a 1-in-n-years SPE for particle energies from 0.1MeV up to 1.0GeV is shown.

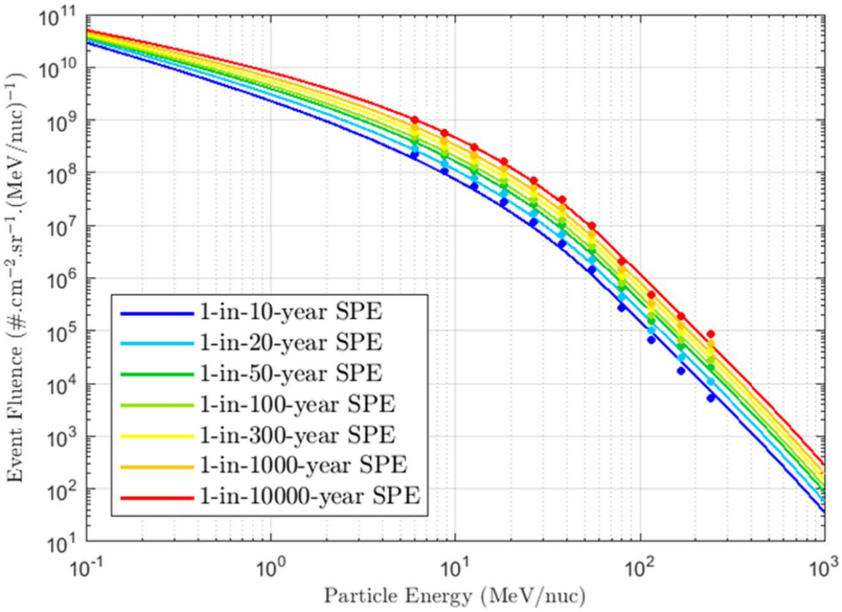

Figure 5.4: Particle energy against the event fluence for several 1-in-n-years solar particle events.

These 1-in-n-years models give insight in the radiation levels induced by SPEs in periods of n years. This insight in peak fluxes of solar particles, is easy to understand and helpful for the user of the model. However, one should thoroughly consider which value for n is most appropriate for the specific space mission. In order to do this, a comparison with existing models on these peak fluxes is performed by Jiggens et al. [2018]. Comparison of the peak flux of SPE in both the CREME96-model and the ESP-PSYCHIC 'Design Limit' model give a good fit with the 1-in-100-years SPE flux by SAPPHIRE. This leads to two things, one is the verification of the SAPPHIRE model for these 1-in-n-years fluxes and second is the use of this model in this thesis. Because of the good fit between the 1-in-100 years SPE flux and the other two 'worst-case' models, the choice has been made to use this 1-in-100 years model to simulate the peak radiation environment around the satellite during its mission lifetime. Figure 5.5 provides the graph to the comparison between the three worst-case models.

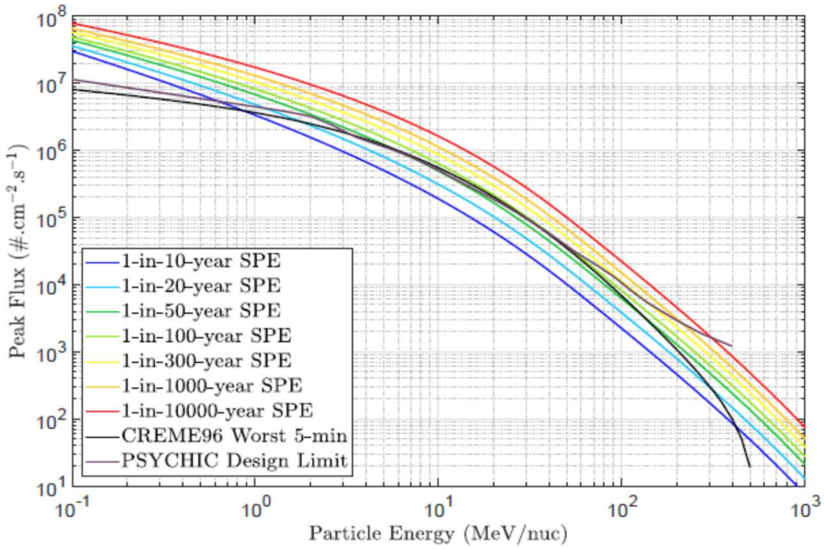

Figure 5.5: Overview of the 1-in-n-years peak flux models of SAPPHIRE and the two worst-case models of CREME96 and ESP-PSYCHIC. Clearly visible is the close fit to the 1-in-100 years peak flux model of SAPPHIRE.

5.3 SPENVIS Outputs: Particle Fluxes

In section 5.1, the mission definition is performed: the orbit is set to be interplanetary. Now that the working principle of SPENVIS is clear, radiation environments can be determined for the CubeSat on this interplanetary mission by setting the time-frame over which the data is retrieved. Due to the highly fluctuating activity of the Sun and the implications for SPE and GCR fluxes, the several periods of the solar cycle are looked at. Four scenarios and their respective time-frames are defined:

1. Solar Maximum (2012-2015, four years in total)
2. Solar Minimum (2006-2009, four years in total)
3. 11 years solar cycle (2006-2016)
4. 1-in-100 years Solar Particle Event (worst-case)

In this section, the radiation environment for all these four is presented graphically and discussed briefly in sections 5.3.1 to 5.3.4. The three different types of radiation shall be covered for all three scenarios. These are:

5.3.1	Short term: Solar Particle Events	Figure 5.6
5.3.2	Long term: Solar Proton Fluences	Figure 5.7
5.3.3	Galactic Cosmic Rays	Figure 5.8

The worst-case 1-in-100 years SPE scenario is presented in section 5.3.4.

5.3.1 Solar Particle Events – Peak Fluxes

The short term peak effects discussed in this section are the worst-case scenarios within the mission epochs as defined at the start of this section. The solar radiation effects for these three scenarios are found in Figure 5.6, where the output from SPENVIS for the short term solar fluxes of the three scenarios is combined into one plot.

From this plot, it is obvious that the peak fluxes are fairly independent of solar maximum or minimum periods. The graphs in figure 5.6 are all in the same order of magnitude and never differ more than that. The overlap in the graphs clearly shows that.

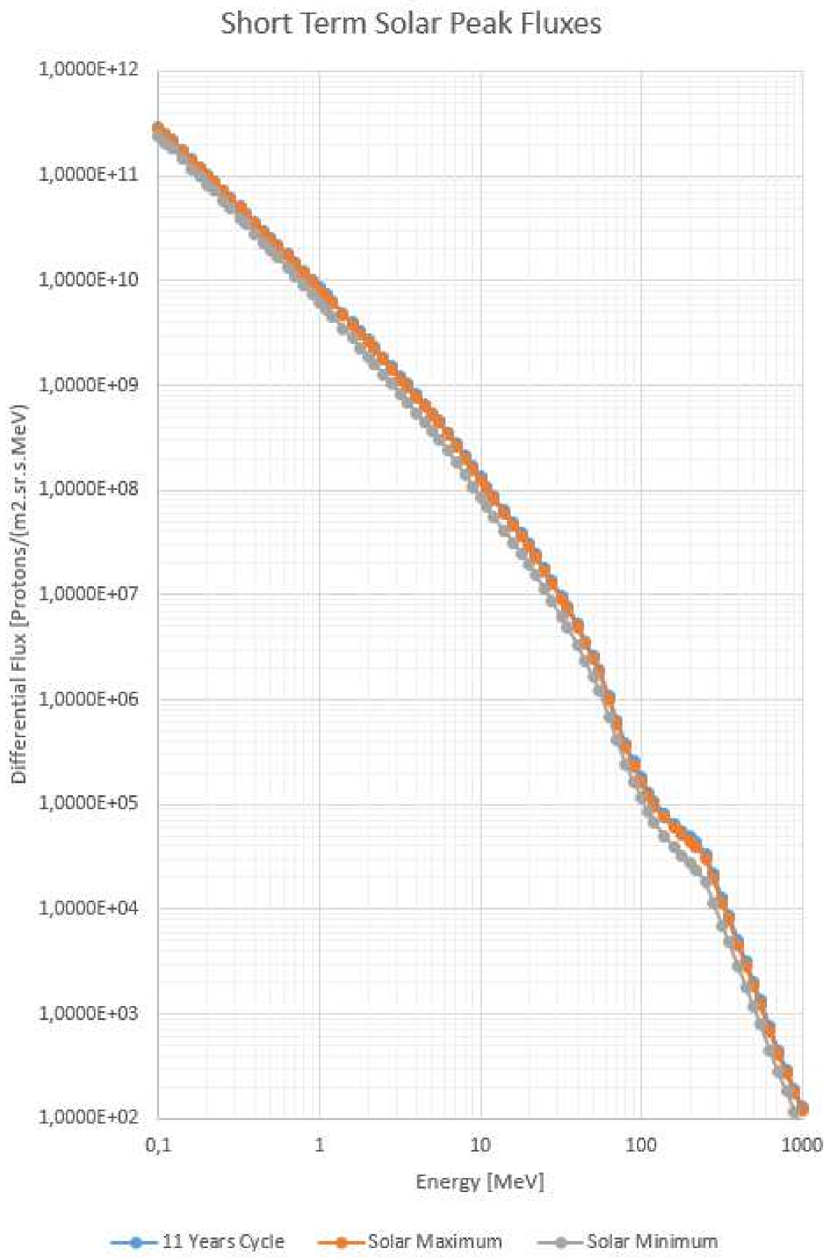

Figure 5.6: Worst-case solar proton fluxes for the three scenarios.

5.3.2 Solar Particle Fluences – Mission Epoch

In Figure 5.7, the proton fluence is given for the three scenarios, obtained using the SAPPHIRE fluence model. In contrast to the short term phenomena, the long term models differ significantly. The fluence during solar maximum is about twice the fluence during solar minimum periods. The solar cycle scenario has slightly higher fluences than the solar maximum fluences, but these are restricted to a further increase of about 30%. This makes sense, as the highest proton fluence period during a solar cycle is the solar maximum period and this is already incorporated in the solar maximum scenario.

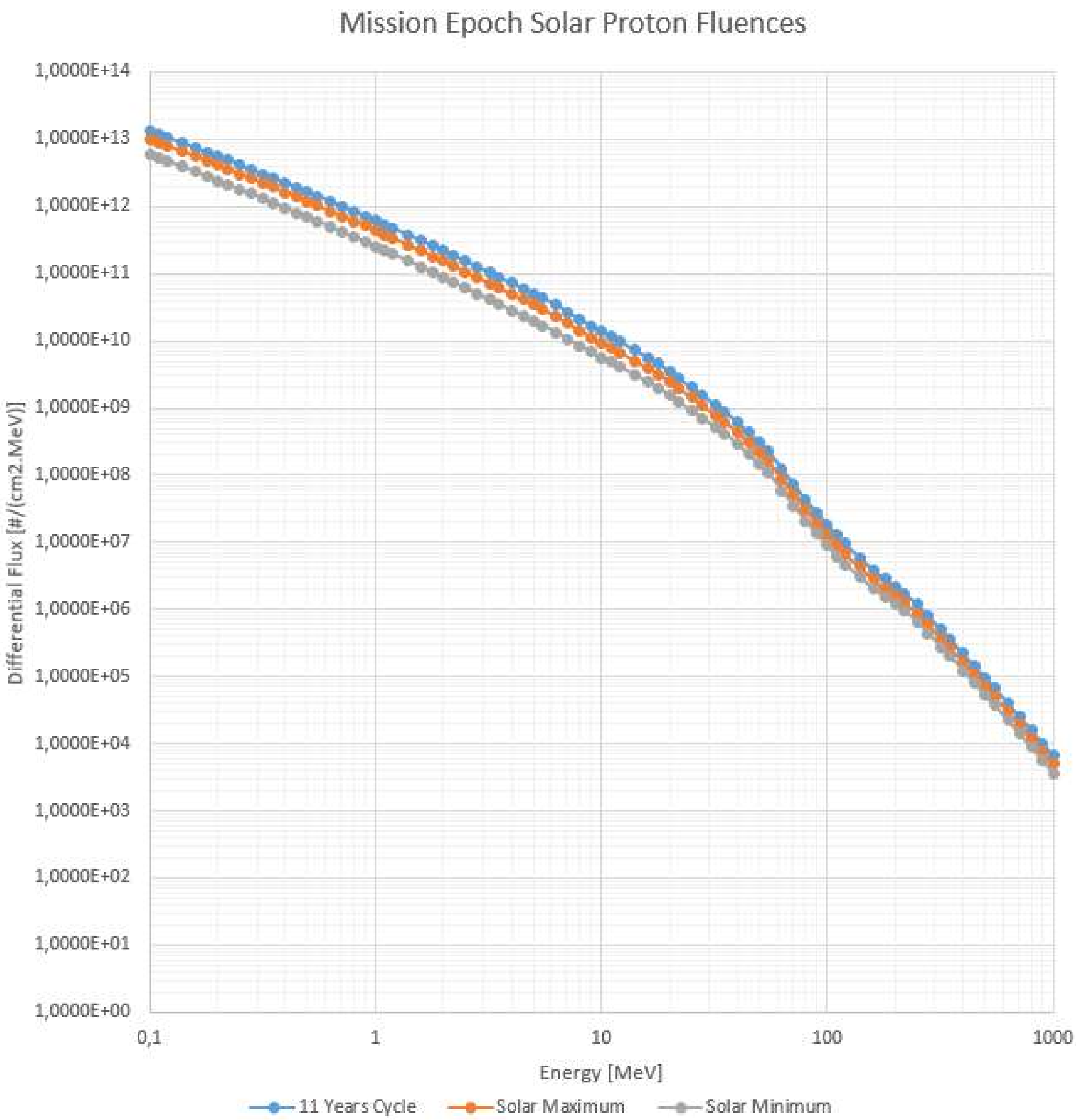

Figure 5.7a: Solar Proton Fluences during (blue) 11 years cycle, (orange) four years in solar maximum and (pink) four years of solar minimum. Note the difference is less than one order of magnitude.

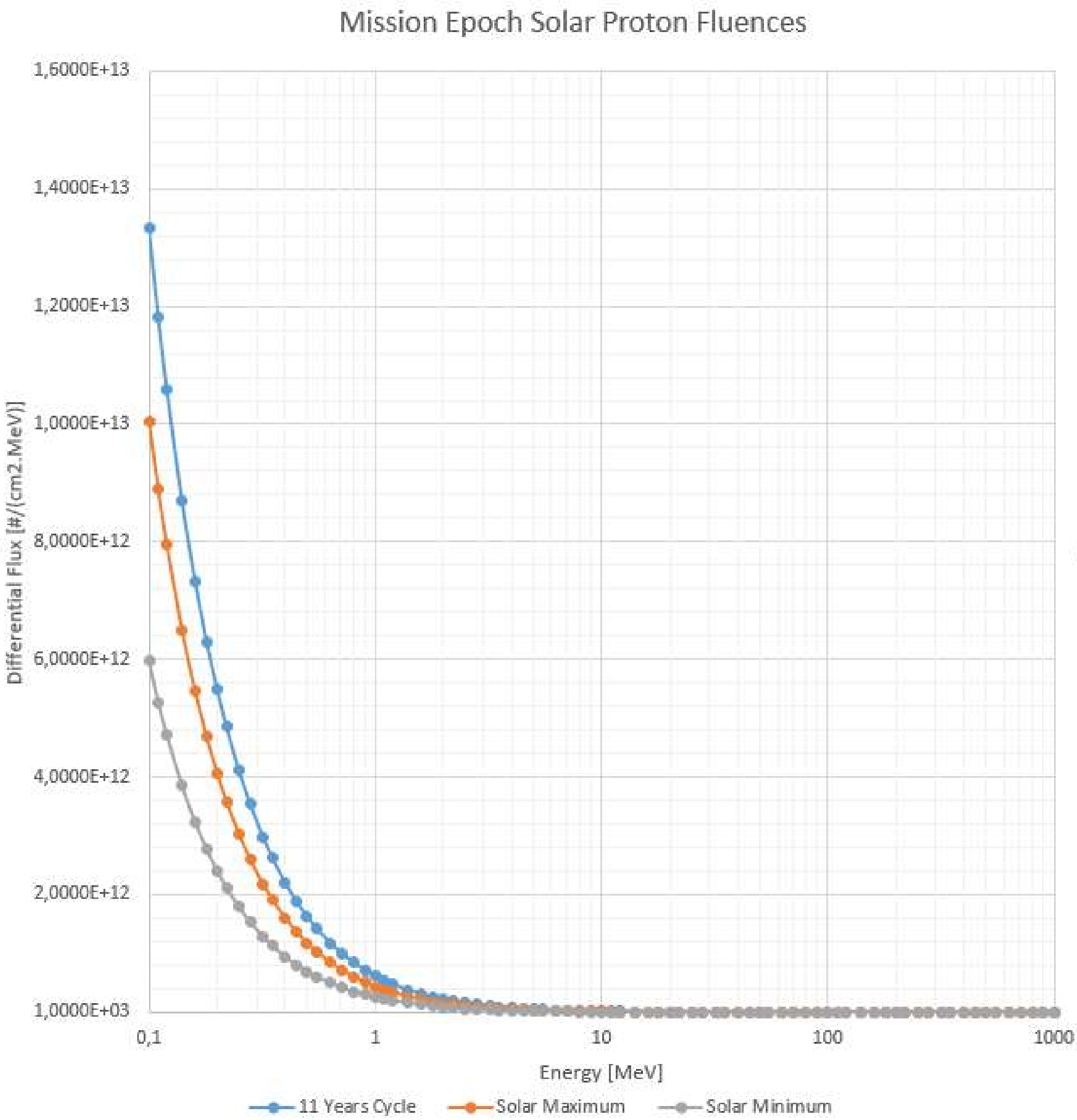

Figure 5.7b: Solar Proton Fluences during (blue) 11 years cycle, (orange) four years in solar maximum and (pink) four years of solar minimum. Note the difference is less than one order of magnitude.

5.3.3 Galactic Cosmic Rays

In Fig. 3.14 and 3.15 the peak in the GCR flux can be noticed, which is highest for energies of the order 100-1000 MeV. This stresses the high energy of these particles when entering the solar system. The peak is slightly lower (around 400 MeV vs. 550 MeV) for H during solar minimum, as the lower activity of the Sun allows these lighter less-energetic ions to enter the solar system.

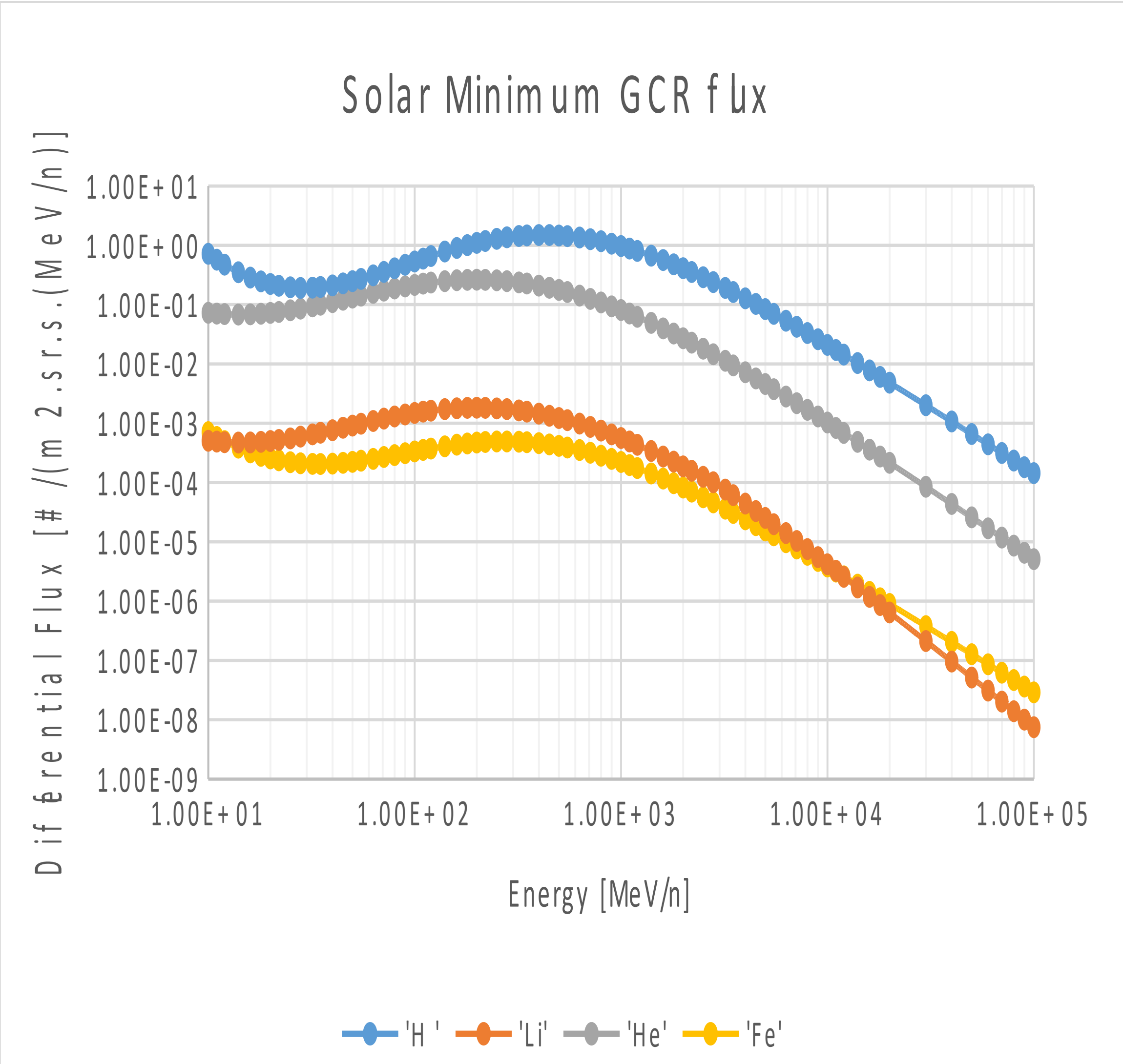

Figure 5.8: GCR spectra for H, He, Li and Fe. Note the dominant presence of lighter ions and the peak value of the fluxes around 100-1000 MeV. Also note the high order difference between H-fluxes (blue) and Li(red)/Fe(yellow) GCR fluxes.

5.3.4 1-in-100 years SPE-fluxes for elements H to Fe

Table 3.16 shows the magnitude of the differential flux per element (Z=1 to 26) for a 1-in-100 years solar particle event. Obvious are the high fluxes for H and He, which are 4 and 2 orders of magnitude higher respectively than the fluxes of any other elements from Li (Z=3) up to Fe (Z=26). Figures 5.9 And 5.10 graphically show the differential fluxes for the elements H and He because these fluxes are far higher than the other elements in the particle flux. The output from SPENVIS for this 1-in-100 years flux is independent of chosen time-frame. This is caused by the uniqueness of this event and because of the timeframe of one solar cycle of 11 years that is shorter than the period over which Sapphire selects its worst case flux of 1-in-100 years.

Table 5.16: Differential flux of ions H (Z=1), He (Z=2) and Li to Fe (Z=3 to 26) during 1-in-100 years SPE

		Differential Flux [#*m-2sr-1s-1 (MeV/n)-1]				
Element	Z	0.1 MeV/n	1 MeV/n	10 MeV/n	100 MeV/n	1 GeV/n
H	1	2.678E+11	5.826E+9	7.110E+08	1.430E+05	6.194E+01
He	2	7.401E+9	1.697E+8	1.690E+06	1.241E+03	1.009E-01
Li to Fe	3-26	4.142E+0 to 9.925E+7	9.498E-2 to 2.276E+6	1.088E-3 to 2.439E+4	2.353E-06 to 1.034E+1	2.422E-10 to 4.333E-3

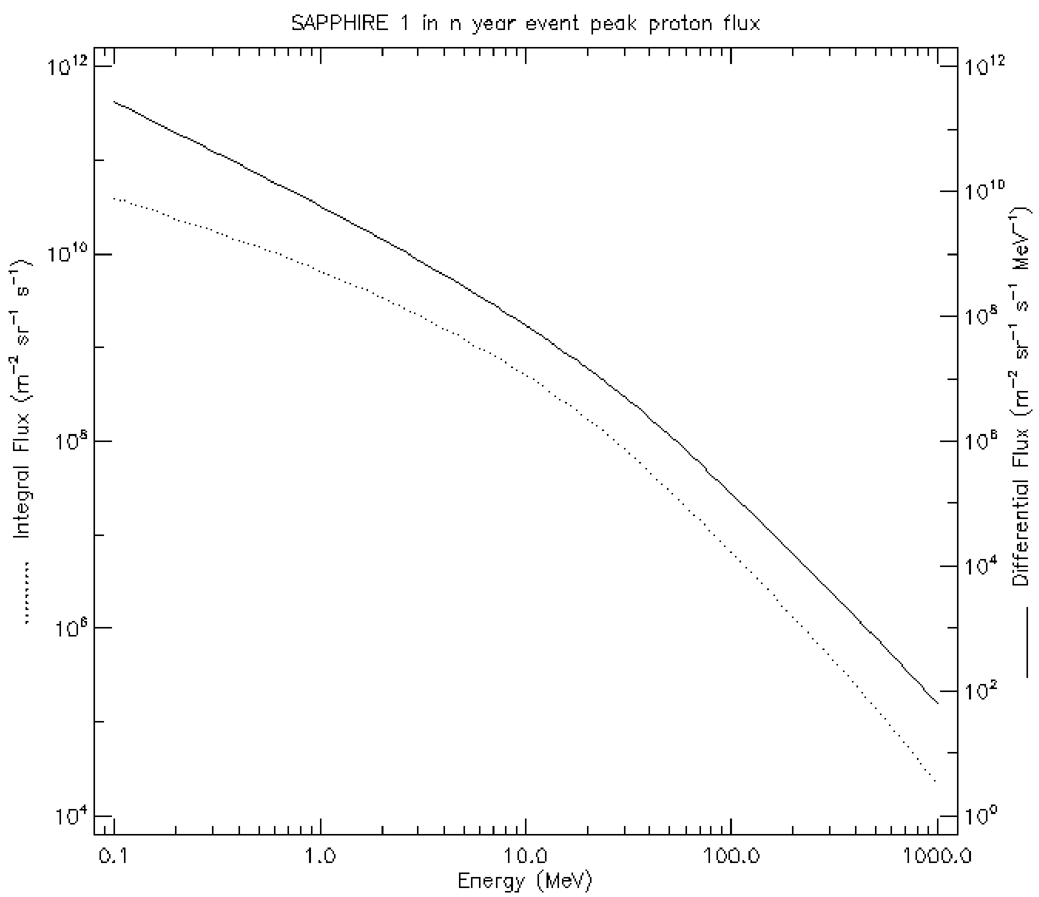

Figure 5.9: Flux of protons during a 1-in-100 years SPE.

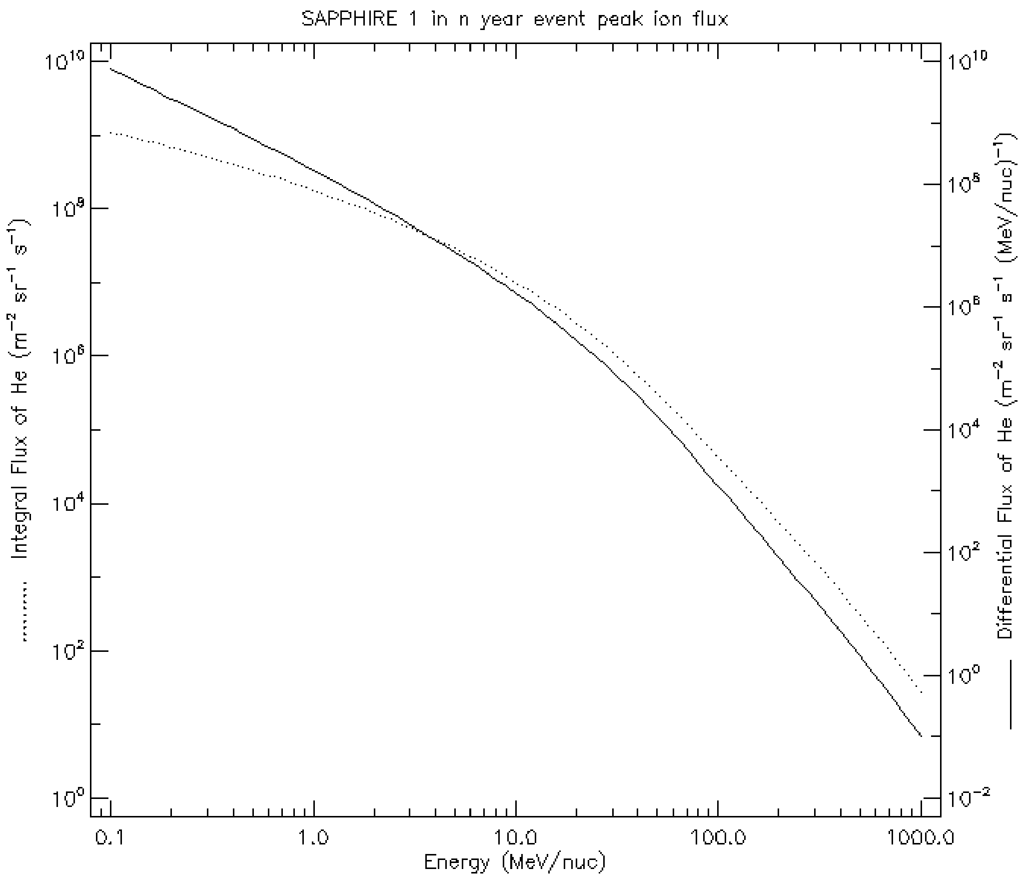

Figure 5.10: Flux of He-ions during a 1-in-100 years SPE.

5.4 Radiation Environment and Event selected for Simulations in Fastrad

In the previous sections of this Chapter 5, the interplanetary orbit (5.1), the radiation model Sapphire (5.2) and the outputs for several mission scenarios (5.3) have been given. It is now time to select one radiation environment that shall be used in the radiation simulations in Fastrad (Chapter 6) and to define a time duration during which this radiation environment has to be applied during the simulations.

From section 5.3, it has become clear that the worst-case scenario of a 1-in-100 years solar particle event is of interest because of its highest proton flux. Also, since it is independent of the time-frame set in SPENVIS, it is a universal worst-case which has to be considered during the development of any space mission. The radiation environment of this 1-in-100 years solar event is published in Appendix B, where one finds the differential flux of protons in the defined orbit for the full particle energy spectrum [MeV].

Later in this thesis, it shall become clear that the Forward Monte Carlo simulations – which are explained later - in Fastrad require a defined time-frame during which the radiation environment of the 1-in-100 years SPE acts on the model. To define this time-frame, an extra literature study has taken place to make sure a correct time-frame is used for a high energy SPE such as the one selected from SPENVIS.

First, there are Neal (Neal at al., 2008) which discusses the importance of the prediction of the dose temporal profiles of large SPEs. Based on the SPEs in 2000 and 2001, they look at the constitution of these SPEs and define a 90h period over which they are active. Graphical results are available in figures 5.11 to 5.13. Mewaldt (Mewaldt et al., 2005) has studied large SPEs' particle spectra during five SPEs in October-November 2003, all lasting hours up to two days. Thirdly there is the study of Emslie (Emslie et al. 2004), which studied the energy flux of solar flares and coronal mass ejections in interplanetary space during April 2002. The proton flux spiked during several hours up to two days during these events in 2002. These three sources, together with literature presented in Chapter 2, lead to the conclusion that large SPEs spike proton fluxes in interplanetary space during several hours up to four days. That is why in later stages of this thesis, a time-frame of four days is set for the simulation time. The proton flux per second as obtained through SPENVIS and published in Appendix B is then applied in the simulations for a four day period.

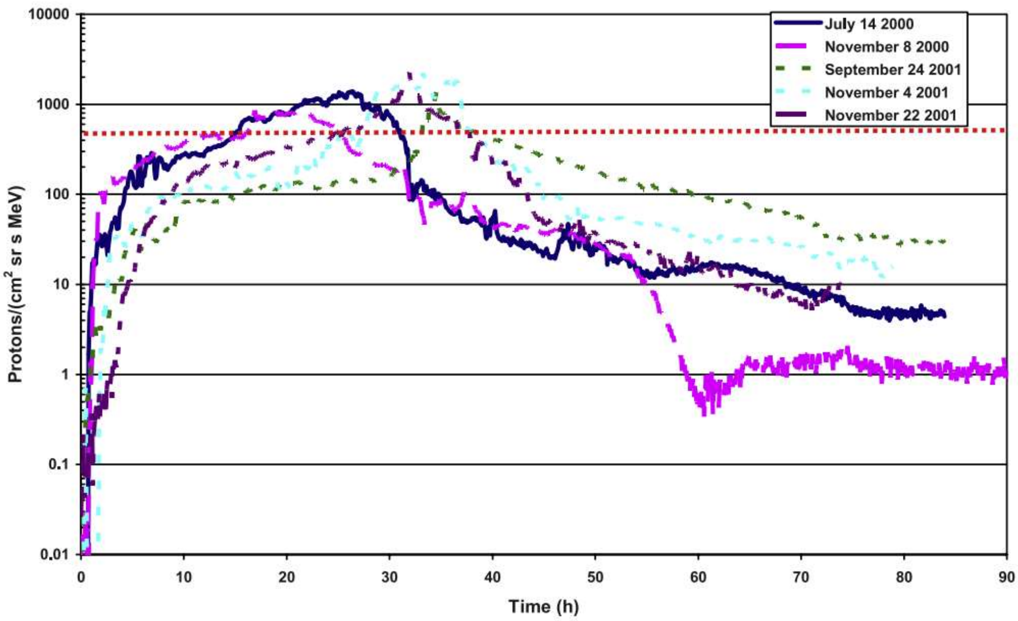

Figure 5.11: Proton flux during the 2000-2001 large SPEs for the energy spectrum 8.7-14.5 [MeV] (Neal at al. 2008).

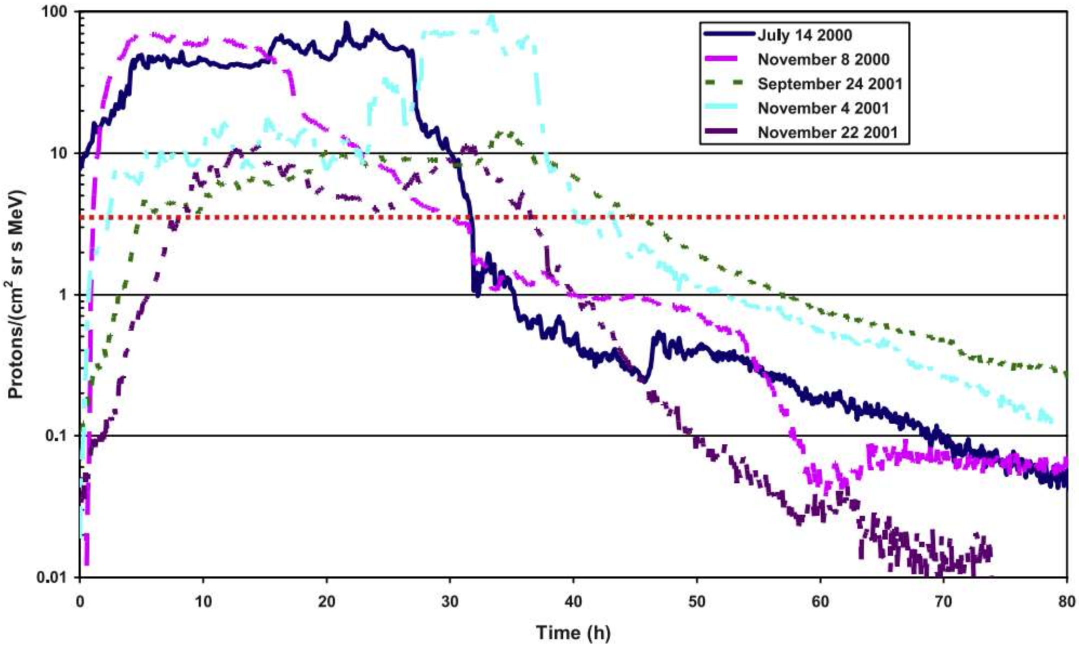

Figure 5.12: Proton flux during the 2000-2001 large SPEs for the energy spectrum 39-82 [MeV] (Neal at al. 2008).

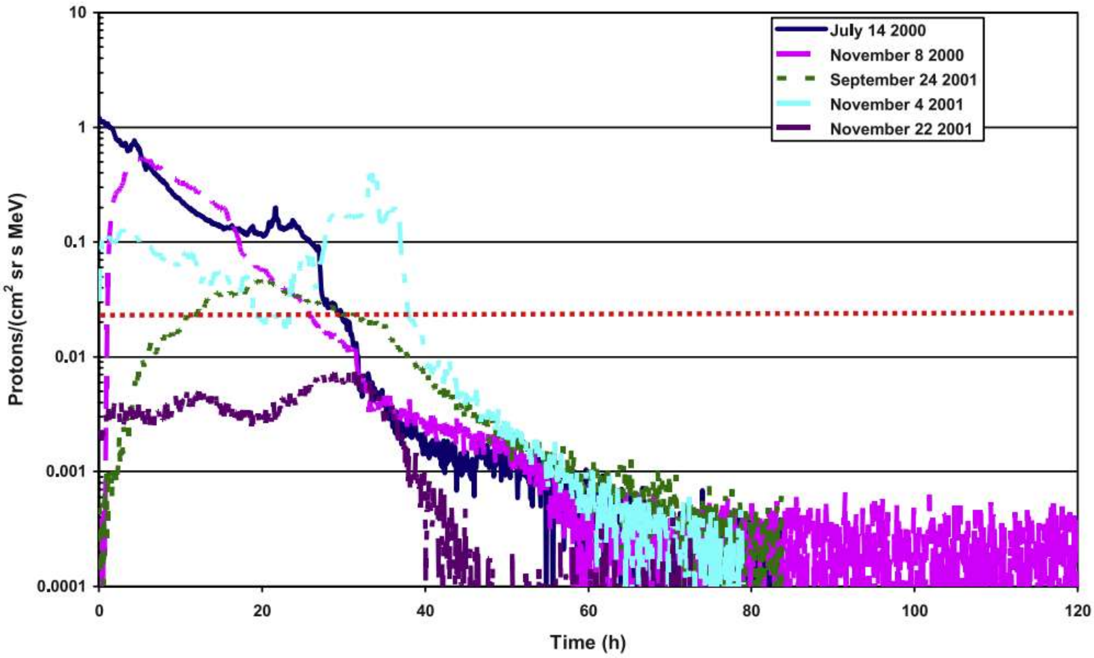

Figure 5.13: Proton flux during the 2000-2001 large SPEs for the energy spectrum 110-500 [MeV] (Neal at al. 2008).

6. Fastrad: Radiation Shielding Analysis

This chapter discusses how FASTRAD has been used in the work flow diagram of this thesis. Once the use and contribution of FASTRAD in this thesis are clear, the simplified CubeSat models created in FASTRAD are presented in section 4.2. Finally, section 4.3 presents the geometry of the final (sophisticated) model of a CubeSat, as obtained through ISIS Space. This model serves as the main test case for radiation deposition later in this thesis.

6.1 Simulation Techniques in Fastrad

Simplified models of CubeSat are created in the FASTRAD environment (section 4.2) to test material choices and verify the method of operation in Fastrad. Besides these simpler models, a state-of-the-art 6U CubeSat model is presented in section 4.3. The results obtained by the SPENVIS radiation environment simulation are used as input to Fastrad to model the deposited radiation load on the spacecraft models.

In this thesis, two simulation techniques are used:

1. Ray Tracing and Sector Shielding Analysis which provides:
    a. a dose-file: an overview of the received radiation at each detector location in the model, and;
    b. a sector-file: an overview of the sectors of the model that are penetrated by the rays travelling towards each detector.
2. Forward Monte Carlo Simulation which provides:
    a. An overview of the deposited radiation dose in each location of the satellite model.
    b. A visualization file that plots the calculated deposited radiation per part onto the model.

The calculated radiation loads on them model can be seen through the post-processing application of Fastrad. For both simulation techniques, a different form of visualization is available. In case of the ray-tracing and sector shielding analysis, this allows the user to see the model with particle rays entering the environment. By visually allowing users to see the path of entry of rays, the designer can see where material has to be added or where the radiation load is highest on the model for each detector location. Figure 6.1a shows this ray-tracing analysis for one of the analyses performed during this thesis. In this figure, the 1U payload model is shown. The active detector on which radiation is projected is situated at one of the corners of the payload. It is clearly visible that the payload itself, but also the overlaying CubeSat bus structure are providing radiation shielding to this spot in the model. The rays that are coming in at a larger angle have to travel farther trough the CubeSat material and are therefore posing a smaller thread to the specific detector location. Figure 6.1b shows the visualization of a Forward Monte Carlo simulation on some parts of the 6U CubeSat model. In this case, the deposited dose of each part of the model can be seen and in this case, there is even a gradual change of deposited dose visible in the rib in the centre of the picture.

A more specific work-flow diagram in Fastrad has been added in Appendix G.

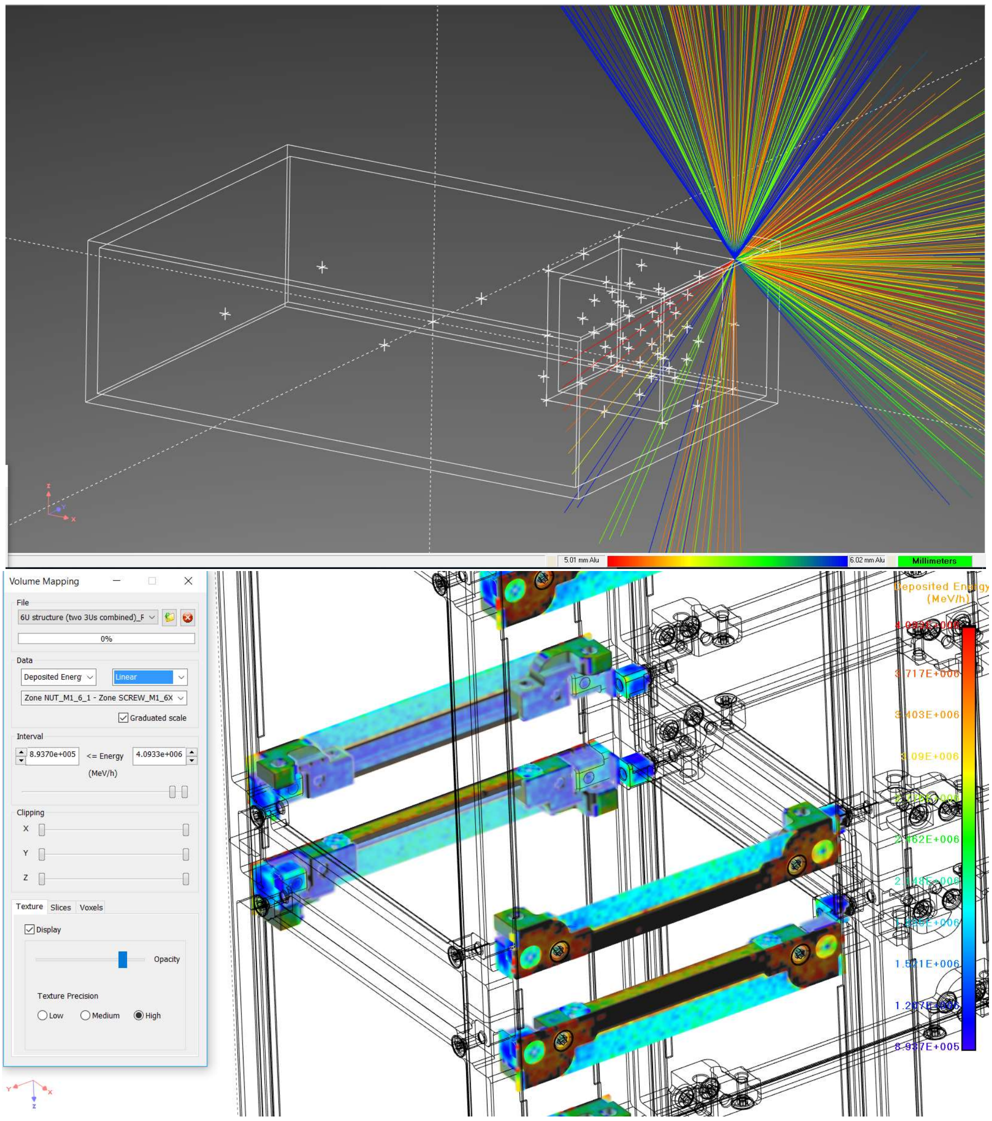

Figures 6.1a+b Visualizations from ray-tracing (top) and Monte Carlo methods (bottom) in Fastrad.

The large difference between the two methods of ray-tracing and forward Monte Carlo simulation, is the location at which the deposited dose is measured. During a ray-tracing simulation, one uses a sector analysis to come up with the radiation dose at a particular point in the model. This point has been defined by the user as a designated measuring point. The Forward Monte Carlo method uses the geometry of the model to measure the deposited dose within the parts of the model. Both methods are used because it provides a fuller picture of the radiation deposition in the model. The Forward Monte Carlo method gives an overview of which parts might require more shielding. The ray-tracing method gives an overview of the path through the model that a particle travels towards each point before depositing its dose. Hence, combining these two sets of information can lead to improved shielding for specific locations or parts in the CubeSat model.

6.2 Simplified CubeSat Models

The first case studied was a simplified geometry model of a 6U type CubeSat which was approximated to a parallelepiped.

As a reference size, the 6U CubeSat of ISIS has been chosen. ISIS is one of the world leading providers of CubeSat materials. The outer dimensions of the structure were the input for the box structures that were used in the modelling. As you can see from the table, these outer dimensions are a length of 340.5 [mm], width of 226.3 [mm] and height of 100.0 [mm].

6U CubeSat Bus Structure ISIS Characteristics	
Primary + Secondary Structure Mass	1100 [grams]
Outside Envelope (l x w x h)	340.5x226.3x100.0 [mm^3]
Inside Envelope (l x w x h)	96x96x89.4 [mm^3] for all 6 units
Thermal Range (min-max)	-40 to +80 [°C]

Figure 6.2 and Table 6.1: ISIS 6U CubeSat and its characteristics.

In this simple model, different material choices and payload configuration were analysed. Three materials have been analysed: Aluminium, Polyethylene and Copper. Aluminium is the state-of-the-art material for current CubeSats and it is used as reference. Polyethylene is a polymer which has other chemical benefits, such as the acceptance of electrons due to the presence of hydrogen in the molecules. Then Copper, which is a heavy metal and therefore has properties beneficial for shielding against heavy-ion radiation. It has to be noted that the density of copper is very high relative to the others and thus the amount of copper used has to be limited.

Four pure Aluminium boxes are modelled with respective thicknesses of 1, 2, 3 and 5 millimetres. These are boxes 1 to 4.

Then three aluminium boxes with a middle layer of polyethylene are chosen, to see how polyethylene has its influence on the radiation shielding and how much the aluminium and polyethylene contribute to this shielding. These are boxes 5 to 7.

Lastly, thin copper layers are included in the sandwich, between the aluminium and polyethylene layers. This way, the sandwich structure might be able to shield the inside structure for heavier ions, which as we learned from the background study, are best shielded using heavier metals. These last three material configurations are models 8 to 10.

#	Layer 1 Material	[mm]	Layer 2 Material	[mm]	Layer 3 Material	[mm]	Layer 4 Material	[mm]	Layer 5 Material	[mm]	Total mm-Al [mm-Al]
	Box Materials for 6U CubeSats [0.3405m x 0.2263m x 0.1000 m]										
1	Aluminium	1.0									1.0
2	Aluminium	2.0									2.0
3	Aluminium	3.0									3.0
4	Aluminium	5.0									5.0
5	Aluminium	0.5	Polyethylene	0.5	Aluminium	0.5					1.174
6	Aluminium	0.5	Polyethylene	1.0	Aluminium	0.5					1.348
7	Aluminium	1.0	Polyethylene	1.0	Aluminium	1.0					2.348
8	Aluminium	0.5	Copper	0.1	Polyethylene	0.8	Copper	0.1	Aluminium	0.5	1.943
9	Aluminium	1.0	Copper	0.1	Polyethylene	0.8	Copper	0.1	Aluminium	1.0	2.943
10	Aluminium	1.0	Copper	0.1	Polyethylene	2.8	Copper	0.1	Aluminium	1.0	3.639

Table 6.2: The ten material configurations of the models. Models 1 to 4 are state-of-the-art as only Aluminium is used. Models 5 to 7 include Polyethylene and in models 8 to 10 Copper is added.

The consequences of the choices for the material models are apparent in the total mass and inside volume of the created models 1 to 10. These results are presented in table 4. The numbers in table 4 are of importance in a later stage, where the material models' radiation shielding performances are analysed. However, it is a good start to keep in mind what the mass consequences are of the choice for Copper or Polyethylene and to see what the available volume is for payloads.

#	Material(s)	Thickness [m]	Mass [kg]	Inside X [m]	Inside Y [m]	Inside Z [m]	Volume [m^3]	Volume [%]
	Structural Characteristics of CubeSat Models							
1	Al 1.0mm	0.001	0.715	0.3385	0.2243	0.0980	0.0074	100.0%
2	Al 2.0mm	0.002	1.416	0.3365	0.2223	0.0960	0.0072	96.5%
3	Al 3.0mm	0.003	2.102	0.3345	0.2203	0.0940	0.0069	93.1%
4	Al 5.0mm	0.005	3.434	0.3305	0.2163	0.0900	0.0064	86.5%
5	0.5Al-0.5PE-0.5Al	0.0015	0.834	0.3375	0.2233	0.0970	0.0073	98.2%
6	0.5Al-1.0PE-0.5AL	0.002	0.952	0.3365	0.2223	0.0960	0.0072	96.5%
7	1.0Al-1.0PE-1.0Al	0.003	1.643	0.3345	0.2203	0.0940	0.0069	93.1%
8	0.5Al-0.1Cu-0.8PE-0.1Cu-0.5Al	0.002	1.373	0.3365	0.2223	0.0960	0.0072	96.5%
9	1.0Al-0.1Cu-0.8PE-0.1Cu-1.0Al	0.003	2.060	0.3345	0.2203	0.0940	0.0069	93.1%
10	1.0Al-0.1Cu-2.8PE-0.1Cu-1.0Al	0.005	2.492	0.3305	0.2163	0.0900	0.0064	86.5%

Table 6.3: Mass and available volume for all eight thin boxes.

6.3 Realistic 6U CubeSat model

After the simplified geometry model a more representative model has been analysed. The CAD file used describes the standard 6U structure manufactured by ISIS (Innovative Solutions in Space). Figure 6.4 shows this model. The 298 parts included in this model range from outer panels of two by three decimetres to screws of under one centimetre in size. By loading the ISIS model into Fastrad and subjecting it to the radiation environment of a 1-in-100 years solar particle event, the worst-case scenario is tested and the received radiation dose at each of these 298 parts follows. This has been done by using the Forward Monte Carlo (FMC) simulation facility of Fastrad. Hereby, each part can be inspected individually.

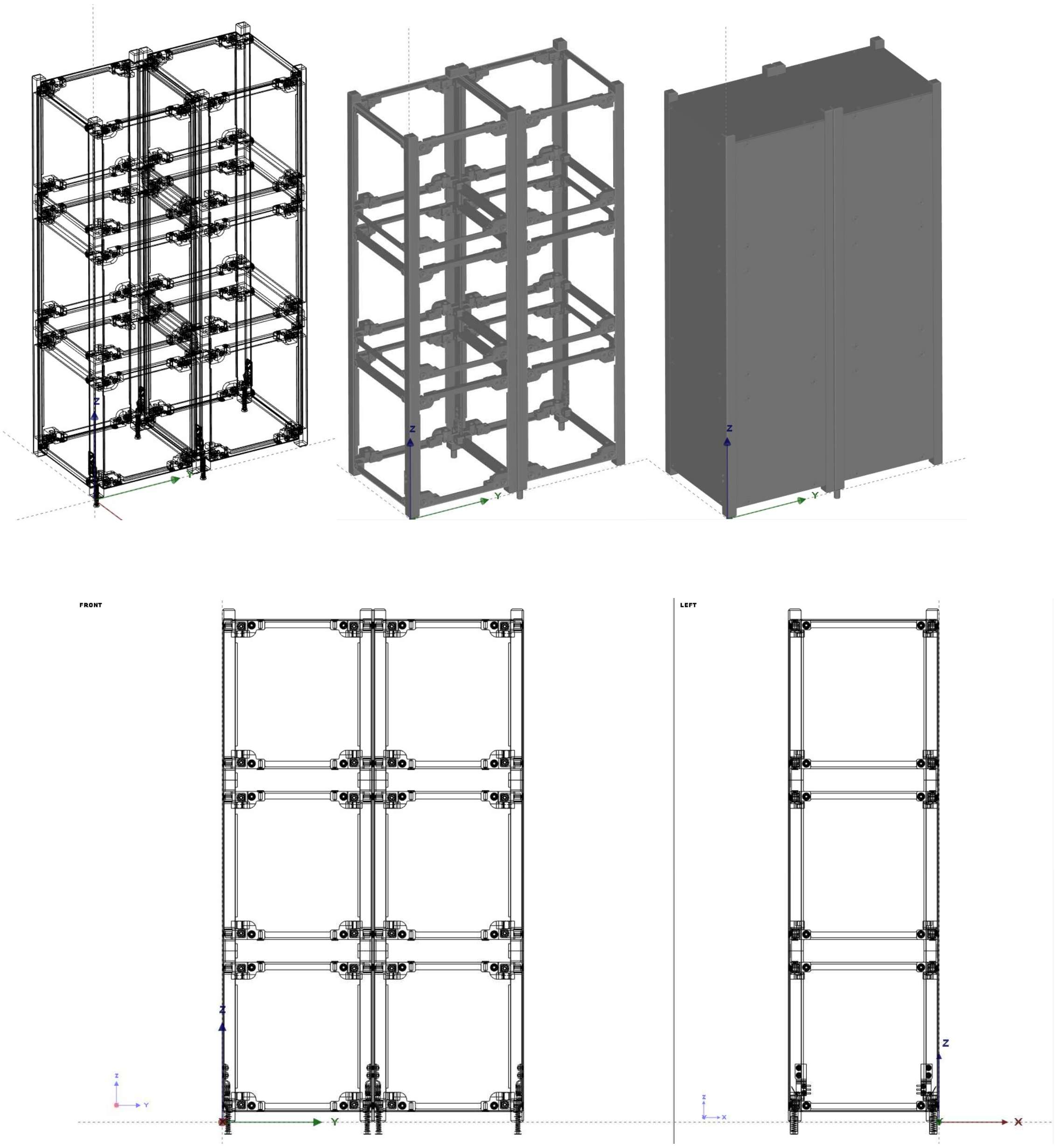

Figure 6.4a-e: Overview of the 6U CubeSat model analysed in this thesis. Wireframe (a), Structural without outer panels(b), full model (c), technical front-view (d) and side-view (e).

7. Results

This section shall discuss the most critical results for the materials and payload configurations chosen in the simplified models definition from section 4.2 as well as the simulation results of the 6U CubeSat model presented in section 4.3. To focus more on the analysis with respect to choice of material and payload configuration, one scenario has been selected from the several scenarios available. From the results the conclusion is drawn that the radiation shielding capacity shows similar behaviour for all SPENVIS outputs. The chosen scenario is the most critical one, namely the 1-in-100 years solar particle event scenario. This radiation environment tests the CubeSat model for a worst case solar radiation event that only occurs once every one hundred years. The proton flux for this worst-case scenario is found in Appendix B and the dose depth curve in Appendix C in case one wants to refer to those.

7.1 Results of Sector Shielding Analysis of Simplified Models

The first step in the radiation analysis is to perform a Sector Shielding Analysis, which in this work has been performed. For the analysis of the simplified 6U box models, a matrix of 3x3x3 detectors has been placed in each octant of the box. A 28th detector is placed on the outside of the model to use as a reference. Doing so, one can see the influence of material choice and material thickness on the radiation received inside the box with respect to the outside environment. This gives a first insight in the material selection to optimize the shielding. Figures 7.1 and 7.2 show the result of the sector shielding analysis on a simplified Aluminium 6U satellite shape. In Figure 7.1, the result is shown for the detector in the centre of the model. In figure 7.2, the result is shown for the detector that is located on the outside of the model. The difference in colours is larger in figure 7.1 (the centre detector) since it receives rays coming in through different sides of the material and hence travelling through a range of thicknesses of material. There is no difference in the colours in figure 7.2 (the outside detector) as it only receives radiation that has not travelled through the material yet. This means that the colour red signifies the radiation dose to which the unshielded environment is subjected. The shape in figure 7.2 is like a hemisphere because the detector on the outside of the model 'sees' a hemisphere of non-material on one side and material on the other side. In other words: half of the incoming rays is blocked by the model.

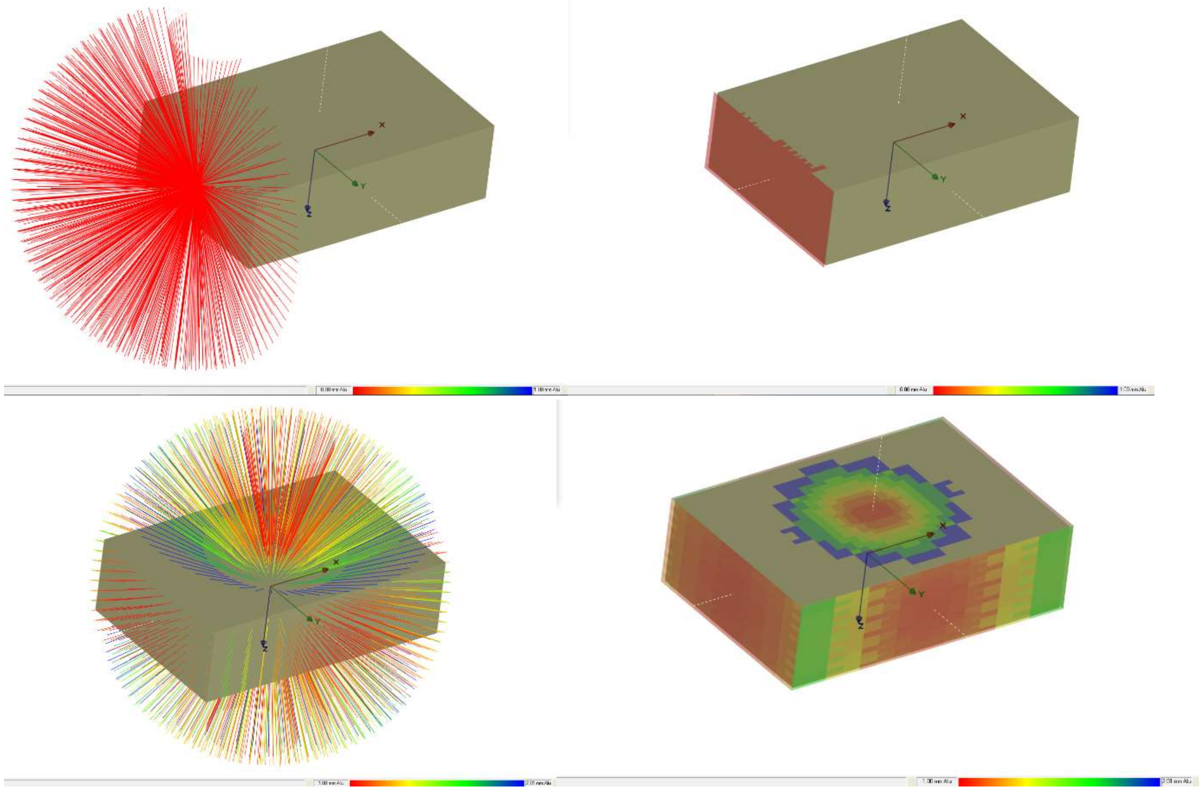

Figures 7.1a+b (top left and right): projection of incoming radiation onto a detector on the outside of the model. No scale in colour since all incoming radiation hits the detector without passing through material.
Figures 7.2a+b (bottom left and right): projection of incoming radiation onto a detector in the centre of the model. Clear differentiation in colours as some rays travel through less material (red) than other rays (blue) which have to penetrate through more millimetres of Al.

7.1.1 Material testing

In section 5.1, the resulting radiation load during a 1-in-100 years solar particle event are shown for the following locations within the satellite: Centre of the Bus, Inside of the three side-panels, Inside of one of the eight corners and the point in the centre of one octant of the satellite. Important to realize here, is the highly symmetrical shape of the CubeSat model, leading to eight identical octants. The chosen points in the previous list are thus valid for other points around the satellite as well. E.g. the measurement at the inside of the positive x- side-panel is valid for the negative x-side as well.

7.1.1.1 Aluminium Models

Four aluminium models were identified, with thicknesses of 1, 2, 3 and 5 mm respectively. Table 6.1 shows these results again. Clearly visible is the sharp decrease in received radiation load when increasing the thickness. This decrease is listed below in Table 6.1. In this Table, the received radiation load at the centre of each model is given as a percentage of the dose for the 1mm model. Also, the received dose as a percentage of the radiation dose outside the CubeSat bus is given. This outside radiation dose is 9.004E+04 [rad].

	Aluminium Thickness	Dose at Centre	Relative to 1mm	Relative to Outside Dose
1.	1mm	5.958E+03 rad	100 %	6.62 %
2.	2mm	2.552E+03 rad	42.8 %	2.85 %
3.	3mm	1.483E+03 rad	24.9 %	1.66 %
4.	5mm	6.993E+02 rad	11.7 %	0.78 %

Table 7.1: Radiation Dose at the centre of the CubeSat bus for all simplified aluminium models with thicknesses 1; 2; 3; and 5 mm. The received dose relative to the 1mm model has been given as well as the relative dose received at the centre of the model compared to the outside of the model.

Another conclusion that can be drawn from the radiation doses received inside the CubeSat is the high dose at the centre. Not only for aluminium this is true, but for all materials, the received radiation dose at the centre is higher than the radiation dose at the inside of the outer panels of the satellite. This result is not as strange as it might seem. The amount of rays that has to travel through a thicker layer of material is higher at the edges of the bus. Being so close to the material, means that only the rays that come in perpendicular to the material reach the detector. For a detector at the centre of the box, this is different. A small change of the angle at which the ray is coming into the CubeSat, will not lead to a large increase in material it has to cross and thus more rays reach the centre of the bus than a detector at the edge. This seems counterintuitive but this is a result that has become clear with the results in Figure 7.3. This leads to the conclusion that the radiation dose is lowest at the inside of two panels meeting. In section 5.2, this is further discussed by using the Forward Monte Carlo Simulation tool to investigate local differences in received radiation dose.

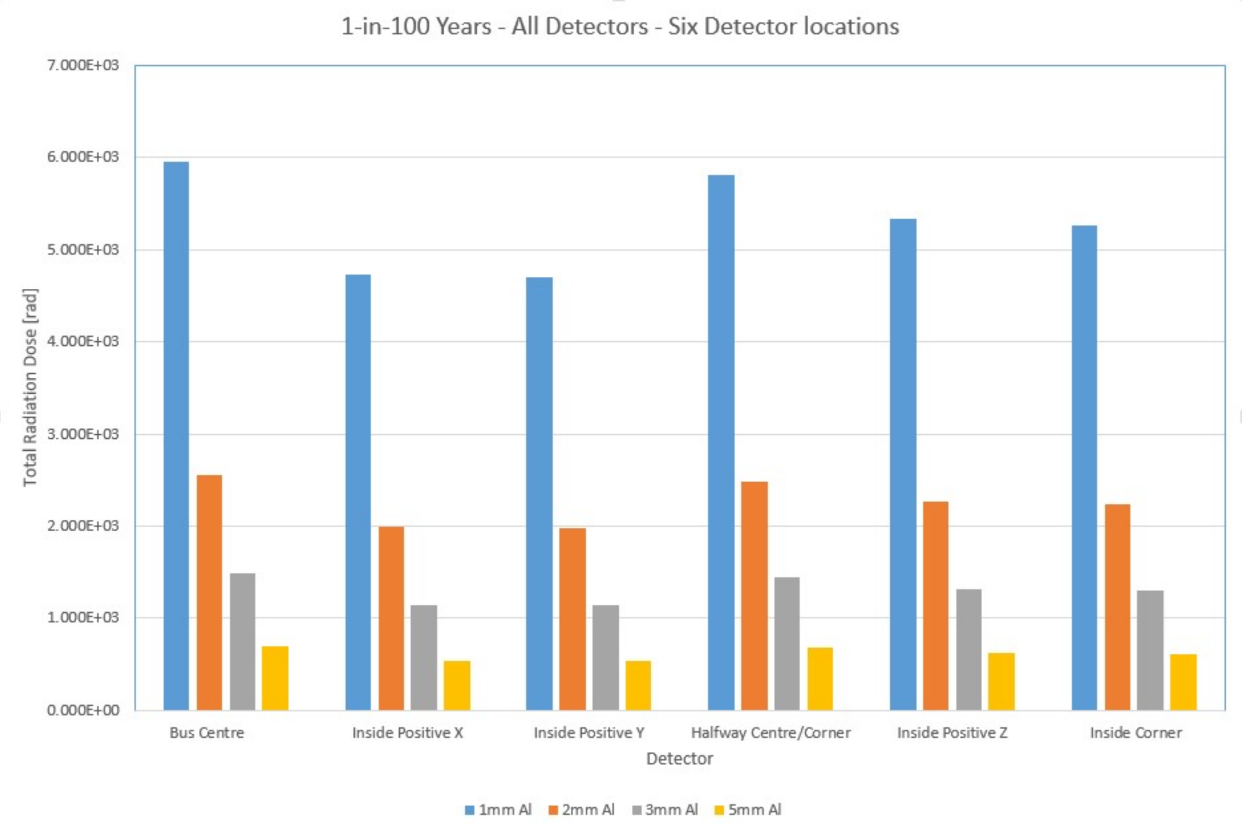

Figure 7.3: Radiation dose at six locations inside the CubeSat bus structure. Note the maximum value at the bus centre.

The relation between thickness of material and received radiation dose is very clear. One millimetre of aluminium already shields over 96% of the incoming radiation load. Thickening the material to five millimetres even decreases this fraction to 6% of the one millimetre dose. For CubeSat missions, an optimum has to be found between radiation shielding capacity and mass. Maybe one can live with a 15% dosage at 3mm thickness, if one does not want to increase the mass of the satellite. This probably is the reason for current state-of-the-art CubeSats to have aluminium thicknesses of 2-3 millimetre.

7.1.1.2 Aluminium and Polyethylene layered structures

The light and hydrogen rich material of polyethylene was chosen as an addition to the full aluminium structure to test its radiation shielding capacities. Figure 7.4 shows the results for the three chosen aluminium polyethylene structures from section 4.2.2. The slimmest model consists of two layers of 0.5 mm of Aluminium with an added 0.5mm layer of polyethylene in the middle. The second model has an equal amount of aluminium but a polyethylene layer of 1.0 mm and the thickest model has three times 1.0 mm thickness (aluminium-polyethylene-aluminium).

The relative shielding is again tabled and can be seen in Table 52. The percentages clearly show that although polyethylene has a low density, it can be used as a shielding material. The decrease in received radiation is stronger for aluminium, as can be seen by judging the difference between models two and three, knowing that the difference is millimetre of aluminium.

Compared to the first model, the second model listed in Table 5.2 has a 20.3% increase in shielding protection with only 0.5 mm of lightweight polyethylene added to the model. The third model is basically is double the layers of the first model, but has only 30.8 percent of the radiation penetrating to the centre of the bus and it can thus be considered a better potential structure, although the mass is twice as high.

Model layers	Dose at Centre	Relative to first	Relative to Outside Dose
0.5mmAl-0.5mmPE-0.5mmAl	4.981E+03 rad	100 %	5.54 %
0.5mmAl-1.0mmPE-0.5mmAl	4.211E+03 rad	84.6 %	4.69 %
1.0mmAl-1.0mmPE-1.0mmAl	2.070E+03 rad	41.7 %	2.31 %

Table 7.2: Radiation dose on models with Aluminium and Polyethylene.

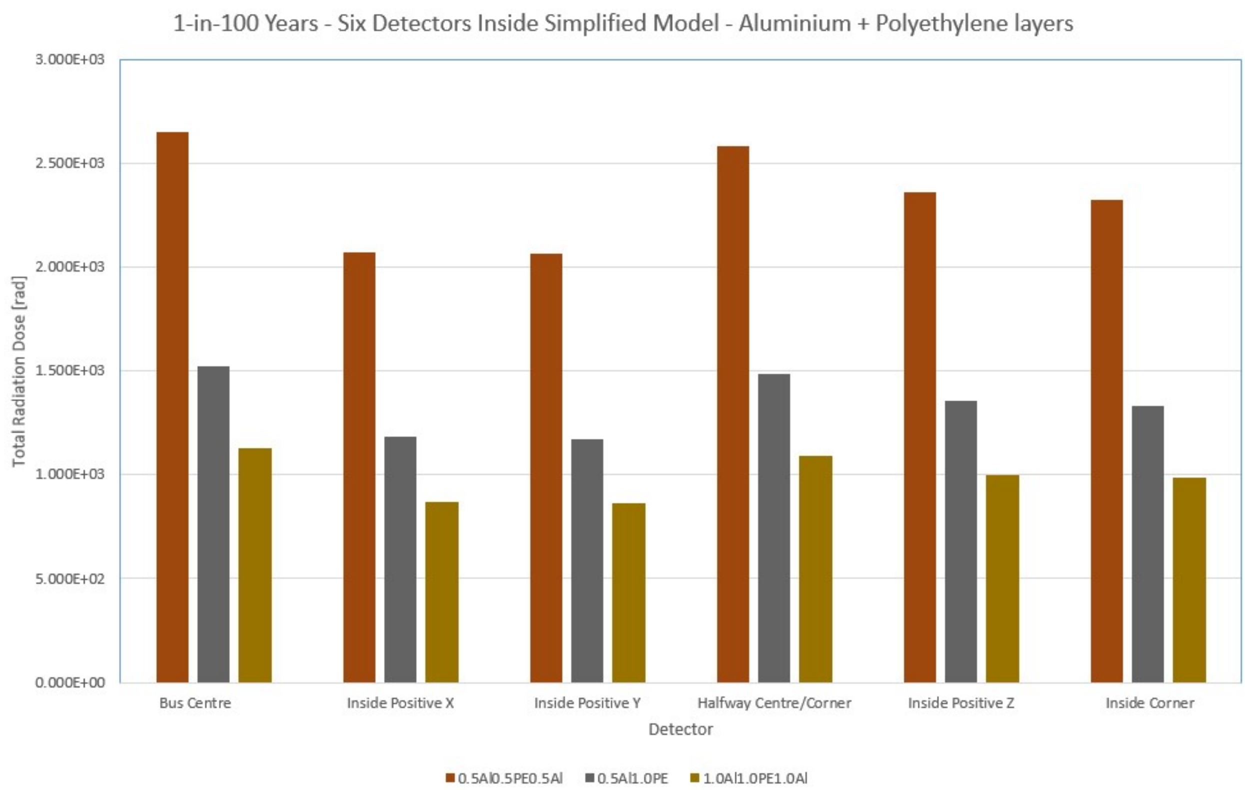

Figure 7.4: Radiation dose at six locations in the CubeSat bus structure for the aluminium plus polyethylene models. Thicknesses ranging from 1.5mm to 3mm.

7.1.1.3 Aluminium, Polyethylene and Copper layered structures

The last category is the sandwich structure of aluminium combined with polyethylene and a thin layer of copper. Copper is introduced to provide the bus structure with extra hardness against heavier ions entering the CubeSat environment.

The results are again tabled in Table 6.3. The result of adding 0.2mm of Cu and 0.8mm of polyethylene (PE) to the 1mm of aluminium already present in state-of-the-art materials, increases its radiation shielding capacity by over 51%. Adding another 2mm of polyethylene reduces the radiation load on the bus structure to one third of the original value.

Model layers	Dose at Centre	Relative to first	Relative to Outside Dose
0.5mmAl-0.1mmCu-0.8mmPE-0.1mmCu-0.5mmAl	2.654E+03 rad	100 %	2.96 %
1.0mmAl-0.1mmCu-0.8mmPE-0.1mmCu-1.0mmAl	1.525E+03 rad	57.55 %	1.71 %
1.0mmAl-0.1mmCu-2.8mmPE-0.1mmCu-1.0mmAl	1.126E+03 rad	42.5%	1.26 %

Table 7.3: Radiation dose on models with Aluminium, Polyethylene and Copper

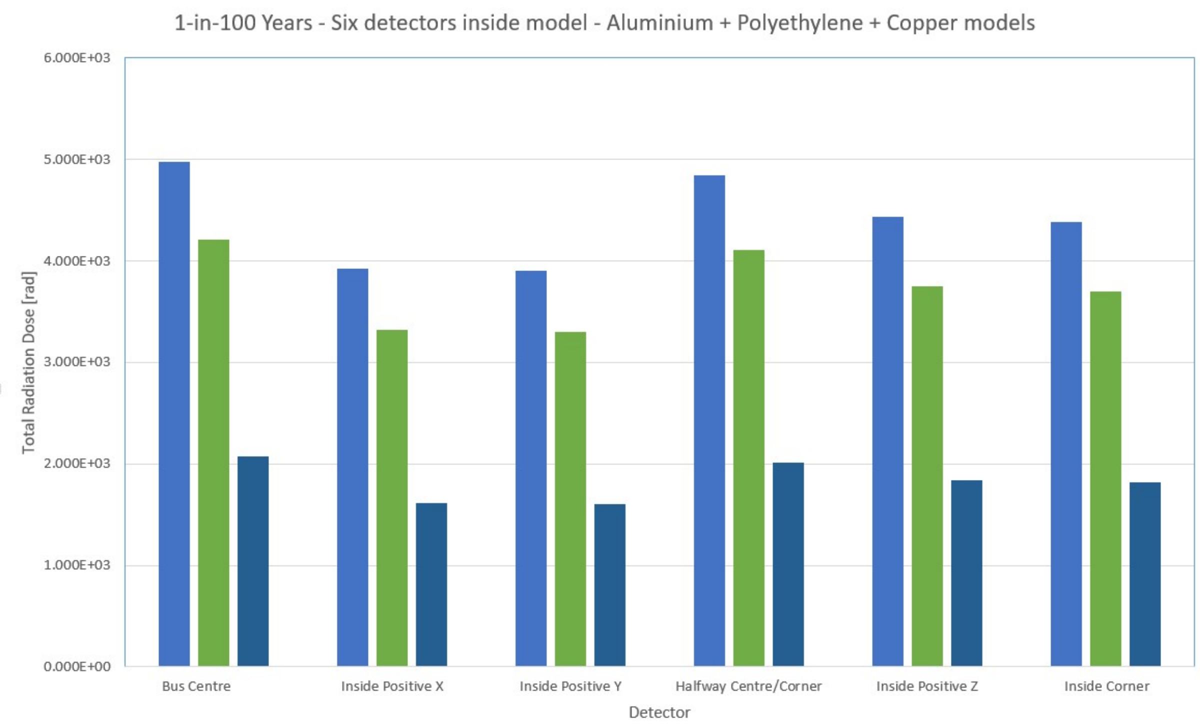

Figure 7.5: Radiation dose at six locations in the CubeSat bus structure for the aluminium plus polyethylene plus aluminium models. Thicknesses ranging from 2mm to 5mm.

7.1.1.4 Overview of Received Dose per Material Choice

As a final but highly important note to the section on material choice analysis, all ten models are compared. The results for one detector have been listed in Figure 7.6 and Table 6.4. Also, the mass of the model is added to provide a clearer overview of the shielding capacity per kg of bus structure. Clearly, heavier/thicker boxes perform better than thinner structures. One results that clearly stands out is the very good characteristics of model 9 (1.0mmAl-0.1mmCu-0.8mmPE-0.1mmCu-1.0mmAl) compared to a 3mm aluminium bus structure. A 3mm aluminium bus structure is a conventional COTS choice for CubeSat bus design. However, this new result for a combination of copper, polyethylene and aluminium shows similar shielding protection against solar radiation. The radiation received is 0.634% instead of 0.612%, so slightly higher. But the model mass is only 2.060 kg instead of 2.102 kg for full aluminium use. The shielding capacities of model 9 against GCR have to be checked, but are thought to be better than that of a pure aluminium bus structure, because of the inclusion of copper, a heavy metal that has the capability to shield heavier ions than aluminium.

Model Layers	Dose at Centre	% of total	Model Mass
1mm	5.985E+03 rad	6.62 %	0.715 kg
2mm	2.552E+03 rad	2.85 %	1.416 kg
3mm	1.483E+03 rad	1.66 %	2.102 kg
5mm	6.993E+02 rad	0.78 %	3.434 kg
0.5mmAl-0.5mmPE-0.5mmAl	4.981E+03 rad	5.54 %	0.834 kg
0.5mmAl-1.0mmPE-0.5mmAl	4.211E+03 rad	4.69 %	0.952 kg
1.0mmAl-1.0mmPE-1.0mmAl	2.070E+03 rad	2.31 %	1.643 kg
0.5mmAl-0.1mmCu-0.8mmPE-0.1mmCu-0.5mmAl	2.654E+03 rad	2.96 %	1.373 kg
1.0mmAl-0.1mmCu-0.8mmPE-0.1mmCu-1.0mmAl	1.525E+03 rad	1.71 %	2.060 kg
1.0mmAl-0.1mmCu-2.8mmPE-0.1mmCu-1.0mmAl	1.126E+03 rad	1.26 %	2.492 kg

Table 7.4: Received radiation dose at the bus centre detector and mass per model.

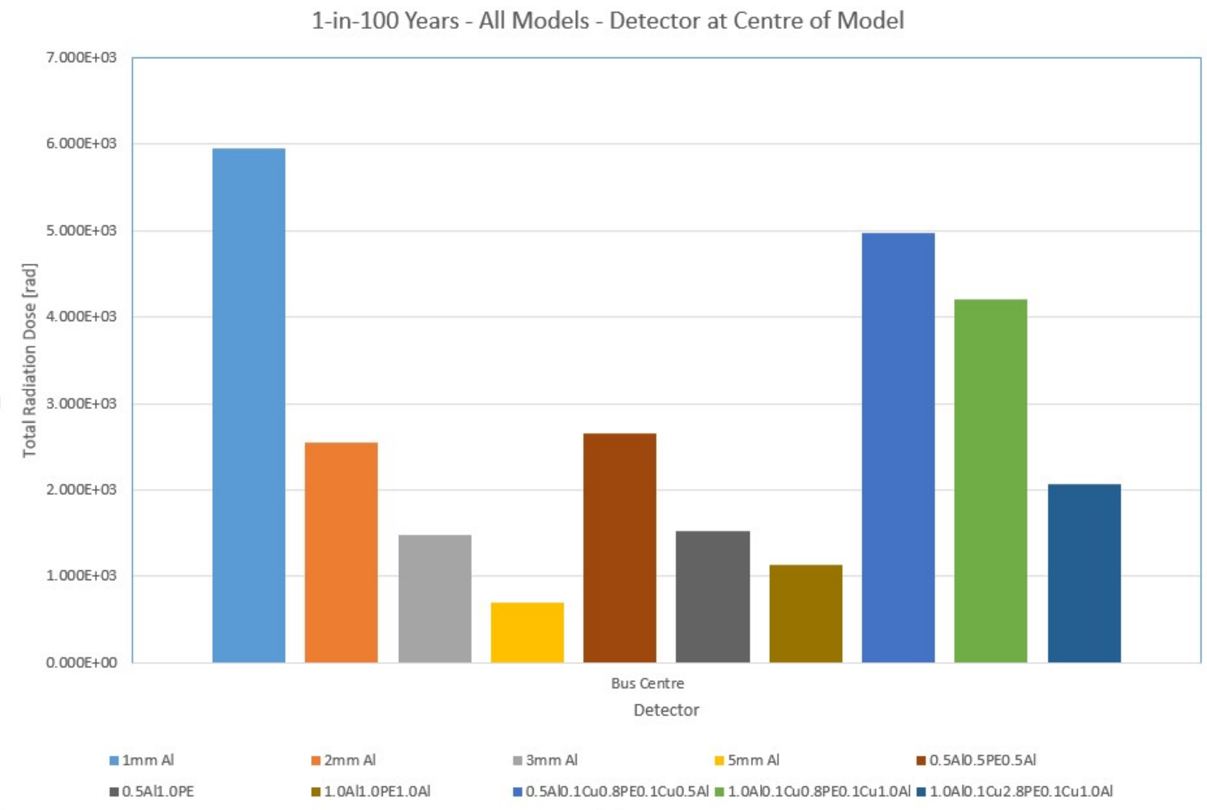

Figure 7.6: Radiation dose received at the models' centre detector for all ten simplified material models. Look at the similar shielding capacity of the third and ninth models.

7.2 Results of Sector Shielding Analysis of 6U CubeSat model

The 6U model which was presented in section 6.3, has been equipped with a dense grid of detectors. With a spacing of 5mm, each cubic centimetre of the model has 27 detectors in it (3x3x3). This leads to 65268 detectors in total. The choice for this dense grid has been made to have a proper overview of the sector shielding at almost each location in the sophisticated model. This way, the influence of all 298 parts of the model can be investigated. Like in the beginning of section 7.1, two explaining figures are included. Figure 7.8 shows the result of the sector shielding analysis of a detector on the outside of the model. Again, limited variation in the received radiation per angle (no shift in colour for changing direction). This is again due to the fact that the detector is open to space for only one hemisphere and on the other side, there is the model which serves as a shield. Figure 7.9 shows one of the best shielded – receiving the lowest radiation dose – detectors of the model. It is closely located to the centre side-frames, is close to the 2x3U outer panel and benefits from the slight extra shielding of the ribs on the side of the model. For this model there is a high variation in the colours, telling us that the radiation from some directions is better than from other directions. Figure 7.9b shows the interesting places for extra shielding (red sections) in case one wants to shield electronics or payloads located at the location of this specific detector. Full dose- and sector-file are provided in Appendices D and E respectively.

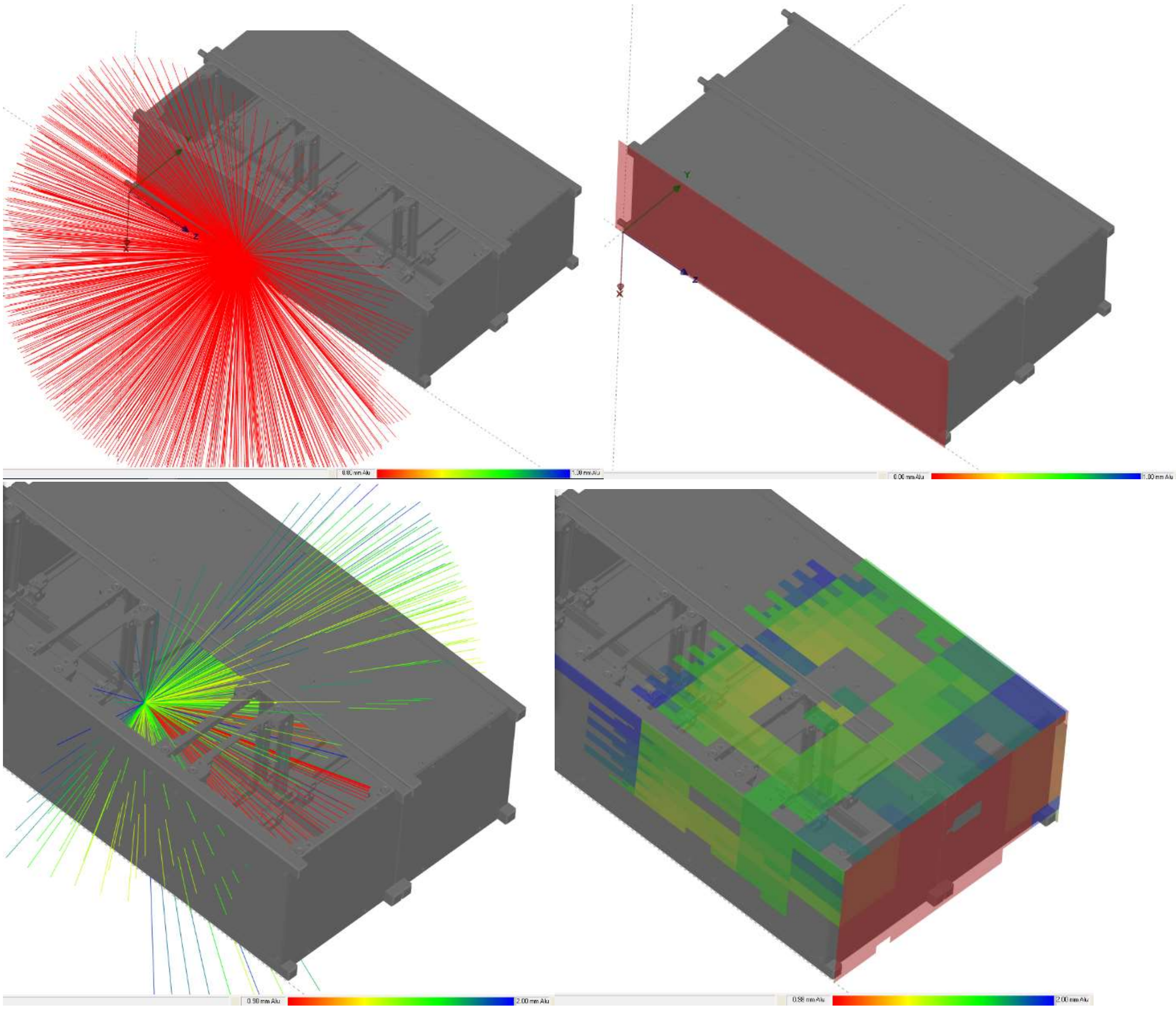

Figures 7.8 and 7.9(bottom): showing the results for two detectors in the sector shielding analysis.

7.3 Results of Monte Carlo Simulation of Simplified Models

The results of the Forward Monte Carlo simulation of the simplified models are limited. The FMC simulation is more useful when specific sensitive zones are to be investigated instead of detector locations. That is why a simple structure is better inspected using the sector shield analysis published in section 5.1. Another factor for the discard of FMC simulation for the simple models, is the fact that the models that consist only of aluminium are defined by a single box. This means that only one sensitive zone can be identified and thus only one value for deposited dose in [rad] is obtained for these simplified models. Nevertheless, the results are published below in table 7.6 to get an overview of the values for deposited dose in [rad] obtained from these FMC simulations. It is clear that similar deposited doses are experienced. This is due to the similar size of the boxes, leading to identical sensitive zones used in the simulations.

Table 7.6: Results of Forward Monte Carlo Simulation for Simplified Aluminium Models

Model Material	Deposited Energy [MeV/h]	Deposited Dose [rad/s]
1mm Aluminium	N/A	N/A
2mm Aluminium	2.290601E+9	2.592307E-2
3mm Aluminium	N/A	N/A

One fact that was referred to before in section 5.1, is the influence of the vicinity of the sides of the box structure on the deposited energy at a specific location. In the centre, one experiences a higher deposited dose than closer to the edges. This can be made visible by increasing the amount of voxels of the sensitive zone. In figure 7.10 a side-view of the 2mm Aluminium model is shown. On this 2x3U side of the model, a clear difference can be spotted in the deposited energy at several locations of this side-panel. Being close to the sides is beneficial for shielding, as one can see from the lighter red and even orange and yellow colours in figure 7.10. As one can read from the scale on the right, this leads to a decrease of deposited energy of a couple of orders of magnitude and this is something to keep in mind when placing specifically vulnerable electronics or payloads.

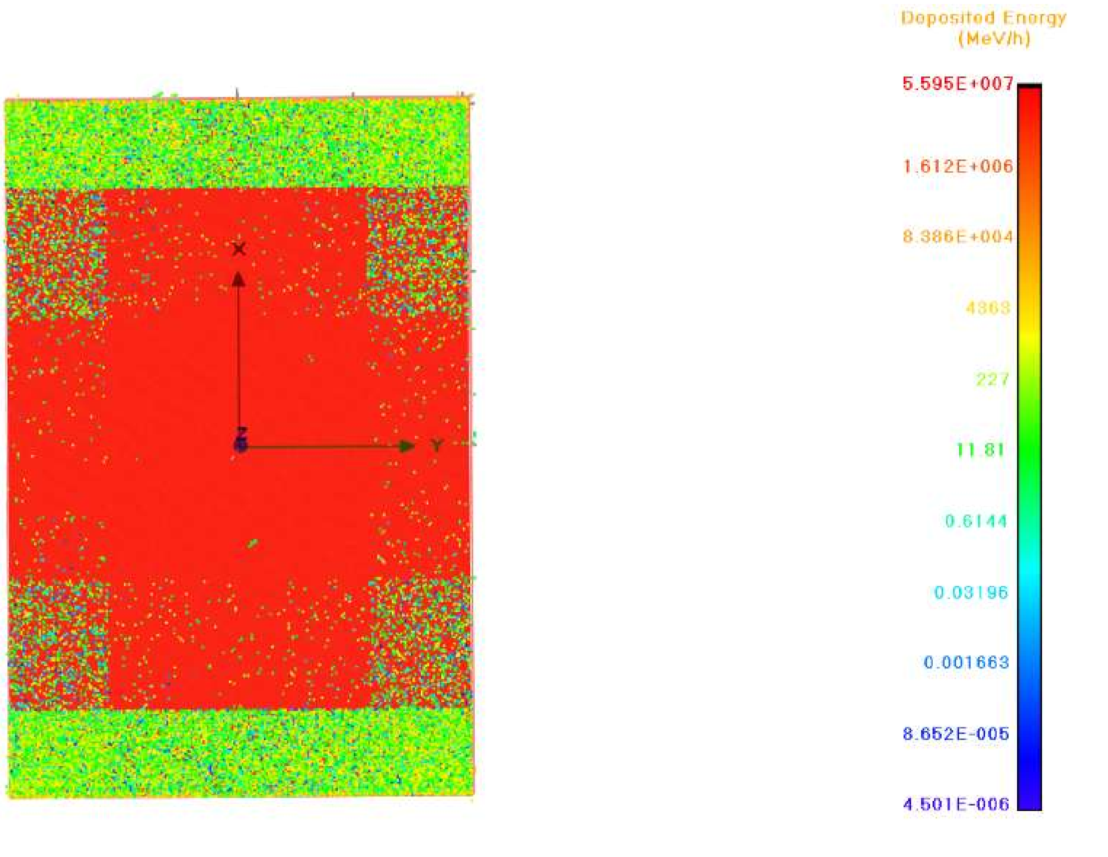

Figure 7.10: Side view of the Forward Monte Carlo simulation result of a 2mm Aluminium simplified 6U structure. The difference in deposited energy per location are visible and differ by a couple of order of magnitude. Scale going from 5.6E7 MeV (red) to 4.5E-6 MeV (blue)

7.4 Results of Monte Carlo Simulation of ISIS 6U CubeSat

The radiation environment as discussed in section 5.3.4 has been modelled in Fastrad to obtain a deposited energy overview for each part of the cad-model of the 6U CubeSat. The results of this Monte-Carlo simulation is presented in this chapter. Defining three levels in the amount of radiation received, one can more specifically see which parts receive high doses of radiation (outsides of the model) and which parts receive less radiation (inside of the model). This division has been made to look into more detail to the radiation deposition of the solar radiation received by the CubeSat. This division is further clarified in the first part of this results chapter. Once this division of structural levels is dealt with, first the best shielded sections are shown. After that, the structures shown are continuing outward to the higher and highest radiation dose receiving parts of the CubeSat model. Both the structural parts involved and the outcome of the Monte Carlo simulation are presented in each section.

Structural Division into Three Levels

By defining three structural levels of the CubeSat model, one can look at the results in more detail. Another benefit is the more specific colour scale that results from the Forward Monte Carlo simulation in Fastrad. This will become clear once these results are shown in the coming sections. First, this section shall define the three structural levels (from inside to outside) of the CubeSat. Three levels are defined:

1. Inside structure
2. Side-frames
3. Outside structure

As expected, the radiation dose received by the three levels increases when going towards the outside of the model. The 10^7 particles Forward Monte Carlo simulation results for the standard aluminium 6U CubeSat model of ISIS Space are shown in Table 7.7. In this table, the ranges of received radiation doses at the three levels is given. From this, it is clear that a significant decrease of received radiation dose is observed for the inside structure compared to the outside structure.

Received Radiation Dose [rad] at three levels of the 6U CubeSat Structure			
Level	Name	Received Dose [rad/s]	Received Dose 4 day SPE [rad]
1.	Inside Structure	2.0E-3 to 9.4E-3	6.9E+02 to 3.2E+03
2.	Side-Frames	1.3E-2 to 3.5E-2	4.5E+03 to 1.2E+04
3.	Outside Structure	6.5E-2 to 7.7E-2	2.2E+04 to 2.7E+04

Table 7.7: Range of Received Radiation Dose per level as presented in sections 5.4.1 to 5.4.3.

7.4.1 Level 1: Inside structure

This section deals with those parts of the model that are least subject to proton penetration and thus have a lower radiation dose subjected to them. The amount of deposited radiation for these parts lies under 1.0E-2 [rad/s] or 3.5E+3 [rad] during a four day SPE. The parts involved are the ribs connecting the side-frames of the CubeSat and the screws attached to them. Due to the protection that these parts experience from the side-panels on the outside of the structure, the radiation levels are lowest in these parts. Figures 7.11a+b designate the parts involved, the radiation received by them and a detailed zoom of some of these ribs and screws.

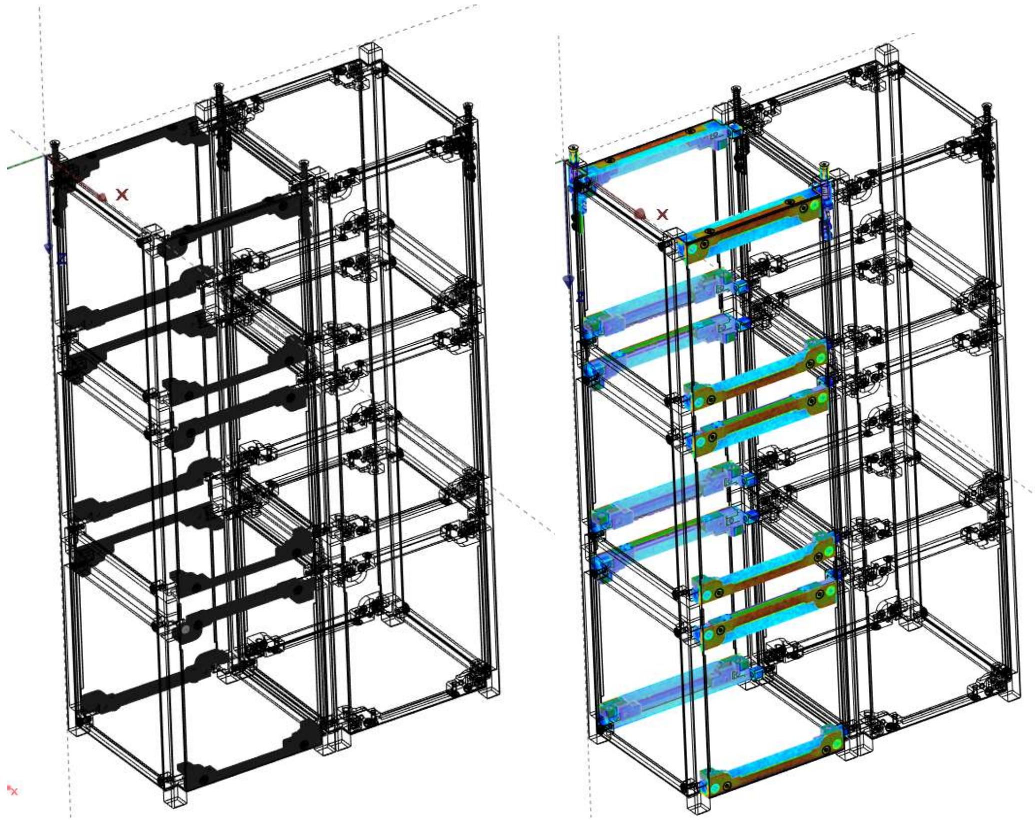

Figure 7.11a+b: Left: structural parts shown in wireframe structure. Right: forward Monte Carlo deposited dose on the parts concerned in this section.

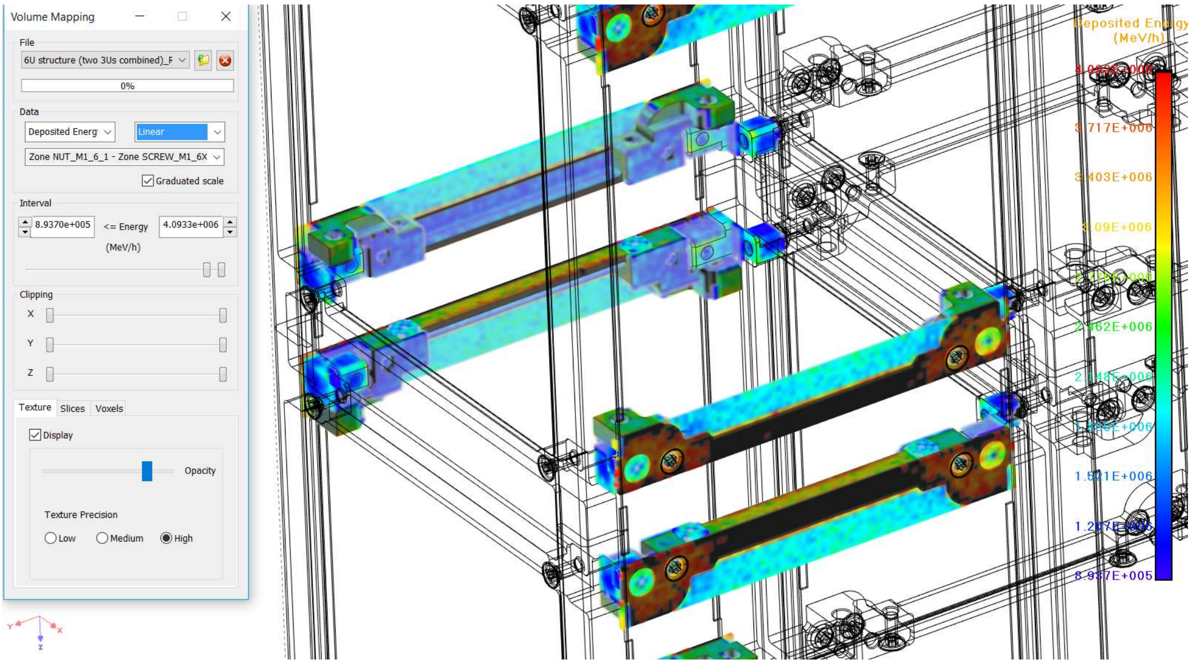

Figure 7.12: Zoom onto the inside structure that is analysed in this section. Clear distinction between the yellow screws and the red ribs. Also, the blue shielded area behind the rib is clearly visible.

There is a clear difference between the outer structure of the CubeSat and the parts designated in Figure 7.12. By presenting these parts separately, the individual distinction between ribs and the screws in these ribs can be made visible, see figure 7.12 In Figure 7.12 a better view is given of four of the ribs on the inside of the CubeSat structure and the radiation received locally. One can even distinguish a slightly higher received dose on the middle section of the rib, compared to the outsides. Also, the screws on the right side of the ribs in figure 7.12 are receiving a higher dose (yellow) than the screws on the left of the picture (blue). The deposited energy in the figures 7.11b and 7.12 ranges from 9E+5 [MeV/h] to 4E+6 [MeV/h]. This corresponds to a received radiation dose ranging from 2.01E-3 [rad/s] in one of the ribs' screws, to 9.43E-3 [rad/s] in one of the springs at the top side of the CubeSat. This is the equivalent of a total dose during a 4 day SPE of 6.94E+2 [rad] in the ribs' screws to 3.26E+3 [rad] in the springs at the top side of the CubeSat. These results show that even on the inside structures of the model, the received radiation dose can be a factor 4 to 5 larger on one part than on another. The specific radiation doses received for each part, are found in Appendix F. In Appendix F one finds a full list of the radiation doses received for all 298 parts of the full model.

7.4.2 Level 2: Side-frames

Going outwards one level, the side-frames are considered. In these parts, one observes that the received radiation levels have dropped due to shielding by the outer panels. However, the received radiation dose is higher than that at the ribs and thus a separate section has been devoted to these parts. Received radiation doses of 1.32-3.54E-2 [rad/s] or 4.56-12.2E+3 [rad] during a four day SPE follow after simulation.

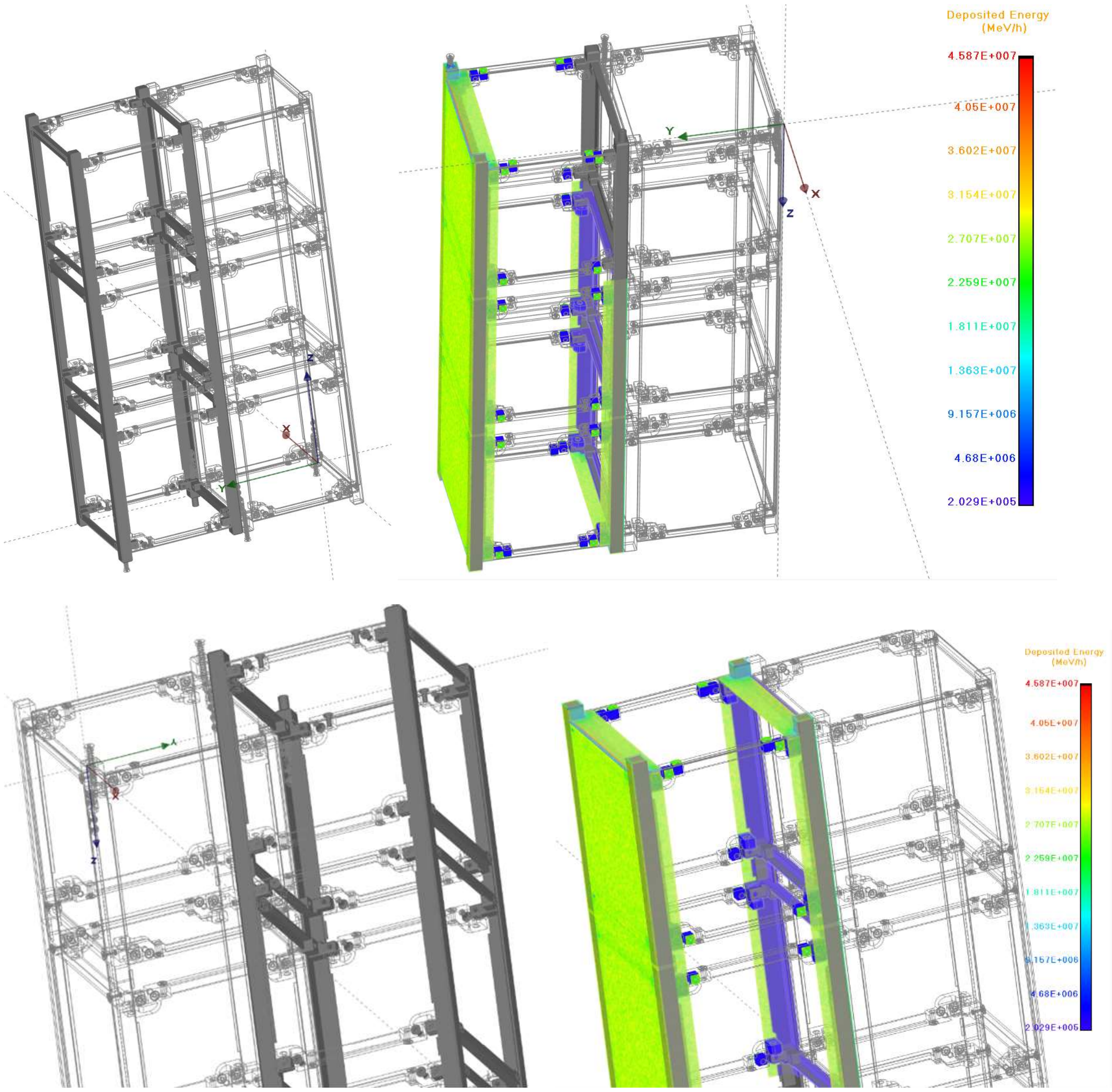

Figures 7.13a-d: Left: structural parts shown in wireframe structure. Right: forward Monte Carlo deposited dose on the parts concerned in this section, level 2.

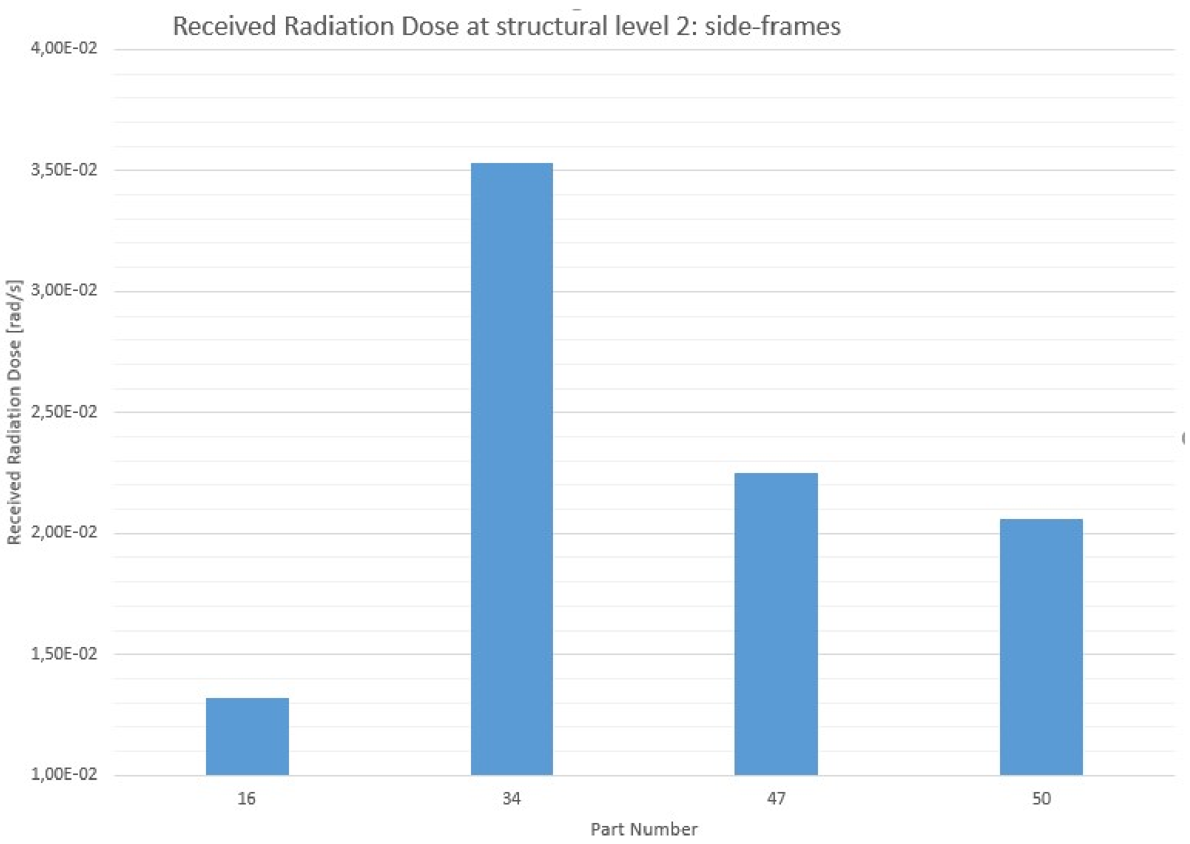

Figure 7.14: Graphical representation of the dose received at four of the level 2 parts. Parts concerned: 1U interior side-frame (16), one of the screws in the exterior side-frame (34), 1U exterior side-frame (47), screws to the interior side-frame (50).

7.4.3 Level 3: Outer panels

Moving towards the outer layer of the CubeSat structure, the highest received radiation doses are experienced – as expected. The structural parts involved in this section are identified in figure 7.14. These are the parts that have no other structure between them and the outside of the CubeSat, resulting in full exposure to the radiation environment as defined in Section 5.3.4. This also leads to a similar radiation environment for all outer panels of the structure, as the radiation environment is uniformly applied. This can be seen in figure 7.14d where the yellow coloured panels mean that the radiation received by the panels is of the same magnitude. The results for a 10^7 particles simulation vary from 7.55E-2 [rad/s] on the top square panels to 7.67E-2 [rad/s] on the rectangular side panels. This equals 2.61E+4 [rad] to 2.65E+4 [rad] during a four day SPE.

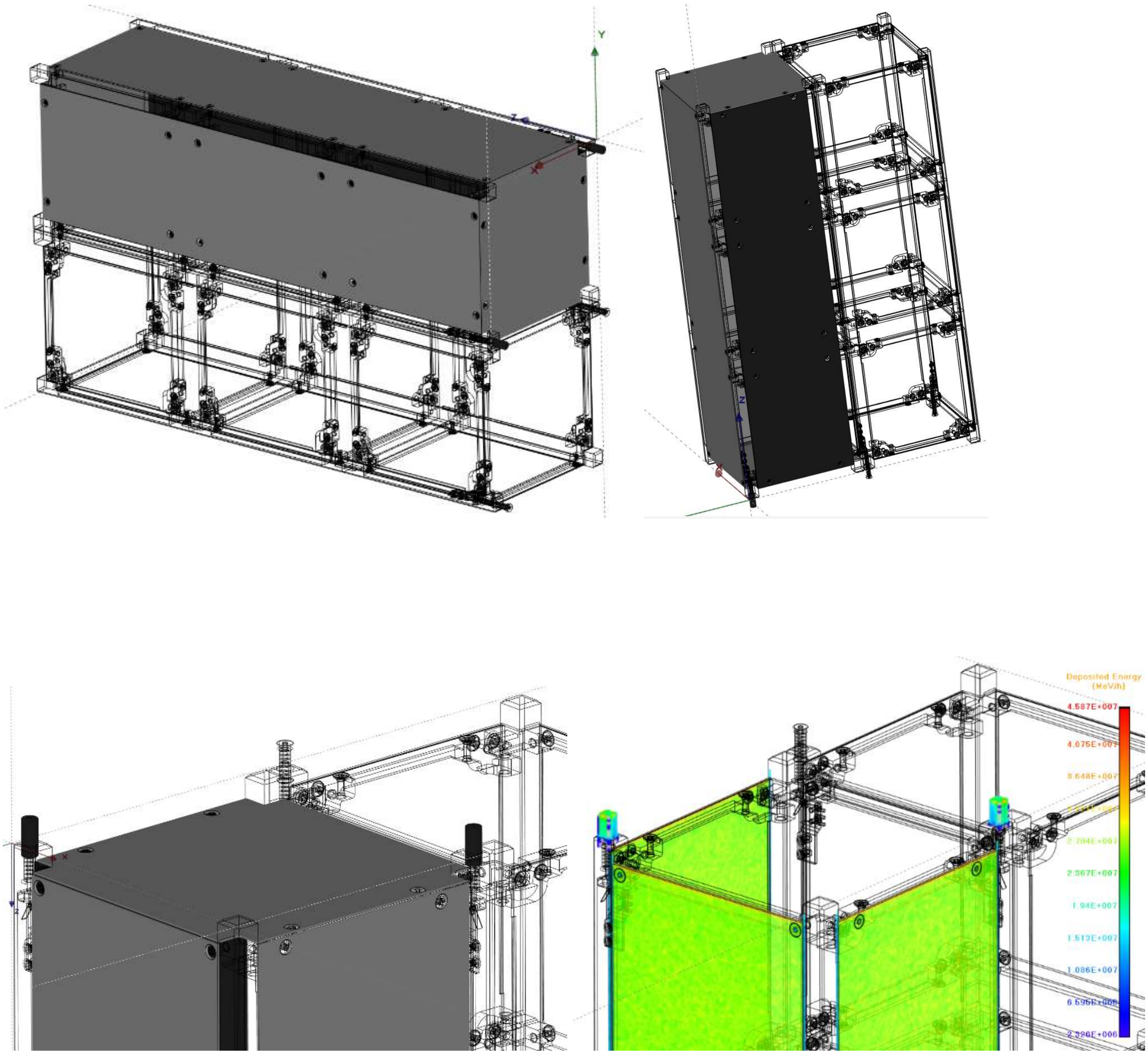

Figures 7.14a-d: Structural representation (a-c) of the parts concerned in this level 3 analysis, with a visualization of the FMC-simulation (d).

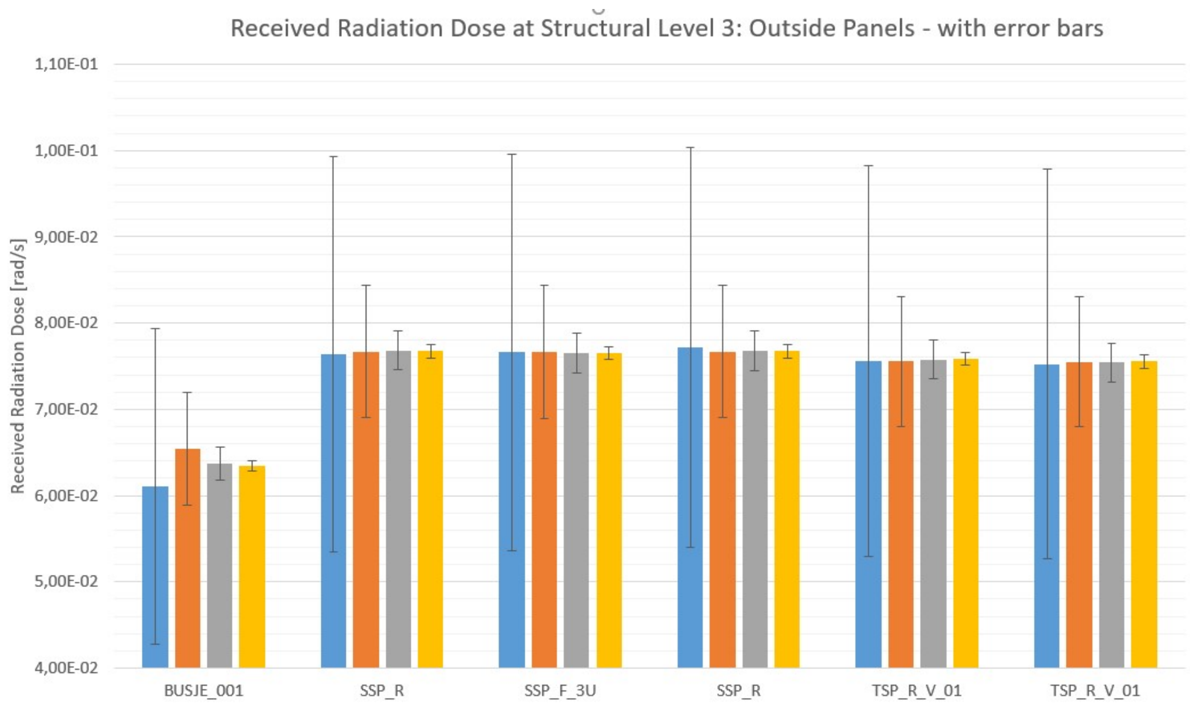

Figure 7.15: Received radiation dose in rad/s for the six parts on the outside of the model. For all six parts, the error margin due to choice for the number of particles in the simulation is given. The error diminishes by a factor of 3 for each order of magnitude.

8. Verification

The results as discussed in Chapter 7 are presented and the simulation methods of ray-tracing and forward Monte Carlo show similar results. This Chapter shall verify this statement by comparing the simulation methods and results. Also, a flashback to chapter 3 shall be made, where the radiation environment is created. It is checked with literature that the created 1-in-100 years solar particle event of SPENVIS is supported by literature. Also, the radiation doses flowing from the simulations results in Chapter 7, are compared to the dose limit of 20 krad for the electronics presented in section 3.5.

8.1 Ray-tracing – sector shielding analyses

The radiation dose files created by the ray-tracing method in Fastrad has created equal radiation doses on both the simplified and the state-of-the-art 6U CubeSat models. This can be seen by taking a look at results for similarly positioned detectors. E.g. the detectors on the outside of an outer panel of the model. The outside detector in the sector file for the 1mm Aluminium Simplified model (results in section 5.1.1.1) shows the same received radiation dose as Detector #19091in the sector file for the 6U state-of-the-art model (Appendix D). Both receive 50% of the incoming radiation without shielding of any material of the model as they are positioned next to an outside panel of the satellite. The respective values for the outside radiation dose of a detector receiving 50% of the incoming radiation are 9.004E+04 [rad] for the simplified model and 9.042E+04 [rad] for the state-of-the-art model. This shows both times, the method is applied with the same inputs and using the same method.

The simplified model of a 1mm Aluminium box shows a range of received radiation doses of 1.126-5.985 E+3 [rad] at the centres of the models and 9.004 E+4 [rad] on the outer skin of the models., whereas the state-of-the-art model shows a range of 5.098E+02 [rad] to 1.583E+05 [rad]. The range of the state-of-the-art model is higher, but this can be explained. The upper limit is defined by detectors on the outside corners of the model, where the model itself only shields one octant of the sphere of incoming rays, thus this particular detector receives about 7/8th of the incoming radiation without shielding. This again is easily proven by realizing that 9.042E+04 [rad] was 50% of the radiation, and indeed, this comparison stacks up. The thousands of detectors on the interior of the state-of-the-art model show a wider range of received radiation dose than the 27 detectors in the simplified models. The lower limit (5.098E+02 [rad]) of the state-of-the-art model's detected radiation dose is of a detector that is shielded by much material from all sides. Some of the rays reaching this well-shielded detector (#11508 in the dose file in Appendix D) are penetrating through centimetres of material (outer panels, ribs, screws etc.) before reaching the detector's location, which is checked by looking at the sector file in Appendix E. This can also be seen in Figure 8.1, where the location of this specific is marked with the ray-tracing method projected on it. One can see that the detector is reached by a limited number of rays because of the high shielding of surrounding material.

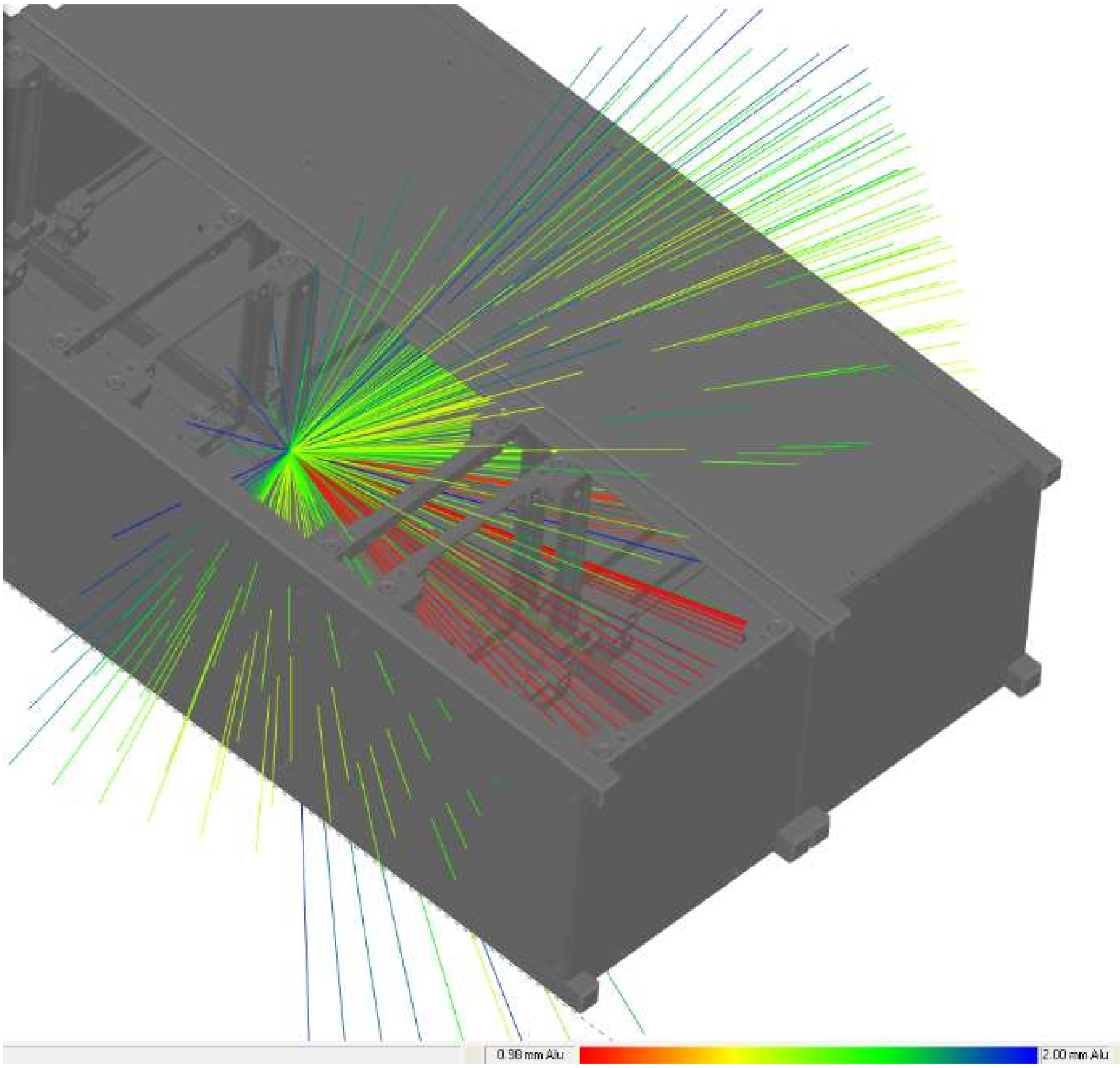

Figure 8.1: Ray-tracing at the location of detector 11508 from appendix D, where the lowest deposited radiation dose was measured, 5.098E+02 [rad]. Note the high amount of parts close to the detector location.

8.2 Forward Monte Carlo Simulation

The forward Monte Carlo simulation was performed with the differential proton flux (Appendix B) from SPENVIS. This proton flux showed similarity with the documentation from the Sapphire model (Figure 5.4, section 5.2) for 1-in-100 years events.

From Appendix F, where one finds the .dat-file containing the results for the forward Monte Carlo simulation of the 6U CubeSat model, and from Figure 7.14 in section 7.4.3 one sees that for the outside parts (numbers 17, 31, 48 and 62 t/m 65) the deposited dose equals values of 6.35E-2 to 7.67E-2 rad/s. This equals 2.2-2.7E+04 [rad] if this radiation dose is applied for the four days SPE scenario.

The simplified structures are also subjected to a forward Monte Carlo simulation, leading to a deposited dose of 2.592E-2 [rad/s] for the 2mm Aluminium structure, boiling down to a dose of 8.959E+03 [rad] during a four day SPE . This sadly was the only Monte Carlo result for the simplified boxes. But, it shows consistency with the results obtained in the ray-tracing simulation, where the maximum outside dose for the 2mm aluminium model was 8.957E+04 [rad] and the dose at the centre was 2.552E+03 [rad]. The FMC result finds its spot in between, and is literally in between the centre and the outside of the model, as in FMC-simulation the structure itself is the 'detector'.

8.3 Overview and Comparison of Two Simulation Methods

This section shows the results discussed in Chapter 7 and the start of this Chapter 8 in brief in table 8.1. It is important to notice the similarity in the result for the two simulation methods of ray-tracing and forward Monte Carlo. Also note the equal radiation dose for the outside skin of the simplified models and the 6U model in the middle column. Both simplified model and 6U state-of-the-art model receive an equal amount of rays at these locations during the ray-tracing simulation, explaining this similarity.

Model	Deposited dose during a 4 day SPE [rad] using Ray-tracing simulation	Deposited dose during a 4 day SPE [rad] using forward Monte Carlo Simulation
2mm Aluminium Simplified	2.552E+03 at centre of model 8.957E+04 at outside skin	8.959E+03
All Simplified Models	1.126-5.985E+03 at centre 8.935-9.004E+04 at outside	N/A
6U State-of-the-art	5.098E+02 deep inside model 9.042E+04 at outside skin 1.508E+05 at outside corner	0.69-3.2E+03 at inside 0.45-1.2E+04 in side frames 2.2-2.7E+04 at outside parts

Table 8.1: Brief results overview to show similarity in results of the simple and state-of-the-art models as well as the similarity in results for ray-tracing and forward Monte Carlo simulation

8.4 Check against Benchmark

With the summarized results restated in table 8.1 in the previous section, the benchmark for small satellite spacecraft set in section 3.5 comes into play again. The value 2.0E+4 [rad] had been found through research by Sinclair and Dyer to be applicable for electronics in small satellites such as CubeSats.

Looking back at the summarized results in section 8.3, one can see that some of these results surpass that number of 2.0E+04 [rad] by quite some margin. On the other hand, these are solely the parts that are situated on the outside of the model, also known as the skins and plates. Looking further into the results of the forward Monte Carlo simulation of the state-of-the-art model, one sees that all other parts receive doses of 6.9E+02 [rad] to 1.2E+04 [rad] during a four day Solar Particle Event.

The relatively high doses at the side-frames of the model (1.2E+04 rad) are still on the high side and one should thus critically look at placing the chosen electronics in a particular spot if one wants to make sure that a 1-in-100 years SPE does not lead to mission failure. The dose and sector files in appendices D to F can support the designer in further optimizing the spacecraft electronics placement such that the minimum amount of deposited dose is cast on the part.

9. Conclusions

The radiation environment of a 1-in-100 years solar event has been cast upon several satellite models. This section discusses the findings of the radiation shielding of these models. Simplified models have been tested through a ray-tracing simulation to investigate which materials might improve the radiation shielding of the satellite. Such a ray-tracing simulation provides an overview of the received radiation at each point in the model (where one has placed a detector). This ray-tracing method also gives an overview of the directions through which this detector receives the highest radiation dose. This makes this ray-tracing method worthwhile, since one would know which parts of the satellite are to be shielded better.

A more sophisticated model of a 6U CubeSat has been subjected to the same radiation environment, now using both a ray-tracing simulation and a forward Monte Carlo simulation. This Monte Carlo simulation provides an overview of the deposited dose in each of the 298 parts of the satellite model. Hereby, one can create clear coloured visualizations of the full satellite model and one can see which parts receive a high dose (red) and which receive a lower dose (blue) of radiation.

All these results are published in Chapter 7, and are summarized in brief in table 8.1 in the previous chapter. Now it is time to look back and recapitalize the most significant findings.

Materials that improve the standard aluminium model

Inclusion of polyethylene into the bus structure models has not led to the desired solution for a new CubeSat design. The lightweight material's shielding capabilities are found to be worse than pure aluminium models. However, the further combination with copper is shown to be beneficial. The combination of low-Z shielding of polyethylene, heavy ion shielding of copper and state-of-the-art material of aluminium in a 3mm thickness structure is found to be as effective for solar particle protection as a full aluminium model of the same thickness. Besides that, copper is also a good heavy ion (high-Z) shielding material when looking at galactic cosmic ray shielding. This extra benefit for this sandwich structure of aluminium polyethylene and copper leads to a recommendation to study this structure in further detail as it shows its potential for inclusion in future interplanetary CubeSat missions as its lighter and equally radiation protective as a bus structure.

Not only the material configuration of the outside bus structure has been studied, but local radiation levels inside the bus structure have been studied as well. Adding models to all of the six unit cells of the 6U CubeSat structure has given insight in the radiation load inside the bus structure. It has been found that there is no difference in several 1U payload units and e.g. one 2U payload when it comes to inside radiation loads. In general, the radiation levels in the central section of the CubeSat is found to be lower than on either end of the CubeSat. However, when placing payloads or extra protective material at either end of the CubeSat, this has a better shielding effect than placing this material on the central zone (two central unit cells) of the CubeSat.

Finalizing this materials study; it has been shown that a combination of aluminium, polyethylene and copper provides a better shielding CubeSat bus structure than the state-of-the-art material of pure aluminium. In the future, it shall thus have to be studied in more detail.

Location dependency within a 6U CubeSat structure

The results of the forward Monte Carlo method in section 5.4 have shown that the parts of a CubeSat structure can be sorted into three groups or 'levels' of radiation dose that is deposited on them. The outside level constitutes of the parts that are directly hit since they are on the outside of the structure; and these receive 6E-2 to 8E-2 rad/s in a 1-in-100 years solar event. Going one level towards the inner structure, one sees parts that receive 1.5E-2 to 3.5E-2 rad/s. The inner structure receives a dose of 2E-3 to 9E-3 rad/s during such a solar event. These values are 6.9E+02 to 3.2E+03 [rad], 4.5E+03 to 1.2E+04 [rad] and 2.2 to 2.7 E+04 [rad] during a 4 day SPE. This is visible in great detail thanks to this Monte Carlo visualization.

The outer structure (mostly the outside panels) thus receives by far the highest dose. When changing the material of the outer panels of the structure or increasing the thickness of these panels, one sees a sharp decrease in radiation deposition on the interior parts. The materials tested in the section with simplified CubeSats have also been incorporated in the sophisticated 6U CubeSat model. These results show a similar shielding behaviour in this sophisticated model as in the simplified models. However, attention has to be paid to anomalies in the results for the updated sophisticated model, since the structure is highly complex (298 parts). The influence of the specific parts on the radiation dose deposition has to be studied further.

The benchmark set in section 3.5 has been partially passed. The outside structure or skin of the CubeSat receives doses that are higher than the 20 [krad] benchmark. However, the benchmark is passed for the largest part of the inside structure of the model during a four day SPE. This means that in further research, the optimum location and connections with subsystems can be investigated to further optimize the design of a 6U CubeSat structure in interplanetary flight.

Sector Shielding Analysis for future improvement

The sector files created in this thesis, especially the sector shielding analysis of the 6U state-of-the-art model, are of interesting use for further research into improvement of a CubeSat structure. The dense grid of detectors in the model has provided an extensive amount on information about the direction from which each point in a 6U CubeSat structure is receiving its radiation dose in case of a 1-in-100 years solar event. This thesis has analysed these vulnerable spots through which radiation penetrates through the model's material and has mapped these in a sector-file which can be used in the future. It is hard to discuss each of the 65268 results for the equal amount of detectors in the model. Some have been discussed in section 5.2. The positive note is, that future research can built on this thesis by using this sector-file and looking into specific local design changes of the structural build-up of a 6U interplanetary CubeSat. Which is something that will support space travel in the future.

10. Future Work

To further investigate the radiation shielding of future CubeSat missions to interplanetary space, this section shall state the research topics that are not performed yet, but which may lead to significant results.

1. Looking at the energy spectrum

The energy spectrum (0.1 MeV to 1 GeV) of the proton flux in appendix B can be studied further. The outcome of the forward Monte Carlo method has provided the particle flux for each band of the spectrum arriving at each part of the satellite model. This means that one can use the data from the forward Monte Carlo simulation to further look into the materials required at specified locations to optimize the shielding of the CubeSat model.

2. Other CubeSat models

This thesis has solely focussed on 6U because of its high relevance towards current and planned missions of CubeSats to both the Moon and Mars. In the future, CubeSats may also be applicable for missions towards other destinations such as Venus, Jupiter etc. Besides the fact that they pose other radiation environments on the satellite, the model might change to 12U or even larger CubeSats when one want to orbit Jupiter with a CubeSat. The trend in CubeSat design has to be followed and potentially the radiation shielding of larger CubeSats can be investigated.

3. Alternating materials in the state-of-the-art 6U model

The data provided by this thesis can be used to further optimize the design of the 6U CubeSat by both looking at different materials as well as structural alternations. The dose- and sector files in the appendices D to F can support the researcher in identifying parts with a high dose deposition. Collaboration with companies like ISIS can prove to be helpful, as the current contribution of ISIS was limited to their cad-models and not their expertise.

11. Bibliography

Badavi et al. (2009), NASA, *Validity of the Aluminum Equivalent Approximation in Space Radiation Shielding,* Retrieved from: http://www.ntrs.nasa.gov/archive/nasa/casi.ntrs.nasa.gov/20090026532.pdf .

Badhwar & Cucinotta (1999), *A Comparison of Depth Dependence of Dose and Linear Energy Transfer Spectra in Aluminium and Polyethylene*, retrieved from: http://www.bioone.org/doi/pdf/10.1667/0033-7587%282000%29153%5B0001%3AACODDO%5D2.0.CO%3B20

Baker J.D. (2017), Presentation: Mars Cube One Overview, retrieved from: https://ssed.gsfc.nasa.gov/pcsi/docs/2017/presentations/014-Communication-A-MarCO-Overview-GSFC%20Symposium.pdf

Beningo J. (2010), *A Review of Watchdog Architectures and their Application to Cubesats,* retrieved from: https://www.beningo.com/wp-content/uploads/images/Papers/WatchdogArchitectureReview.pdf

Cubesatshop.com (2017), Catalogue of commercial CubeSat material, http://www.cubesatshop.com/

Eckart, P. (2006), *The lunar base handbook - An introduction to lunar base design, development and operations*, P142-152, Columbus, United States: McGraw-Hill Education

ESA/ESTEC (2017), Article about work of dr. U. Lafont: *3D Printing CubeSat Bodies for Cheaper, Faster Missions*, retrieved from: http://www.esa.int/Our_Activities/Space_Engineering_Technology/3D_printing_CubeSat_bodies_for_cheaper_faster_missions

Copeland S. (2012), *The Deep Space Radiation Environment*, Stanford University, retrieved from: http://large.stanford.edu/courses/2012/ph241/copeland2/

Daly et al. (1996), Space environment analysis: Experience and trends, in ESA Symposium on Environment Modelling for Space-based Applications, p.15-22.

Emslie (2004), *Energy Partition in two solar flare/CME events,* American Geophysical Union, doi: 10.1029/2004JA010571

Feynman et al. (1990), A new interplanetary fluence model. In: journal of spacecraft and rockets 27, p. 3-10.

Feynman and Gabriel (2000), On space weather consequences and predicitons. In: Journal of geophysical research 105, p. 43-64.

GEANT4 (2017), Information on GEANT4 software, retrieved from: http://geant4.esa.int/

George J.S. et al. (2009), *Elemental composition and energy spectra of galactic cosmic rays during solar cycle 23*, in the Astrophysics Journal 698:1666 page 4, Pasadena, United States

Github, User: Timo-Sanders, Folder: Dec2018, files: Appendix B to F, retrievable from: https://github.com/Timo-Sanders/Dec2018

Heynderickx et al. (2017), SEPEM reference data set (rds) v2.0, http://sepem.eu/help/SEPEM_RDS_v2-00.zip

ISIS (2017), Overview of structural CubeSat material readily available from the Innovative Solutions in Space (ISIS) webshop, http://www.isispace.nl/product-category/satellite-products/cubesat-structures

Jiggens et al. (2018), *Updated Model of the Solar Energetic Proton Environment in Space,* Journal of Space Weather and Space Climate, doi: 1801.05422

Kramer H.J., 2017, Information on QuakeSat, retrieved from: https://directory.eoportal.org/web/eoportal/satellite-missions/q/quakesat

Lai, S.T. (2011) , *Fundamentals of spacecraft charging*, Ch.14 Energetic particle penetration pages 126-136, Princeton University, United States: Princeton University Press

Loff, S. (2017), NASA information page on Explorer-1, retrieved from: https://www.nasa.gov/mission_pages/explorer/explorer-overview.html

Mark H. (2003), *Encyclopedia of Space Science and Technology volume II,* pages 583-598, New York, United States: Wiley

Mewaldt (2005), *Proton, helium and electron spectra during the large solar particle events of October-November 2003,* American Geophysical Unit, doi: 10.1029/2005JA011038

Myung-Hee K.Y. (1994), *Performance Study of Galactic Cosmic Ray Shield Materials,* NASA technical paper 3473, retrieved from: http://citeseerx.ist.psu.edu/viewdoc/download?doi=10.1.1.406.8737&rep=rep1&type=pdf

Nanosats.eu (2018), Information and figures of trends of CubeSat sizes and launches through time, retrieved from: https://www.nanosats.eu/index.html#figures

NASA (2002), n.n., *Understanding Space Radiation,* retrieved from: https://spaceflight.nasa.gov/spacenews/factsheets/pdfs/radiation.pdf

NASA (2017), Mars Cube One (MarCO) mission by NASA, retrieved from https://www.jpl.nasa.gov/cubesat/missions/marco.php

Neil et al. (2008), *Importance of predicting the dose temporal profile for large solar energetic particle events*, Space Weather Vol. 6, doi: 10.1029/2008SW000393

Norbury J.W. (2010), Pion production data needed for space radiation. In: 40th international conference on environmental systems, Retrieved from NASA Technical Reports Server (NTRS), 12–15 July 2010

QB50.com, 2017, Information on the collaboration of CubeSats called QB50, retrieved from: https://www.qb50.eu/

Rasmussen R.J. (1988), *Spacecraft Electronics Design for Radiation Toleranc,* Proceedings of the IEEE vol. 76 no. 11, p.1527-1537.

Rodriguez et al. (2017), Validation of the effect of cross-calibrated goes solar proton effective energies on derived integral fluxes by comparison with stereo observations. In: Space Weather 15, 2017: p.290-309.

Shirley J.H. (1997), *Encyclopedia of Planetary Sciences,* Dordrecht, Netherlands: Springer

Sinclair and Dyer (2013), *Radiation Effects on COTS Parts in SmallSats*, 27^{th} annual AIAA/ISU Conference on Small Satellites.

SPENVIS (2017), Information on SPENVIS software, retrieved from: https://www.SPENVIS.oma.be/help/models/packages.html

Staehle et al. (2014), *Interplanetary CubeSats: Opening the Solar System to a Broad Community at Lower Cost*, Journal of Small Satellites Vol.2 No. 1 pp. 161-186

Tiano et al. (n.d.), *Boron Nitride Nanotube: Synthesis and Applications*, retrieved from: https://ntrs.nasa.gov/archive/nasa/casi.ntrs.nasa.gov/20140004051.pdf

TRAD (2017), Information on FASTRAD software, retrieved from: http://www.Fastrad.net/

TU Delft (2017), website of the Delfi nanosatellite project of TU Delft, retrieved from: http://www.delfispace.nl/

Wertz J.R. (1999), *Space Mission Analysis and Design,* Space Technology Library, United States

Wilson J. (2008) *Issues in Space Radiation Protection: Galactic Cosmic Rays*, Health Physics volume 68, pages 50-58

Appendix A - Radiation Detector Placement

In Fastrad, detectors are necessary to measure the incoming radiation. This section discusses where the detectors are placed in this test and why. Again, the distinction shall be made between the models where the material varies and the models where payloads are added.

The material models presented in section 6.2 are all basically empty boxes with the type of material as the variable in this simulation. The high symmetrical layout of the box, has its consequences on the area to be investigated. As the material models are boxes, these are symmetrical around three axis. Hence, inspection of only one eighth of the total volume is required to get a full picture of the radiation doses at all locations in the model. This statement leads to the placement of detectors in only one octant of the model.

In order to get a reference value on all sides of the model, a detector was placed on all outsides of the positive XY, YZ and XZ planes of the thin box structures. Also, a reference detector was placed in the centre of the box, so in the origin in Figure A.1. The other three detectors on the positive XY YZ and XZ planes can be found when following the X, Y and Z axes from that origin in figure A.1 In total there are 28 detectors. These are the 27 detectors in a 3x3x3 mesh in one octant plus the detector on the outside of the model, which will measure the outside radiation level.

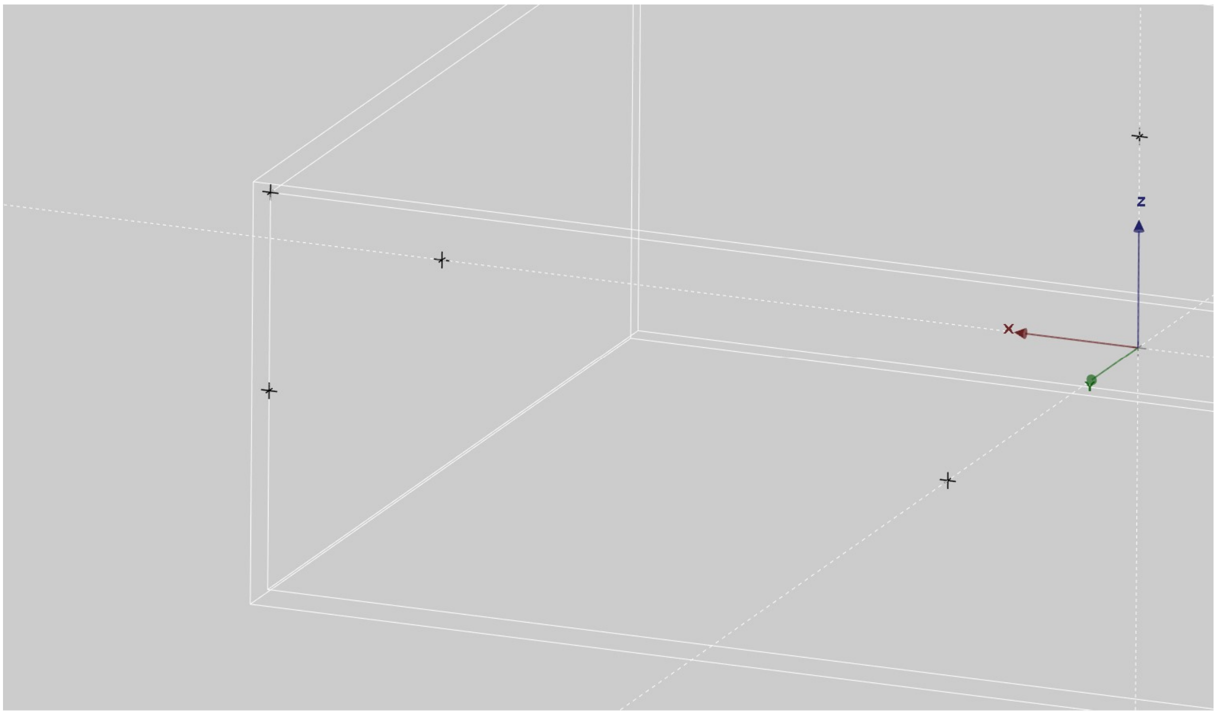

Figure A.1: Six of the 28 detectors in one octant of the model. The detectors shown are on the extreme locations within the octant (centre, maximum X, maximum Y, maximum Z, top corner).

To get a better view of the sandwich structure used in box structures 8 to 10 and the place of the detector on the inside of the corner of three planes, figure 7 is included. In this figure one can see the layered structure of box 9 (1mm Al, 0.1mm Cu, 0.8mm Polyethylene, 0.1mm Cu, 1mm Al). The origin in the picture is at the corner-detector location, which is on the inside of the corner of the model.

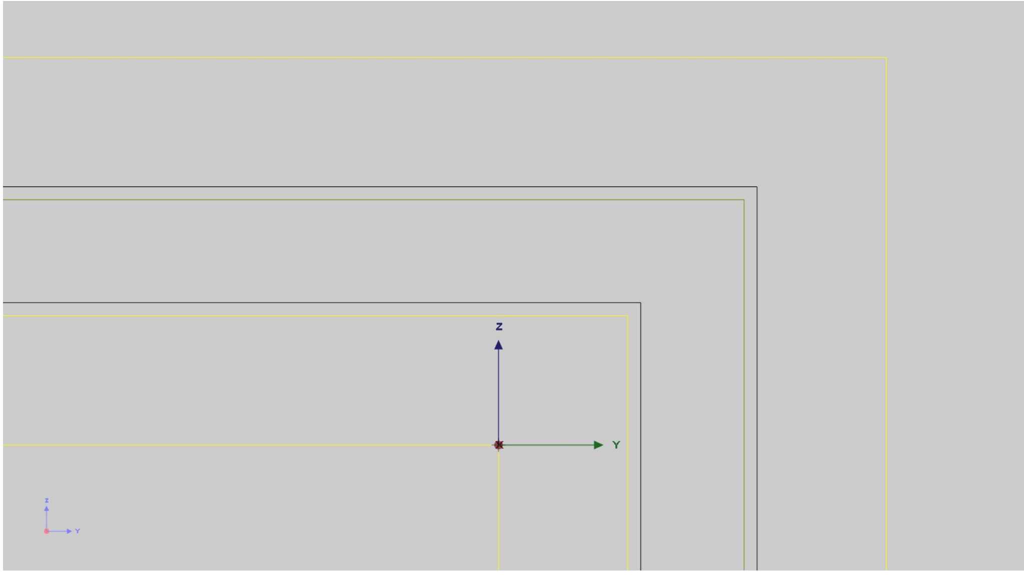

Figure A.2: Location of the corner-detector, designated with the axes focussed on the location of the detector, in the corner of the inside of the box. One can also clearly see the layered structure of this specific box 9 design, which has five layers: 1.0mm of Aluminium, 0.1mm of Copper, 0.8mm of Polyethylene, 0.1mm of Copper and 1.0 mm of Aluminium.

By creating this 3x3x3 detectors mesh for all material models, the local radiation levels in all ten material models can be easily compared. Also, the difference in radiation levels of the three side panels is investigated. Since the box is not a cube, slight variations are expected.

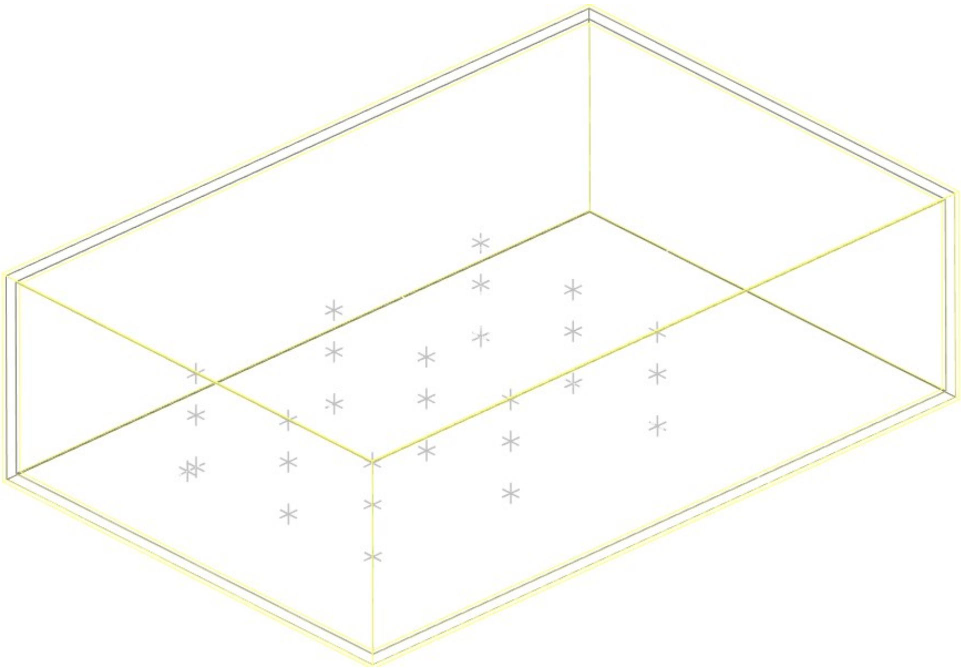

Figure A.3: The 3x3x3 mesh of detectors in one octant of the model. Also visible, the outside detector on the near-left outer panel of the model.

Appendix B – Proton Flux during a 1-in-100 years SPE

1st Column: Energy [MeV]

2nd Column: Integral proton flux [#/(m^2*s*sr)]

3rd Column: Differential proton flux [#/(m^2*s*sr*MeV)]

```
'*',     39,      1,     18,     14,      5,      5,     81,       1
'SPENVIS 4.6.10.3393          - 21-Nov-2018 20:30:36'
'PRJ_DEF', -1,'SOLARMAXIMUM'
'PRJ_HDR', -1,'Solar Maximum 2012-2015'
'MOD_ABB', -1,'FLA'
'MIS_PLA',  1,    -3,' '
'MIS_NTR',  1,     1,' '
'MIS_STA',  1,  22645.00000000,' '
'MIS_END',  1,  22649.00000000,' '
'MIS_DUR',  1, 4.000000E+00,'days'
'FLA_IEL',  1,  1,' '
'FLA_JEL',  1, 92,' '
'FLA_MOD', -1, 'SAPPHIRE 1 in n year event peak flux'
'FLA_OMN',  1, 0, ' '
'FLA_ABS', -1,'Energy'
'FLA_IGC',  1,  0,' '
'FLA_IGV',  1,  1,' '
'FLA_IST',  1,  0,' '
'PLT_HDR', -1,'SAPPHIRE 1 in n year event peak proton flux'
'SPECIES', -1,'proton'
'PS Annotation',  8,   1
'Mission start: 01/01/2012 00:00:00'
 0.05, 0.00, 0.00
'Mission end: 05/01/2012 00:00:00'
 0.95, 0.00, 1.00
'Nr. of segments:    1'
 0.05, 1.50, 0.00
'Duration: 4.00 days'
 0.95, 0.00, 1.00
'PS Annotation',  4,   0
'Solar particle model: SAPPHIRE 1 in 100 years event peak flux'
 0.05, 2.00, 0.00
'Magnetic shielding:    off'
 0.10, 1.50, 0.00
'Energy','MeV', 1,'Energy'
'IFlux','m!u-2!n sr!u-1!n s!u-1!n', 1,'Integral Flux'
'DFlux','m!u-2!n sr!u-1!n s!u-1!n MeV!u-1!n', 1,'Differential Flux'
'Attenuation',' ', 1,'Orbit Averaged Proton Attenuation Factor'
'Exposure','hrs', 1,'Proton Exposure Time'
  1.0000E-01,  3.8909E+10,  2.6779E+11, 1.0000, 8.0000E+00
  1.1000E-01,  3.6430E+10,  2.2958E+11, 1.0000, 8.0000E+00
  1.2000E-01,  3.4290E+10,  1.9948E+11, 1.0000, 8.0000E+00
  1.4000E-01,  3.0770E+10,  1.5550E+11, 1.0000, 8.0000E+00
  1.6000E-01,  2.7979E+10,  1.2533E+11, 1.0000, 8.0000E+00
  1.8000E-01,  2.5703E+10,  1.0345E+11, 1.0000, 8.0000E+00
  2.0000E-01,  2.3805E+10,  8.7074E+10, 1.0000, 8.0000E+00
  2.2000E-01,  2.2195E+10,  7.4502E+10, 1.0000, 8.0000E+00
  2.5000E-01,  2.0182E+10,  6.0443E+10, 1.0000, 8.0000E+00
  2.8000E-01,  1.8530E+10,  5.0207E+10, 1.0000, 8.0000E+00
  3.2000E-01,  1.6734E+10,  4.0211E+10, 1.0000, 8.0000E+00
  3.5000E-01,  1.5614E+10,  3.4645E+10, 1.0000, 8.0000E+00
  4.0000E-01,  1.4064E+10,  2.7748E+10, 1.0000, 8.0000E+00
  4.5000E-01,  1.2807E+10,  2.2813E+10, 1.0000, 8.0000E+00
  5.0000E-01,  1.1763E+10,  1.9100E+10, 1.0000, 8.0000E+00
  5.5000E-01,  1.0883E+10,  1.6247E+10, 1.0000, 8.0000E+00
  6.3000E-01,  9.7249E+09,  1.2904E+10, 1.0000, 8.0000E+00
  7.1000E-01,  8.7925E+09,  1.0535E+10, 1.0000, 8.0000E+00
  8.0000E-01,  7.9365E+09,  8.5914E+09, 1.0000, 8.0000E+00
```

```
  9.0000E-01,  7.1613E+09,  6.9984E+09, 1.0000, 8.0000E+00
  1.0000E+00,  6.5229E+09,  5.8255E+09, 1.0000, 8.0000E+00
  1.1000E+00,  5.9869E+09,  4.9347E+09, 1.0000, 8.0000E+00
  1.2000E+00,  5.5295E+09,  4.2410E+09, 1.0000, 8.0000E+00
  1.4000E+00,  4.7898E+09,  3.2281E+09, 1.0000, 8.0000E+00
  1.6000E+00,  4.2174E+09,  2.5389E+09, 1.0000, 8.0000E+00
  1.8000E+00,  3.7607E+09,  2.0543E+09, 1.0000, 8.0000E+00
  2.0000E+00,  3.3870E+09,  1.6997E+09, 1.0000, 8.0000E+00
  2.2000E+00,  3.0753E+09,  1.4300E+09, 1.0000, 8.0000E+00
  2.5000E+00,  2.6948E+09,  1.1255E+09, 1.0000, 8.0000E+00
  2.8000E+00,  2.3911E+09,  9.1033E+08, 1.0000, 8.0000E+00
  3.2000E+00,  2.0698E+09,  7.0894E+08, 1.0000, 8.0000E+00
  3.5000E+00,  1.8743E+09,  5.9943E+08, 1.0000, 8.0000E+00
  4.0000E+00,  1.6111E+09,  4.6216E+08, 1.0000, 8.0000E+00
  4.5000E+00,  1.4054E+09,  3.6652E+08, 1.0000, 8.0000E+00
  5.0000E+00,  1.2402E+09,  2.9787E+08, 1.0000, 8.0000E+00
  5.5000E+00,  1.1046E+09,  2.4692E+08, 1.0000, 8.0000E+00
  6.3000E+00,  9.3216E+08,  1.8808E+08, 1.0000, 8.0000E+00
  7.1000E+00,  7.9922E+08,  1.4680E+08, 1.0000, 8.0000E+00
  8.0000E+00,  6.8246E+08,  1.1462E+08, 1.0000, 8.0000E+00
  9.0000E+00,  5.8118E+08,  8.9461E+07, 1.0000, 8.0000E+00
  1.0000E+01,  5.0142E+08,  7.1095E+07, 1.0000, 8.0000E+00
  1.1000E+01,  4.3733E+08,  5.7751E+07, 1.0000, 8.0000E+00
  1.2000E+01,  3.8480E+08,  4.7768E+07, 1.0000, 8.0000E+00
  1.4000E+01,  3.0456E+08,  3.3653E+07, 1.0000, 8.0000E+00
  1.6000E+01,  2.4686E+08,  2.4714E+07, 1.0000, 8.0000E+00
  1.8000E+01,  2.0370E+08,  1.8821E+07, 1.0000, 8.0000E+00
  2.0000E+01,  1.7061E+08,  1.4531E+07, 1.0000, 8.0000E+00
  2.2000E+01,  1.4477E+08,  1.1481E+07, 1.0000, 8.0000E+00
  2.5000E+01,  1.1533E+08,  8.3702E+06, 1.0000, 8.0000E+00
  2.8000E+01,  9.3621E+07,  6.2486E+06, 1.0000, 8.0000E+00
  3.2000E+01,  7.2675E+07,  4.3768E+06, 1.0000, 8.0000E+00
  3.5000E+01,  6.1016E+07,  3.4462E+06, 1.0000, 8.0000E+00
  4.0000E+01,  4.6661E+07,  2.3845E+06, 1.0000, 8.0000E+00
  4.5000E+01,  3.6598E+07,  1.6934E+06, 1.0000, 8.0000E+00
  5.0000E+01,  2.9325E+07,  1.2464E+06, 1.0000, 8.0000E+00
  5.5000E+01,  2.3895E+07,  9.4439E+05, 1.0000, 8.0000E+00
  6.3000E+01,  1.7773E+07,  6.1656E+05, 1.0000, 8.0000E+00
  7.1000E+01,  1.3677E+07,  4.2336E+05, 1.0000, 8.0000E+00
  8.0000E+01,  1.0513E+07,  2.9066E+05, 1.0000, 8.0000E+00
  9.0000E+01,  8.0967E+06,  1.9992E+05, 1.0000, 8.0000E+00
  1.0000E+02,  6.4031E+06,  1.4295E+05, 1.0000, 8.0000E+00
  1.1000E+02,  5.1733E+06,  1.0547E+05, 1.0000, 8.0000E+00
  1.2000E+02,  4.2544E+06,  7.9867E+04, 1.0000, 8.0000E+00
  1.4000E+02,  3.0017E+06,  4.8726E+04, 1.0000, 8.0000E+00
  1.6000E+02,  2.2132E+06,  3.1705E+04, 1.0000, 8.0000E+00
  1.8000E+02,  1.6877E+06,  2.1669E+04, 1.0000, 8.0000E+00
  2.0000E+02,  1.3217E+06,  1.5396E+04, 1.0000, 8.0000E+00
  2.2000E+02,  1.0576E+06,  1.1288E+04, 1.0000, 8.0000E+00
  2.5000E+02,  7.8206E+05,  7.4292E+03, 1.0000, 8.0000E+00
  2.8000E+02,  5.9665E+05,  5.1162E+03, 1.0000, 8.0000E+00
  3.2000E+02,  4.3204E+05,  3.2871E+03, 1.0000, 8.0000E+00
  3.5000E+02,  3.4698E+05,  2.4379E+03, 1.0000, 8.0000E+00
  4.0000E+02,  2.4921E+05,  1.5566E+03, 1.0000, 8.0000E+00
  4.5000E+02,  1.8527E+05,  1.0442E+03, 1.0000, 8.0000E+00
  5.0000E+02,  1.4156E+05,  7.2825E+02, 1.0000, 8.0000E+00
  5.5000E+02,  1.1060E+05,  5.2422E+02, 1.0000, 8.0000E+00
  6.3000E+02,  7.7358E+04,  3.2652E+02, 1.0000, 8.0000E+00
  7.1000E+02,  5.6128E+04,  2.1411E+02, 1.0000, 8.0000E+00
  8.0000E+02,  4.0501E+04,  1.3974E+02, 1.0000, 8.0000E+00
  9.0000E+02,  2.9168E+04,  9.1196E+01, 1.0000, 8.0000E+00
  1.0000E+03,  2.1628E+04,  6.1939E+01, 1.0000, 8.0000E+00
'End of Block'
'End of File'
```

Appendix C – Dose Depth Curve (SPENVIS output)

1st Column: Equivalent mm-Aluminium [mm]
2nd Column: Radiation Dose [rad]

```
#'*',     25,      1,     11,     10,      2,      6,     25,      0
#'SPENVIS 4.6.10.3386           -  3-Dec-2018 16:10:12'
#'PRJ_DEF', -1,'SOLARMAXIMUM'
#'PRJ_HDR', -1,'Solar Maximum 2012-2015'
#'MOD_ABB', -1,'SH2'
#'MIS_PLA',  1,    -3,' '
#'MIS_NTR',  1,     1,' '
#'MIS_STA',  1,  22645.00000000,' '
#'MIS_END',  1,  22649.00000000,' '
#'MIS_DUR',  1, 4.000000E+00,'days'
#'PLT_TYP', -1,'SUMMARY'
#'PLT_HDR', -1,'4pi Dose at Centre of Al Spheres'
#'PLT_LEG', -5,'Total','Electrons','Bremsstrahlung','Trapped
#Protons','Solar Protons'
#'PS Annotation',  8,  1
#'Mission start: 01/01/2012 00:00:00'
# 0.05, 0.00, 0.00
#'Mission end: 05/01/2012 00:00:00'
# 0.95, 0.00, 1.00
#'Nr. of segments:    1'
# 0.05, 1.50, 0.00
#'Duration: 4.00 days'
# 0.95, 0.00, 1.00
#'PS Annotation',  0,  0
#'Thick','mm',#'Dose','rad',
5.0000E-02  1.0812E+05
1.0000E-01  6.5455E+04
2.0000E-01  3.8273E+04
3.0000E-01  2.7232E+04
4.0000E-01  2.0914E+04
5.0000E-01  1.6977E+04
6.0000E-01 1.4240E+04
8.0000E-01 1.0630E+04
1.0000E+00 8.3956E+03
1.5000E+00 5.3853E+03
2.0000E+00 3.7816E+03
2.5000E+00 2.8634E+03
3.0000E+00 2.2630E+03
4.0000E+00 1.5236E+03
5.0000E+00 1.0988E+03
6.0000E+00 8.5089E+02
7.0000E+00 6.6823E+02
8.0000E+00 5.3997E+02
9.0000E+00 4.5029E+02
1.0000E+01 3.7630E+02
1.2000E+01 2.7958E+02
1.4000E+01 2.1185E+02
1.6000E+01 1.6725E+02
1.8000E+01 1.3703E+02
2.0000E+01 1.1271E+02

'End of File'
```

Appendix D – Dose-files and Sector files of Ray-tracing analysis on simplified models

Can be retrieved from Github: Timo-Sanders, Dec2018, Appendix D

Appendix E – Dose-file and Sector-file of Ray-tracing analysis on 6U realistic model

Can be retrieved from Github: Timo-Sanders, Dec2018, Appendix E

Appendix F – Forward Monte Carlo simulation results of 6U model

Can be retrieved from Github: Timo-Sanders, Dec2018, Appendix F

Appendix G – Workflow-diagram

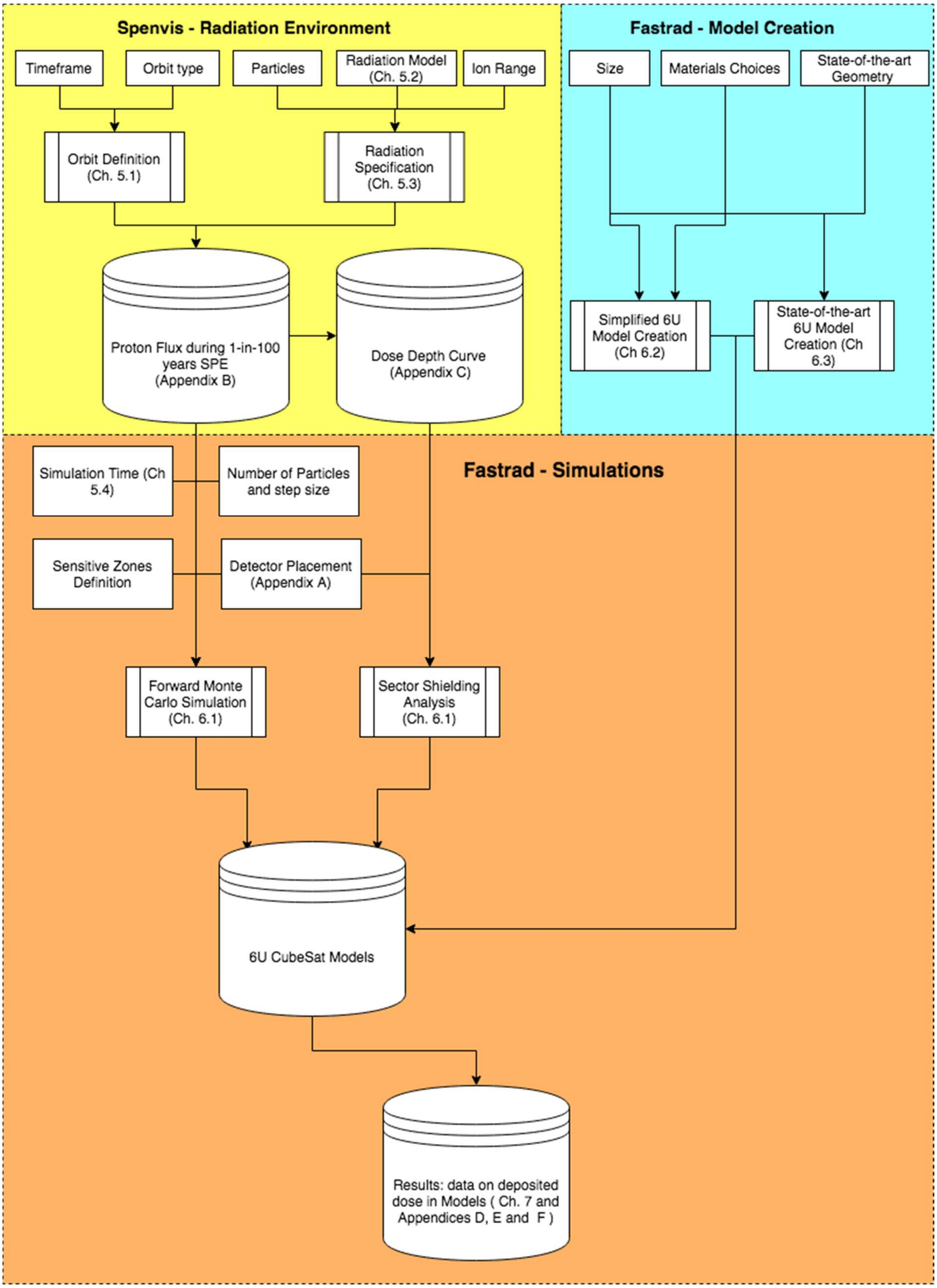

Figure G.1: Work-flow diagram of thesis. Inputs from SPENVIS (top left) and Fastrad models (top right) are combined to simulate in Fastrad (bottom).